SHORT-EXTERNAL-CAVITY NEAR-INFRARED DIODE LASERS FOR USE IN MOLECULAR SPECTROSCOPY

By

BRIAN FRANCIS VENTRUDO, B.Sc., M.Sc.

A Thesis

Submitted to the School of Graduate Studies

in Partial Fulfilment of the Requirements

for the Degree

Doctor of Philosophy

McMaster University

SXC NEAR-IR DIODE LASERS FOR USE IN MOLECULAR SPECTROSCOPY

DOCTOR OF PHILOSOPHY McMASTER UNIVERSITY

(Engineering Physics) Hamilton, Ontario

TITLE: Short-External-Cavity Near-Infrared Diode Lasers For Use In Molecular Spectroscopy

AUTHOR: Brian F. Ventrudo, B.Sc. (Lakehead University)

M.Sc. (University of Western Ontario)

SUPERVISORS: Professor D.T. Cassidy and Professor J. Reid

NUMBER OF PAGES: xvii,166

ABSTRACT

InGaAsP and AlGaAs near-IR laser diodes with a short external cavity (SXC) were characterized and used as single-mode radiation sources for molecular spectroscopy. A module for extended temperature-tuning of the lasers was tested to evaluate their single-mode frequency tuning range. AlGaAs SXC lasers operating at 0.76 μm tuned up to 400 cm^{-1} in a single mode, a few wavenumbers at a time, with no gaps in frequency coverage. InGaAsP SXC lasers operating at 1.3-1.55 μm tuned up to 200 cm^{-1} in a similar fashion. A technique was developed to control the behaviour of the longitudinal modes and enhance laser operation. The technique employed interference fringes in the laser output intensity distribution to produce a discriminating signal used in an electrical feedback loop to maintain the external cavity at the optimum length for single-mode operation. Control theory was used to optimize the operation of this feedback loop. The SXC lasers were used in a high-sensitivity absorption spectrometer. The noise sources of the spectrometer were assessed, and the sensitivity obtained with SXC lasers was compared with that obtained with distributed feedback lasers. Both lasers yielded sensitivities of $\approx 3 \times 10^{-6}$ in units of equivalent absorbance in an equivalent noise bandwidth of 1.25 Hz. The sensitivity was limited by etalon fringes produced by optical components in the detection path. The SXC laser spectrometer was employed to monitor the relative abundance of H_2O/HDO and $^{12}CO_2/^{13}CO_2$. Changes in the relative abundance

as small as 1% could be observed. The crystal-field and impurity splitting of the $W_{1\leftarrow 0}(0)$ transition of solid hydrogen were observed with the spectrometer. Finally, frequency measurements were made of the $3\nu_2 \leftarrow 0$ ro-vibrational band of the H_3^+ molecular ion.

ACKNOWLEDGEMENTS

I would like to express my gratitude to my supervisor, Professor Daniel T. Cassidy, for his guidance, encouragement, and generosity during the course of my studies. I also thank my co-supervisor, Professor John Reid, for many illuminating discussions and for teaching me how to think about physical problems more intuitively.

Dr. Doug Bruce helped me enormously during my early days with the trace-gas detection system, and with the wire bonding of many lasers. I also profited from many discussions about lasers, etc., with my colleagues in the sub-basement of the Burke Science Building, especially Joe Hayward and Shane Woodside.

I express my thanks to everyone at the Oka Ion Factory, University of Chicago, for three enjoyable summers of research. I particularly thank Steven Lee, Zhaoyu Guo, Sangwoo Joo, Matthias Rosslein, and Charles Gabrys for a pleasurable and fruitful collaboration on the H_3^+ project; I also enjoyed both working hard and playing hard with Karen Kerr and Teri Byers. I especially thank Professor Takeshi Oka for sharing with me his time, his wisdom, and his exceptional enthusiasm and ability for scientific research.

Most of all I thank my wife Lorie, to whom this work is dedicated, for her patience and support during the course of my studies.

TABLE OF CONTENTS

LIST OF FIGURES

LIST OF TABLES

CHAPTER 1 - INTRODUCTION

1.1 Lasers and Spectroscopy

The study of atomic and molecular spectroscopy has undergone a revolution since the introduction in 1960 of the laser. This device produces intense and coherent radiation that cannot be provided with "classical" light sources. The properties of laser radiation allow the detection and very accurate measurement of weak atomic and molecular transition frequencies. In addition, the high intensity of the electric field in a laser beam can induce previously unobserved non-linear effects in both gases and solids; these phenomena have formed the basis for a new area of research in spectroscopy. The power and elegance of the techniques of laser spectroscopy and the importance of the knowledge gained are indisputable. Indeed, the field of spectroscopy today is almost unrecognizable compared to the time before the laser's introduction.

The scientific and technological importance of the laser has incited enormous efforts in the development of a wide variety of lasers using many different pumping schemes and active media that emit radiation over a broad range of frequencies. Laser

radiation can now be produced over almost the entire range of the electromagnetic spectrum from the far infrared to the vacuum ultraviolet. Some lasers, such as the CO_2 laser, emit at discrete frequencies that are restricted by the spectral properties of their active media. The use of such lasers in spectroscopy often depends on a fortunate coincidence between the frequency of laser emission and the resonant frequency of the system of interest. Other lasers such as dye, colour-centre or titanium-sapphire lasers are widely tunable over many hundreds of wavenumbers which makes them more versatile in spectroscopic investigations where the features of interest are spread over a wide range of frequency.

Semiconductor diode lasers are another variety of tunable laser that have found wide application in molecular spectroscopy. Devices based on II-VI lead-salt semiconductor compounds have been used very extensively since the early 1970's to make absorption spectroscopic measurements in the mid-infrared region (3-30 μm). They are a common tool in the modern spectroscopy laboratory and in applied spectroscopic studies of air pollution and combustion analysis [1].

The first semiconductor diode lasers were not made from a Pb-salt compound but from GaAs, a III-IV semiconductor [2,3,4,5]. Such lasers were at the time little more than laboratory curiosities, but were used in a small number of early spectroscopic investigations [6,7,8]. Ternary and quaternary semiconductors such as AlGaAs and InGaAsP have since been developed that can lase at room temperature. AlGaAs lasers can be constructed to emit radiation over a range of $\approx$20-30 nm in the 0.7-0.9 μm

region. InGaAsP lasers emit radiation over a similar range in the 1.1-1.7 μm region. The nominal frequency of each device depends on the fractional composition of the semiconductor. The potential application of AlGaAs and InGaAsP lasers for fibre-optic communication systems has since 1975 fuelled a tremendous amount of activity in research and development aimed to improve the operation and reliability of these lasers. Today such devices are far more technologically advanced and economical than Pb-salt devices, and they are much easier to operate because they lase at room temperature and require far less injection current than Pb-salt lasers. The global proliferation of optical communication systems is a testament to the success of fibre-optic and III-V laser diode technology.

1.2 Spectroscopy with Near-IR Diode Lasers

The availability and low cost of III-V laser diodes emitting in the near-IR have also sparked the interest of atomic and molecular spectroscopists. AlGaAs lasers provide excellent alternatives to dye lasers, and many spectroscopic investigations of atoms and molecules have been pursued with these lasers in recent years. InGaAsP lasers are important to spectroscopists because they are at present the most economical commercial source of laser radiation in the 1.1-1.7 μm range. Until the advent of these devices, this region has been relatively unexplored with the intensity and resolution that these lasers

can provide. Recently, however, there have been many applications of InGaAsP lasers to both pure and applied research in molecular spectroscopy.

AlGaAs and InGaAsP diode lasers operate on very similar principles and have comparable output powers and spectral characteristics. However, because they operate at slightly different frequencies, each type of laser has generally been used to investigate distinct types of spectroscopic phenomena.

AlGaAs diode lasers cover the spectral region from 0.7-0.9 μm (14300 - 11100 cm^{-1}), which contains mostly atomic transitions of alkali metals and noble gases, a few molecular electronic transitions, and a few very weak molecular vibrational overtone transitions. The majority of applications of these lasers has been in investigations of atomic spectroscopy. By far the most actively pursued area of study with AlGaAs lasers is high-resolution spectroscopy and optical pumping of the hyperfine transitions of alkali metals. Of particular importance are the transitions in Rb and Cs that are used for frequency standards. AlGaAs diode lasers have been used for some time to pump the atoms into the lower state of the microwave "clock" transition and are then used to detect the atoms that have undergone the microwave transition. These lasers are also used in the "optical cooling" and trapping of Rb and Cs atoms. Reviews of the application of AlGaAs diode lasers in atomic physics are given by Camparo [9] and by Wieman and Hollberg [10].

InGaAsP diode lasers operate in the 1.1-1.7 μm (9100 - 5900 cm^{-1}) region. At these frequencies, there are few strong atomic transitions, but there exist many molecular

vibrational overtone transitions and a small number of molecular electronic transitions. Overtone transitions are by their nature much weaker than the fundamental vibrational transitions that are found at longer wavelengths. Most InGaAsP diode lasers do not yet have both the resolution and the power to saturate these overtone transitions, and most fundamental research so far has been restricted to the determination of the frequencies of overtone transitions rather than non-linear spectroscopy. Several Japanese groups, most notably H. Sasada and co-workers, have made fundamental measurements and assignments of near-IR overtone and combination bands of HCN [11,12], HDO and D_2O [13], C_2H_2 [14], and HN_2^+ [15]. Vibrational transitions of NH_3 have been used to stabilize the frequency of InGaAsP lasers [16,17]. Electronic bands of C_3 [18], C_2H [19] and Rydberg transitions of N_2 [20] have also been observed. The latter work also demonstrated the use of near-IR lasers for sub-Doppler saturation spectroscopy, made possible by the large dipole transition moment of the Rydberg states. Many more near-IR electronic and overtone transitions remain to be observed with InGaAsP lasers.

InGaAsP and AlGaAs lasers have also become popular for the monitoring of trace gases and atmospheric pollutants produced by natural or industrial processes. These devices are attractive for such applications because of their reliability, low-cost and ease of operation. The disadvantage of these lasers is that the molecular transitions are much weaker than at higher frequencies where, for example, Pb-salt lasers could be used. This trade-off is acceptable in some instances, however, and many investigations have been

performed to demonstrate the use of both InGaAsP and AlGaAs lasers in trace-gas detection [21,22,23,24,25,26,27,28]. The sensitivity that can be attained with these lasers permits real-time monitoring of concentrations of the ppm level, and such systems are now being developed for industrial and environmental use.

1.3 Single-Mode Near-IR Semiconductor Diode Lasers

The spectral purity of the emission of near-IR diode lasers is critical for applications in both spectroscopy and optical communications. An explanation of the spectral properties of semiconductor lasers is a formidable task; only a brief review of such properties that are important for spectroscopy is given here. For more complete treatments of the spectral properties of semiconductor lasers, see [29,30,31,32,33,34] and references therein.

Near-IR lasers are usually constructed so that laser emission occurs in the fundamental spatial mode; this is critical for coupling into optical fibres. However, lasing will typically occur on several longitudinal cavity modes, which are spaced in frequency by c/2nL, where c is the velocity of light and n and L are the group index and length of the laser cavity. The light from such a multi-mode laser is still quite monochromatic compared to classical light sources, but is not sufficient for high-speed communications and many spectroscopic applications. Optical fibres are dispersive, and

if a laser pulse is sent through a fibre, the dispersion of light of different frequencies will result in a broadening of the pulse and a limit on the rate at which such pulses can be sent through the fibre. In spectroscopy, highly monochromatic light is desired to act as a frequency-selective probe of atomic or molecular energy structure. Several laser modes oscillating at once may simultaneously probe several energy levels and confuse or obscure the signal that is ultimately detected.

A second problem for spectroscopic applications of diode lasers is related to the tuning of the laser frequency, which is most easily accomplished by altering the temperature of the laser. Frequency tuning results from the temperature dependence of the peak gain of the laser and the temperature dependence of the optical length of the laser cavity. The unfortunate situation is that, for most semiconductor lasers, these dependences are different which results in a discontinuous tuning of the laser frequency. At a particular temperature, for example, most of the laser emission may be in one longitudinal mode. When the temperature is increased, the frequency of the mode will decrease as a result of the change in optical length of the cavity. However, eventually, the peak gain of the laser will shift to the next longitudinal mode of lower frequency before the first mode has been completely tuned over a longitudinal mode spacing. As a result, a gap in the frequency coverage of the laser is observed; this is a serious problem for a laser used as a tunable source for molecular spectroscopy.

A third property of diode laser emission that is crucial for both spectroscopy and optical communications is the linewidth of each longitudinal mode. Even if a laser

operates in a single mode, there is a finite purity of spectral emission. Because of the relatively short cavities of diode lasers (only a few hundred microns, typically), the Schawlow-Townes linewidth is of the order of a few MHz. Further broadening is caused by the large amount of spontaneous emission that couples into a laser mode and by the coupling between intensity and frequency fluctuations that occur in semiconductor lasers, which increase the Schawlow-Townes limit by a factor of $(1+\alpha^2)$, where α is the ratio between the change in real and imaginary parts of the refractive index in the laser cavity [35]. The value of α is about -5 to -6 for bulk semiconductor [32]. For most solitary index-guided lasers, the linewidth is then typically 10-50 MHz for an output of a few mW [31], which is often too large for some applications. Again because of dispersion in optical fibres, this linewidth imposes a limitation on the rate at which information can be transmitted through a fibre. In addition, some experiments in saturation spectroscopy or high-precision measurement require very narrow linewidths of < 100 kHz.

There are several schemes for resolving the above difficulties. Most techniques to force operation in a single longitudinal mode or to narrow the laser linewidth employ some type of optical feedback into the laser cavity. Diode lasers are extremely susceptible to optical feedback [36]. This is often a negative aspect of diode laser operation because small amount of light reflected back into the laser cavity from the surfaces of fibres, lenses, and other optical elements can adversely affect the operating characteristics of a laser diode. It is possible, however, to utilize optical feedback from an external reflector in a positive way to control the spectral properties of a diode laser.

Mirrors, gratings, fibres and etalons have all been used as external reflectors. The laser may or may not have an anti-reflection coating on one facet to enhance optical feedback. All techniques have advantages and disadvantages: usually, tunability and ease of operation must be balanced against the requirement of spectral purity. Reviews of techniques for achieving single-mode operation of near-IR diode lasers are found in [10] and [37] and references therein.

1.4 Goal of the Thesis

The purpose of the research reported in this thesis was to characterize a particular configuration of external cavity diode laser, a short-external-cavity laser, for use in pure and applied research in molecular spectroscopy. Short-external-cavity (SXC) lasers retain the tunability of all diode lasers, but have the advantage of operating in a single longitudinal mode; they can be also be controlled to eliminate gaps in the tuning frequency that are exhibited by multimode diode lasers. The tuning range of both AlGaAs and InGaAsP SXC lasers was determined. A technique was developed to control the longitudinal modes of the laser to prevent mode hops caused by frequency tuning or thermal or mechanical perturbations to the laser or external cavity. Once the behaviour of both the lasers and mode control techniques was understood, the lasers were employed to make very sensitive spectroscopic measurements of molecular absorption

transitions. The sensitivity of the lasers was demonstrated by the detection of trace gases and determining the accuracy with which the relative concentration of isotopic constituents of these gases can be monitored. The lasers were used in fundamental spectroscopic investigations of the $W_{1-0}(0)$ transition of solid parahydrogen and second overtone band of the H_3^+ molecular ion. Finally, the limitations of SXC lasers as sources for molecular spectroscopy were assessed.

1.5 Outline of the Thesis

The remainder of this thesis details the implementation of SXC diode lasers and their application in molecular spectroscopic measurements. Chapter 2 describes the basic layout of an SXC laser and outlines the theory used to explain the steady-state spectral output of these devices. A description is made of the design of the SXC lasers that are used in this thesis, and a vacuum module is used to extend the tuning of these lasers by allowing large variation of the laser temperature. Chapter 3 relates the development of techniques to control the longitudinal mode behaviour of SXC lasers. A method developed by Cassidy and Bonnell [23] that uses the voltage behaviour of these lasers is compared to a new technique that employs interference fringes in the far-field intensity distribution of SXC lasers. The electrical feedback system for mode control is analyzed using elementary control theory, and strategies are discussed for the

optimization of the control system. Chapter 4 outlines the suitability of SXC laser diodes as radiation sources in a high-sensitivity absorption spectrometer. The techniques used to achieve sensitive detection are explained, and the factors that limit the sensitivity of the spectrometer are determined. The performance of the spectrometer with SXC laser diodes is then compared to that using distributed feedback laser diodes. Chapter 5 demonstrates the application the SXC laser absorption spectrometer using harmonic detection techniques. The accuracy of measuring the relative abundance of $^{13}CO_2/^{12}CO_2$ and HDO/H_2O is determined. An application to the detection of the $W_{1\leftarrow0}(0)$ dipole-induced multipole absorption transition in solid parahydrogen is also discussed, and the crystal-field and impurity splittings of the transition are measured. Chapter 6 describes the detection and measurement of the $3\nu_2\leftarrow0$ overtone band of the H_3^+ molecular ion, which is of fundamental importance in chemical physics and astrophysics. The techniques to produce and detect the ion are described, and methods to enhance the sensitivity are examined. Finally, Chapter 7 summarizes the results of the thesis and suggests improvements to the SXC lasers and further topics of research.

CHAPTER 2 -

OPERATION AND CONSTRUCTION OF SHORT-EXTERNAL-CAVITY SEMICONDUCTOR DIODE LASERS

2.1 Introduction

This chapter describes the theory, construction and operating characteristics of near-infrared short-external-cavity diode lasers that can be used as radiation sources for spectroscopy. The qualitative operation of an external cavity lasers is explained by considering the effect of the external cavity on the net gain of the solitary laser. The basic design, implementation, and the method of alignment of an SXC laser is presented. The construction details of a module for extended temperature-operation of the laser is given, and the frequency tuning ranges of SXC InGaAsP and AlGaAs lasers and InGaAsP distributed feedback lasers [38] using the module are reported.

2.2 *Fundamentals of Diode Laser Operation*

The steady-state spectral output of solitary semiconductor diode lasers are explained qualitatively in this section. Detailed analyses of diode laser operation can be found elsewhere [29,30,31].

Diode lasers are single crystals consisting of layers of epitaxially-grown semiconductor that form a p-n junction (Fig. 2.1). Lasing occurs in the active region, which is located at the junction in a narrow layer between highly doped p and n-type semiconductors. The active region is usually undoped and has a band gap E_{act} that is smaller than that of the surrounding semiconductor layers. When the diode is forward biased, charge carriers (electrons and holes) are injected into the active region and are confined there because of the lower band gap. The carriers combine in both radiative and non-radiative processes. Radiative recombination occurs spontaneously or by stimulated emission of a photon, and the light in the active region is optically confined and guided by the surrounding semiconductor layers because they have a lower refractive index than the active region. Most modern InGaAsP and AlGaAs diode lasers are index guided: optical confinement and guiding are provided on all sides of the active region by providing a refractive index step (Fig. 2.1).

When the carrier injection rate is sufficient to separate the quasi-Fermi levels (F_c for the conduction band and F_v for the valence band) of the active region by an energy larger than the band gap, then photons with energy

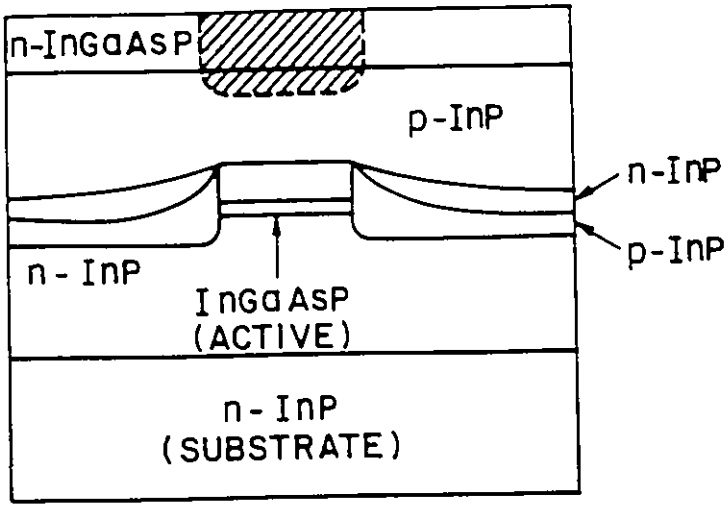

Figure 2.1

The architecture of a planar-buried heterostructure (index-guided) InGaAsP semiconductor diode laser (from reference 30).

$$E_{gap} < h\nu < F_c - F_v \tag{2.1}$$

will experience net gain. This is the condition for population inversion in a semiconductor. Light with frequency range defined in (2.1) entering the active region will be amplified. The total absorption coefficient is

$$\alpha = -g_{net} + \alpha_{int} \tag{2.2}$$

where g_{net} is the net gain per unit length and α_{int} is the loss of photons per unit length in the active region. A negative value of α indicates gain, rather than absorption.

The active region is located between the two end facets of the semiconductor crystal. These facets are partially reflecting because of the index step between the semiconductor and the outside environment. At an InGaAsP/air interface, for example, the reflectance is ≈ 0.32. The facets provide the necessary feedback of the photons in the active region to sustain laser operation. The loss from the facets also governs the threshold condition for laser operation and the Fabry-Perot cavity formed by the facets strongly influences the spectrum of laser emission. Consider Fig. 2.2, which illustrates the active region of a laser with length L, facet reflectances R_1 and R_2, and a complex propagation constant β given by

$$\beta = \frac{2\pi\nu}{c} n + i\alpha \tag{2.3}$$

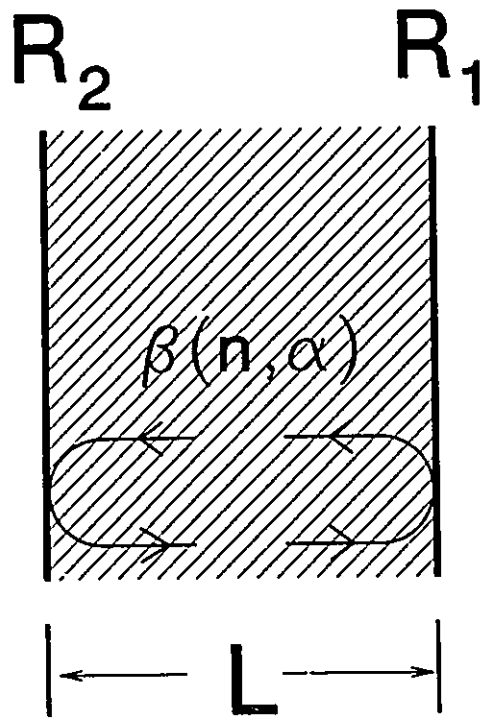

Figure 2.2

A schematic of the active region of a diode laser with propagation constant β in the active region with a circulating electric field.

where n is the refractive index of the active region, ν is the frequency of light in the cavity, and α is the absorption coefficient of (2.2). The condition for steady-state laser operation is that there is no change in the amplitude of the electric field in the laser cavity after one round trip through the cavity. This leads to the approximate condition

$$\sqrt{R_1 R_2}\,\exp(2i\beta L) \approx 1 \tag{2.4}$$

Equating the real parts of this relation gives

$$\sqrt{R_1 R_2}\,\exp(-\alpha L) = 1 \tag{2.5}$$

Equating the α in (2.5) with that of (2.2) gives the threshold condition

$$g_{net} = \alpha_m + \alpha_{int} \tag{2.6}$$

where

$$\alpha_m = \frac{1}{2L}\ln(1/R_1 R_2) \tag{2.7}$$

describes the cavity loss caused by light escaping through the facets averaged over the length of the device.[1] For lasing to occur, carrier injection must be sufficient to produce a net gain that (asymptotically) equals the total loss. Once this threshold gain is reached, lasing begins and the gain is "clamped" at the threshold value. Further pumping does

---

[1] Equation (2.6) is not quite accurate: the gain never quite equals the loss because a small number of the photons in the cavity are spontaneously emitted. This has the effect of reducing the gain necessary for lasing to commence.

not appreciably increase the gain, but is manifested in a larger number of photons in the cavity.

Equating the imaginary parts of (2.4) gives the relation

$$\sin(\frac{4\pi\nu nL}{c})=0 \tag{2.8}$$

There are multiple solutions for the frequency ν:

$$\nu_m = \frac{mc}{2nL} \tag{2.9}$$

where m is a positive integer. These are the central frequencies of the longitudinal modes of the laser cavity. They can also be obtained intuitively by considering the resonance condition of the cavity, in which a half-integral number of wavelengths must fit inside the length of the cavity. The separation of the laser modes, or free spectral range, is given by

$$\Delta\nu = \frac{c}{2n_s L} \tag{2.10}$$

where n_s is the group index of the active region. A typical InGaAsP laser has $n_s \approx 4.2$ and $L \approx 250\ \mu m$, which gives a mode spacing of $\approx 5\ cm^{-1}$ (1 nm).

Lasing does not occur on all the cavity resonance frequencies because the gain is also frequency dependent. The gain has a peak value at ν_0 and decreases gradually on either side of that frequency. The gain curve for semiconductor diode lasers is very

broad, typically ten's of nm, so several longitudinal modes will lase simultaneously. This is a disadvantage for lasers that are used in high-speed communications systems and spectroscopy. The loss in the diode laser is only weakly dependent on frequency, and can be approximated as being constant over the frequency range covered by several longitudinal modes. An illustration of the net gain, loss and cavity modes is found in Fig. 2.3(a); a measured spectrum from a 250 μm long InGaAsP index-guided laser operating above threshold is found in Fig. 2.3(b).

2.3 *Operation of Short-External-Cavity Diode Lasers*

Placing an external reflector behind one facet of a solitary laser forms a second cavity of length L_{ext} (Fig. 2.4). The ratio of the laser length to external cavity length is N :

$$N = \frac{nL}{L_{ext}} \tag{2.11}$$

If $N > 1$, then the external cavity is called a short-external cavity, since the length of the external cavity is less than the optical length of the laser. The purpose of the external mirror is to reflect a small amount of light back into the active region of the diode laser,

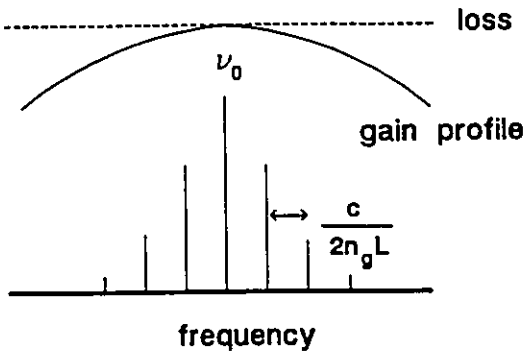

Figure 2.3(a)

An illustration of the gain, loss and laser cavity modes as a function of frequency in a solitary diode laser.

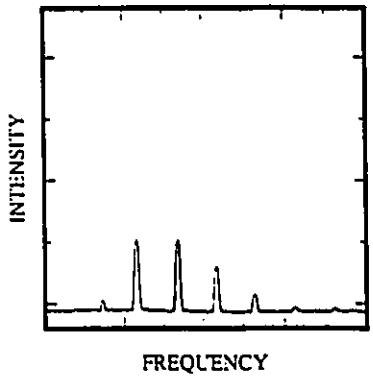

Figure 2.3(b)

The measured spectrum of a solitary index-guided InGaAsP diode laser operating at 1.5x threshold.

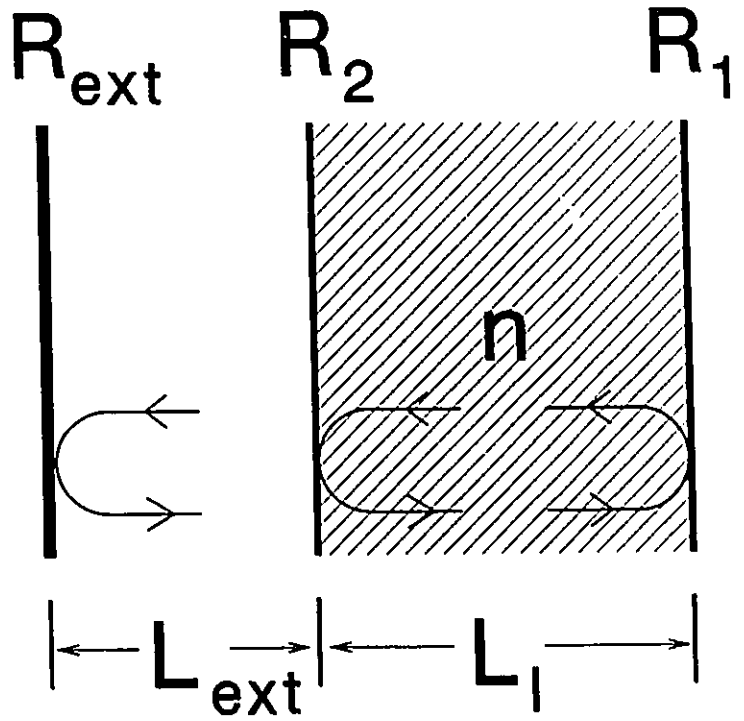

Figure 2.4

A schematic diagram of a short-external-cavity laser, showing the circulating electric field.

and this light influences the spectrum of laser emission in a way that depends sensitively on the amount of feedback and the length of the external cavity. When the external cavity is introduced, the laser behaves as a coupled-cavity laser [39], which in general is difficult to analyze. However, if the external mirror reflects only a small portion of the light back into the laser active region, the description of the effect on the laser is considerably simplified. For the geometry shown in Fig. 2.4, only $\approx 10^{-3}$ to 10^{-4} of the light emitted from the rear facet is reflected back into the active region for $L_{ext} \sim$ 100-200 μm, even if a highly reflective external mirror is used. The fraction of light reflected back into the laser cavity is labelled R_{ext}. For such small R_{ext}, the electric field entering the external cavity laser can be considered to make only one round trip of the external cavity. By tracing the amplitude and phase of the electric field through one round trip, an expression can be obtained for an effective reflectivity of the rear laser facet R_{eff}, which is given by

$$R_{eff}(\nu, L_{ext}) = R_2 + (1-R_2)^2 R_{ext} + 2(1-R_2)\sqrt{R_2 R_{ext}} \cos\frac{4\pi\nu L_{ext}}{c} \qquad (2.12)$$

The consequence of introducing the weakly-reflecting cavity, then, is effectively to modulate as a function of frequency and external-cavity length the reflectivity of the rear facet. R_{eff} replaces the factor R_2 in (2.7), and so the loss as a function of frequency is also modulated. This is shown qualitatively in Fig. 2.5(a). The frequencies of lowest cavity loss are separated by $c/2L_{ext}$, which is the free spectral range of the external cavity.

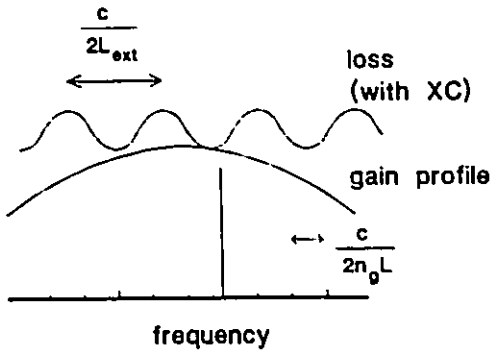

Figure 2.5(a)

An illustration of the gain and loss, and the laser and external cavity modes in an SXC laser

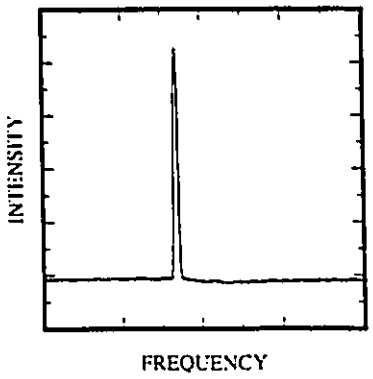

Figure 2.5(b)

The measured spectrum of the same laser used to obtain Fig. 2.3(b), but with a short-external-cavity of length $\approx 150\ \mu m$.

A longitudinal laser mode that is closest to the gain peak and to an external cavity mode is enhanced at the expense of the other laser modes. If the cavity length does not allow coincidence of laser mode and external-cavity mode, then the two laser modes with the highest net gain will compete. Although there exist many laser modes with low cavity loss, they are much further from the gain peak than the lasing mode if the free spectral range of the external cavity is larger than that of the laser.

The ratio of the intensity of the strongest side mode to the lasing mode is called the side mode suppression ratio (SMSR), and it is possible with a planar reflector and good alignment to attain a SMSR of $\approx 0.1\%$ to 1%. Further details of external cavity alignment tolerances and a calculation of R_{ex} is provided in [40].

Consecutive laser modes are selected by slightly varying the external cavity length (with a piezo-electric positioner, for example) so that a particular external cavity mode becomes coincident with the next laser mode. Eventually, as the length of the external cavity is varied continuously, the external cavity mode will move away from the gain peak and the adjacent external cavity mode will become closest to the gain peak. The effect of continuously changing the external cavity length in one direction is to periodically cycle through approximately the number of laser modes that is given by (2.11) .

There is an optimum external cavity length for single-mode operation. If L_{ex} is too large, then the separation of external cavity modes will not be sufficient to prevent two laser cavity modes that are separated by the free spectral range of the external cavity

from lasing at one time. If L_{ext} is too small, then the width of the external cavity mode becomes broad enough to allow several adjacent laser cavity modes to lase at one time. Experience indicates that for a 250 μm laser, an external cavity length of 80-200 μm results in good single mode operation.

A measurement of the effect of the SXC on the spectrum of a diode laser is shown in Fig. 2.5(b). The external reflector was placed ≈ 150 μm behind the rear facet of the laser.

2.4 Distributed-Feedback Diode Lasers

Another type of single-mode diode laser used in optical communications and spectroscopy is the distributed feedback (DFB) laser. Such a laser can have a very similar structure to the device shown in Fig. 2.1, but it incorporates a periodic variation of refractive index in or near the active region. This variation acts as a grating that influences the spectral output of the laser. The electric field propagating through the laser cavity is reflected back upon itself and interferes. If the period of the grating is chosen properly, the phase of the individual reflections of the electric field in the cavity cause the field to interfere constructively, which occurs near the Bragg wavelength, given by

$$\nu_B = \frac{M\pi}{\Lambda} \tag{2.13}$$

where M is the order and Λ is the period of the grating. The interference reduces the threshold gain of modes near the Bragg frequency, and only those longitudinal modes will lase. If the laser parameters are chosen carefully, then only one mode will lase. These devices therefore operate intrinsically in a single mode. Detailed theory of DFB laser design and operation is found in [29,30].

DFB lasers have been used extensively in spectroscopy (see references in Chapter 1). Their use is limited however, by their expense and by their limited availability at wavelengths other than those that are optimum for optical communications. The SXC lasers therefore may provide an alternative to DFB lasers. In Section 2.7 and Chapter 4, a comparison will be made of the properties of these lasers that are important in spectroscopic applications.

2.5 *Implementation of a Short-External-Cavity Laser*

The design and alignment of the SXC lasers used in the following chapters is now described. An isometric drawing of the short-external-cavity laser mounting scheme is shown in Figure 2.6. The lasers were mounted on an open chip carrier so that the back

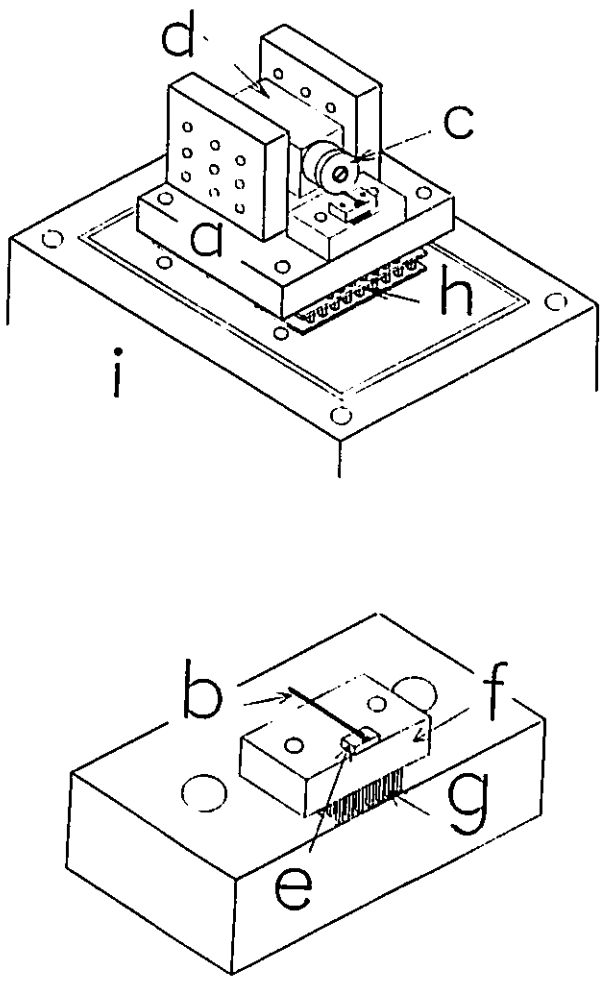

Figure 2.6

(a) An isometric drawing of the SXC assembly mounted in the tuning module and (b) an expanded view of the module showing the laser. 'a' is the SXC assembly, 'b' is the drill bit with attached mirror, 'c' is the washer which attaches drill bit to 'd', the piezo-electric positioner, 'e' is the laser chip carrier, 'f' is a copper block with embedded thermistor, 'g' is the small Peltier cooler, 'h' are the large Peltier coolers, and 'i' is the base of the tuning module.

facet of the laser was accessible. The carrier was mounted with thermal epoxy on a small copper block containing a thermistor (Fenwal Electronics 192-103LET-A01) that allowed the temperature to be monitored. The block was mounted in good thermal contact on a Peltier cooler (Melcor FC 0.45-32-05L), and the assembly was bolted to an aluminum bracket that could hold a piezo-electric translator (PZT) (Physik Instrumente Model 171). A small brass washer was bolted to one end of the PZT, and a #80 drill bit was epoxied to the washer. A small (250 x 400 x 400 μm) optically flat gold-coated mirror, which provided the optical feedback to the laser, was epoxied to the other end of the bit. The alignment of the mirror and PZT is accomplished by manipulating its position with an XYZ translation stage (Newport Model 460) that was mounted on a tilt-and-rotate stage (Newport Model 37). The channel of the aluminum bracket was 5 mm wider than the PZT, so a tilt of $\pm 6°$ could be obtained. The spectral output of the laser is monitored in real time during the alignment with a monochromator outfitted with a scanning mirror. The quality of alignment is determined by monitoring the side mode suppression ratio, the number of available SXC modes, and the single-mode power. Optimum alignment is achieved with a planar mirror when the mirror face is perpendicular to the optical axis of the laser. The alignment tolerance is not severe: useful SMSR and single-mode tuning can be obtained when the mirror is within 4° of parallel [40]. Once the desired alignment is achieved, the PZT is carefully clamped in place by the screws that are threaded through the sides of the aluminium bracket. Care must be taken not to pinch off the piezo stacks inside the PZT; this is easily avoided by

clamping the screws at the edges of the PZT rather than the middle. The external positioning apparatus can then be disconnected from the PZT. This method of mounting has been found to be very stable and compact. The entire apparatus fits in the palm of the hand, and can be transported safely for use in another location.

2.6 *Module for Enhanced Single Mode Tuning*

Frequency tuning of the SXC laser is most easily achieved by altering its temperature, which alters the frequency of the gain peak. To achieve a large range of frequency tuning, it is therefore necessary to the alter the temperature of the laser over as large a range as possible. A module was designed [38] that can alter the laser temperature from -80 °C to well above the temperature that most diode lasers can operate (~80 to 100 °C). The aluminum bracket that holds the SXC laser is bolted in the module in thermal contact with a pair of large thermoelectric heat pumps (Melcor CP2-31-06L and CP2-71-06L). The base of the module is hollowed out to allow water to flow through as a coolant that removes the heat from the underside of the large coolers. The assembly is covered and the vacuum chamber is pumped down to < 100 mTorr: above this pressure, electrical arcing may occur in the PZT. The electrical connections through the wall of the vacuum chamber to the coolers, the thermistor and the laser are made with a vacuum plug and connector (Amphenol 105-9 plug and 105-12

socket). The high-voltage connection to the PZT is not made through this connector so that there is no danger of arc across the insulation in the plug to the laser leads; such an arc could destroy the laser and the laser driver circuitry. Connection to the PZT is made through a second vacuum plug, also mounted in the wall of the chamber. The mode control techniques described in Chapter 3 can still be implemented when the laser is mounted in the vacuum chamber.

The cover of the module is outfitted with an aperture that holds a 5 x 5 cm plate glass window that allows the laser radiation to exit. The aperture is cut at an angle of 25°. to the optical axis of the laser to avoid optical feedback into the laser cavity. A neutral density filter can replace the plate glass if further isolation from feedback is required.

2.7 *Tuning Range of SXC Lasers*

The frequency-tuning range of both AlGaAs and InGaAsP lasers in the SXC configuration has been determined using the vacuum module. The measurement of this tuning range is straightforward. The diode laser is mounted in the aluminum bracket and installed in the vacuum module, which is evacuated to < 100 mTorr. Water is continuously flowed through the chamber under the large coolers. The small cooler directly under the laser can only alter the temperature by as much as $\pm$ 30 °C relative

to the temperature of the SXC assembly. If a further change in temperature is required, current is passed through the larger coolers, which reach thermal equilibrium with the laser and mount within several minutes. The small cooler stabilizes in a few seconds. The temperature is determined by monitoring the resistance of the thermistor, and is controlled by a resistive bridge in conjunction with electronic feedback circuitry. The laser wavelength and SMSR are monitored by a scanning monochromator. Small changes in the alignment and length of the SXC caused by thermal expansion or contraction can alter the SMSR and the number of available modes. At each temperature, the highest and lowest attainable single mode wavelength (SMSR $< 0.5\%$) is recorded. As the temperature is lowered, care was taken to reduce the laser injection current, since the laser threshold drops exponentially with temperature. For all measurements, the laser current was kept at $1.3I_{th}$. Four to eight modes were typically accessible over the entire temperature range in which the SXC lasers were operated.

An illustration of the frequency tuning of an InGaAsP laser operating at 1500 nm is given in Figure 2.7. This laser tuned over 190 cm^{-1} (34 nm) with a temperature variation of -70 °C to 60 °C. Although the number of available modes does change somewhat with temperature, there were no gaps in frequency coverage over this region: the laser could be tuned in steps of a few wavenumbers over the entire 190 cm^{-1} interval. This result is typical for InGaAsP SXC lasers, which have frequency tuning ranges of 70 to 250 cm^{-1} (12-45 nm). Differences in tuning ranges are observed even in lasers with the same structure from the same manufacturer. The origin of this difference in

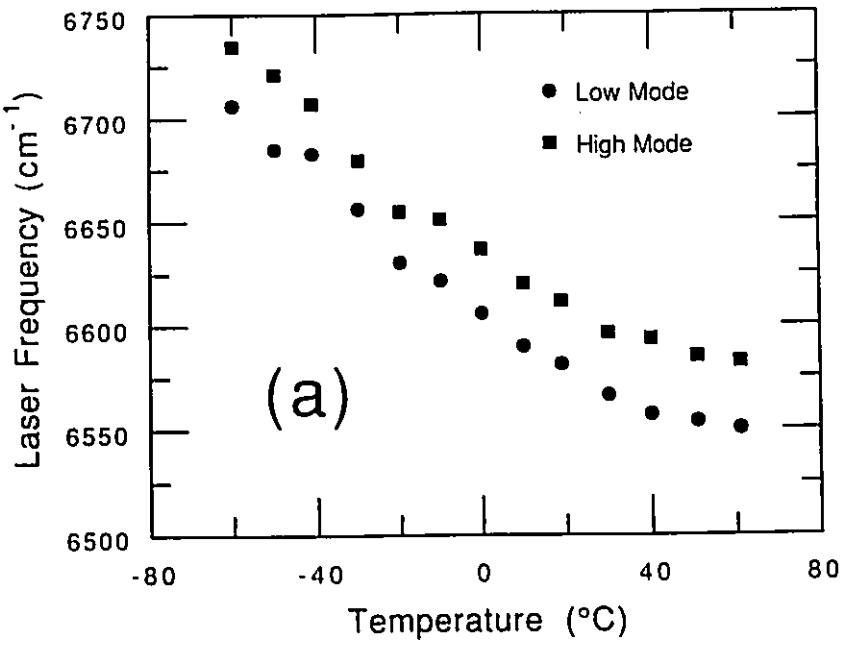

Figure 2.7

Single-mode tuning range of an InGaAsP SXC laser. The laser tunes over a spectral interval given by 4-8 laser modes that are selected with the SXC.

frequency tuning range is not known.

Similar measurements were made for AlGaAs SXC lasers operating at 760 nm. Much wider continuous ranges of 400-500 cm^{-1} (22-27 nm) were observed. The difference in tuning between InGaAsP and AlGaAs lasers is a consequence of the different temperature shift of the gain peak in these materials.

An InGaAsP distributed feedback laser (DFB) (without a short-external cavity) was also tested in the vacuum module. This laser tuned continuously over 50 cm^{-1} (9 nm) in a single mode before it hopped to multimode operation at an operating temperature of -30 °C, below which it continued to operate multimode (Fig. 2.8). The change in spectral characteristics of the DFB laser occurs when the frequency of the gain peak shift sufficiently far away from the Bragg frequency of the internal grating so that the Fabry-Perot modes at the gain peak have the highest net gain. The tuning range of the DFB laser is shown in Fig. 2.8.

2.8 Summary

The operation of both solitary and SXC diode lasers has been qualitatively described. The short-external cavity has the effect of modulating the reflectance of the rear laser facet as a function of frequency and external-cavity length. When an external cavity mode is coincident with a laser cavity mode near the gain peak, the laser mode

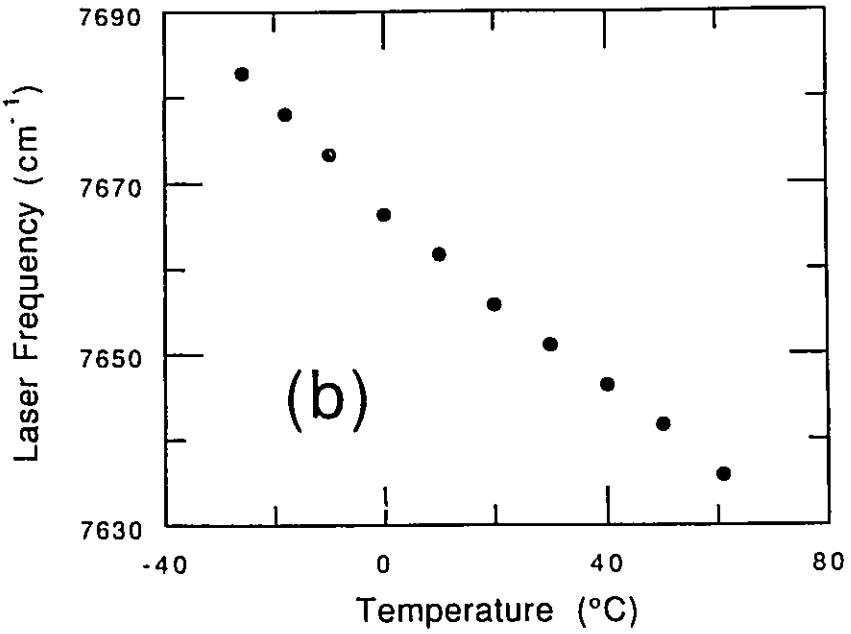

Figure 2.8

Single-mode tuning range of an InGaAsP distributed feedback laser.

is reinforced at the expense of the other laser modes, causing the laser to operate in a single longitudinal mode. The realization of an SXC laser has been described, and a module that allows extended temperature operation of the lasers has been characterized. The extended temperature tuning allowed InGaAsP lasers to be tuned up to 250 cm^{-1} (45 nm) in overlapping segments of a few wavenumbers with no gaps in frequency coverage. AlGaAs lasers could similarly be tuned by 500 cm^{-1} (27 nm). The continuous tuning range of the SXC lasers rivals other methods of controlling the frequency tuning range of semiconductor diode lasers (see Chapter 1), but is considerably simpler and more adaptable to off-the-shelf laser diodes.

CHAPTER 3 - MODE CONTROL OF SXC LASERS

3.1 Introduction

The short-external-cavity lasers described in Chapter 2 are extremely susceptible to perturbations in the optical length of the laser and in the external cavity length. A hop from one longitudinal laser cavity mode to the next is induced if the external cavity length changes by

$$\Delta L_{ext} = \frac{\lambda}{2N} \tag{3.1}$$

where λ is the laser wavelength and N is given by (2.11). For an SXC laser with λ=1.3 μm and N=8, a change in length of only 81 nm will induce a change in longitudinal mode. In addition, when the frequency of the gain peak is tuned, for example, by altering the laser temperature, the optimum value of L_{ext} for a particular mode will change and a mode hop may again be induced. Methods of dynamic control of the external

cavity length were developed to address this problem [23,41,42,43,44]; each method can be applied to specific lasers in specific circumstances.

A very convenient technique to control longitudinal modes was developed by Cassidy and Bonnell [23,44]. This approach exploits the change in voltage across the laser diode when L_{ext} is altered from its optimum value for single mode operation. When the external cavity is optimally aligned for single mode operation the threshold current of the laser, the separation of the quasi-Fermi levels and therefore the voltage across the laser diode are minimized. When L_{ext} drifts from its optimum value, the voltage across the laser increases and this change can be detected and processed to restore the external cavity length to optimize single-mode operation. This method is elegant in that it requires no external optics to implement, but it suffers from a low signal-to-noise ratio (SNR) of the laser voltage. Although it has been used successfully, this technique is difficult to implement and has a relatively slow response time. An improved method is therefore desirable.

This chapter describes a new method of controlling the longitudinal mode behaviour of SXC lasers [45]. The discriminating signal for mode control is provided by interference fringes in the far field intensity distribution of the lasers. The origin and behaviour of the fringes in the far-field of the SXC lasers was explained with a simple model of interfering wavefronts. The discriminating signal produced by the fringes was characterized and used in a negative feedback loop to control the external cavity length so that mode hops were suppressed. The operation of this control system was analyzed,

and the stability and response time determined. A comparison was made of the SNR and response time of this technique with the voltage control method.

3.2 Origin of the Interference Fringes

3.2.1 Observations of the Far Field of SXC Lasers

The far field of an SXC laser operating in a single longitudinal mode is seen in Fig. 3.1, which is a photograph of an IR viewing card onto which the laser output is projected. This photograph reveals that the far field consists of two distinct patterns of semi-circular rings that blend together near the plane containing the active region of the laser. The rings in the upper half of the photo have a smaller angular separation than those in the lower half. The pattern in Fig. 3.1 appears most clearly when the laser is operating in a single longitudinal mode, and is not present when the external cavity is removed. The image of the rings is real-- no imaging optics were used. The rings are reminiscent of the interference pattern called Newton's rings [46], and it will be demonstrated in the next section that the rings in the far field of the SXC lasers are indeed the result of a similar type of interference caused by the light from the front and back facets of the SXC laser.

Figure 3.2(a) shows a measurement of the far field of the same SXC laser

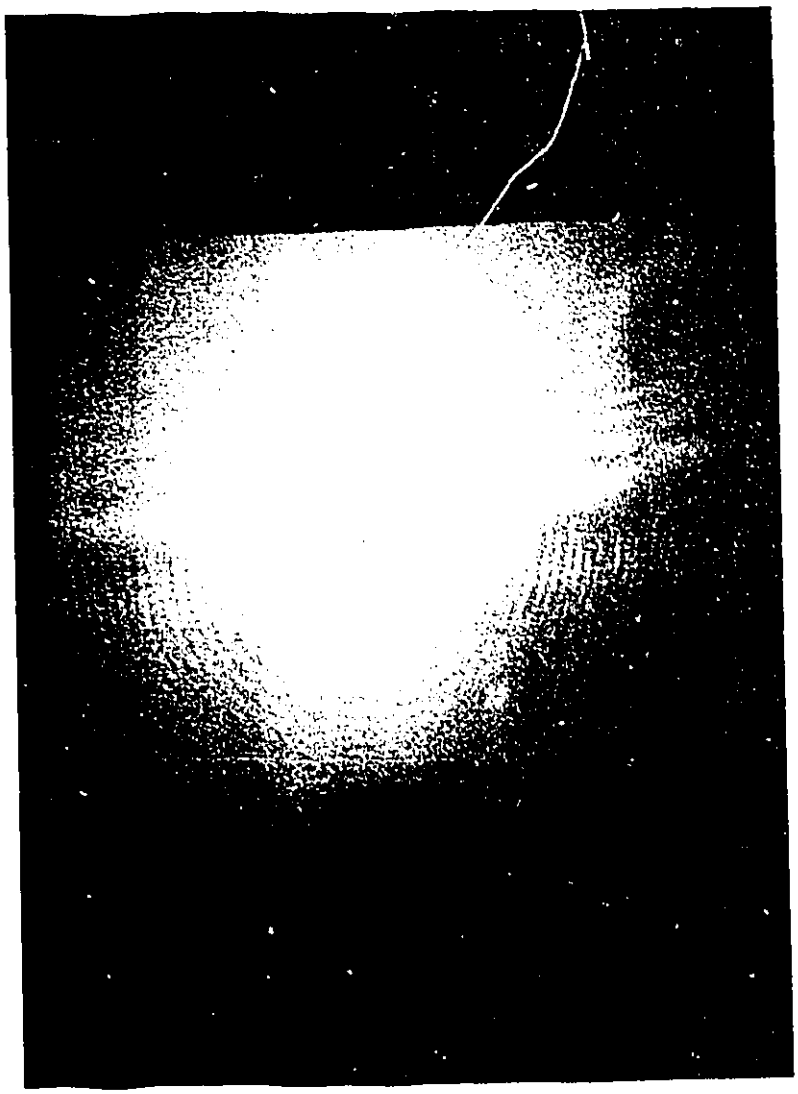

Figure 3.1

A photograph of an IR viewing card onto which the emission of an SXC laser is projected. The upper half of the fringe pattern is above the laser axis (see Fig. 3.4). The surface of the card subtends a 25° x 25° angle.

used to produce Fig. 3.1. Again, the laser was operating in a single longitudinal mode. This scan is a vertical slice through the centre of the interference pattern in Fig. 3.1. To obtain these data, the laser was rotated about an axis in the plane of the active region and the light was measured with a 1 mm^2 area detector placed 250 mm away from the laser, giving an angular resolution of 0.25°. The origin for θ was chosen to be the laser axis, which was taken to be the position at which the intensity of the far-field of the solitary laser is maximum. It will be demonstrated that the fringes lying below the laser axis in Fig. 3.1 and Fig. 3.2(a) (at positive θ) are produced by the light from the external reflector passing through the laser cladding and substrate and interfering with light from the front facet. The fringes above the laser axis (negative θ) are produced when the back-reflected light passes over the top of the laser and interferes with the light from the front facet. The transition between the two cases occurs near $\theta=0$ because the active region of this laser is only 2 μm from the top surface of this laser. The laser is 142 μm thick.

The linear fringes seen in Fig. 3.1 are caused by diffraction of the back reflected light by the top edge of the laser. This effect also appears in Fig. 3.2(a) as a modulation of the intensity of the fringes at negative θ.

Figure 3.3 shows measurements of the far field of an SXC laser operating on three adjacent longitudinal laser cavity modes which are labelled 1, 2 and 3. The fringes above the laser axis are shifted in position upon a change of mode, while the fringes below the laser axis do not perceptibly shift position. The change in position of

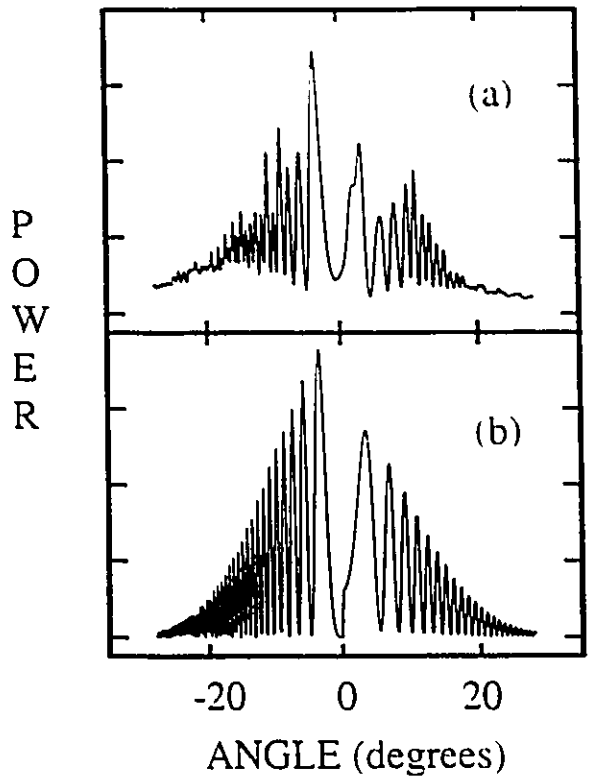

Figure 3.2

(a) Measured and (b) predicted far field intensity distributions of an SXC laser with L_1=254 μm, L_{ext}=92 μm, n_a=3.5 and n_c=3.4. Negative angles correspond to regions above the laser axis. This is a vertical cross-section of the far field of the same laser used to produce Fig. 1.

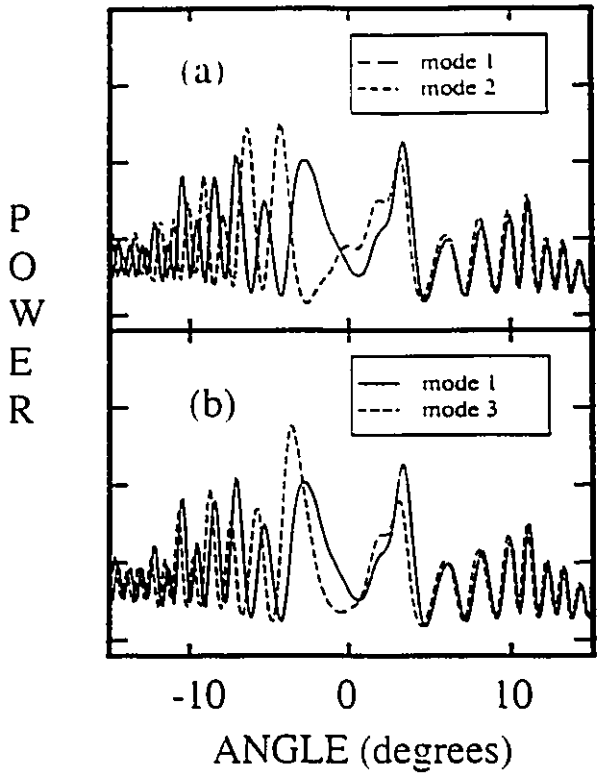

Figure 3.3

(a), (b) The far field intensity distribution of an SXC laser for 3 consecutive longitudinal modes labelled 1,2 and 3 in order of increasing frequency.

the fringes for adjacent longitudinal modes immediately suggests a method to detect and possibly control L_{ex} to prevent a mode hop. This possibility will be considered in Sec. 3.3.

The laser used for Fig. 3.1, 3.2 and 3.3 was mounted on a heat sink with the active region near the top of the laser (active region up). When an SXC laser with the active region near the bottom of the laser was observed, the far-field pattern was quite different. The far-field of the laser below the axis was unchanged with the insertion of the external cavity and no semi-circular fringe pattern was observed. Above the laser axis, a semi-circular fringe pattern was observed, but these fringes did not shift position upon change of the laser mode. This is an important consideration: the laser must be mounted active region up to observe the change in fringe position that can be used for mode control.

The above observations have been recorded for several different InGaAsP lasers mounted with the active regions up or down, and for lasers with both gain-guiding and various index guiding structures.

3.2.2 A Model of the Interference Fringes

A simple model to explain the fringes can be obtained from Fig. 3.4, which are schematic diagrams of the path of light emitted from an external cavity laser to a point

P some distance D away. For an isolated diode laser, the light emitted from each facet is phase-related but propagates in opposite directions. The insertion of the external mirror, however, reverses the direction of the light from the rear laser facet and this light can interfere with light from the front facet. Light will pass over the laser (Fig. 3.4(a)), or through the laser substrate (Fig. 3.4(b)) to point P. For InGaAsP lasers, the substrate is transparent at the frequency of laser emission.

Consider Fig. 3.4. A plane wavefront of wavelength λ is incident upon the front facet of the laser from within the laser itself. Part of the wavefront passes through the front facet at angle θ_1 to the laser axis and propagates to point P where it has intensity $I_1(\theta_1)$. The light that is reflected backward by the front facet propagates through the laser cavity, leaves the laser at angle θ_2, propagates through the external cavity and is reflected by the external mirror to point P where it has intensity $I_2(\theta_2)$. The two wavefronts will interfere at P shown in Fig. 3.4 with intensity

$$I_p(\theta_1,\theta_2) = I_1(\theta_1) + I_2(\theta_2) + 2\sqrt{I_1(\theta_1)I_2(\theta_2)}\,\cos\delta \qquad (3.2)$$

where

$$\delta = \frac{2\pi}{\lambda}\,\Lambda \qquad (3.3)$$

is the relative phase of the two wavefronts and Λ is the optical path difference between the wavefronts. $I_1(\theta_1)$ and $I_2(\theta_2)$ describe the usual Gaussian dependence of intensity with

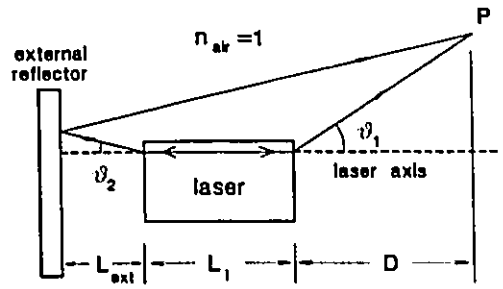

Figure 3.4(a)

A schematic diagram for tracing the path of the wavefronts in an SXC laser above the laser axis.

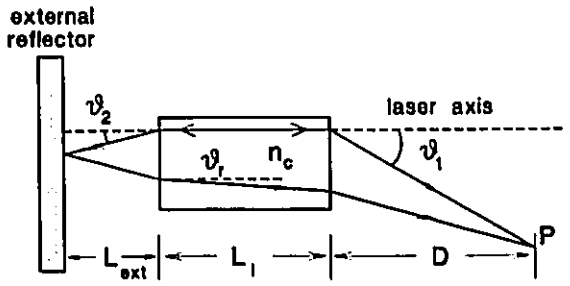

Figure 3.4 (b)

Same a Fig. 3.4(a), but the rays are traced through the laser cladding and substrate.

angle in the diverging beam of a diode laser. In Fig. 3.4(a), the optical path difference is, assuming the refractive index of air is unity,

$$\Lambda_{air} = n_a L_l + \frac{2L_{ext} + L_l + D}{\cos\theta_2} - \frac{D}{\cos\theta_1} \tag{3.4}$$

and in Figure 3.4(b),

$$\Lambda_c = n_a L_l + \frac{2L_{ext} + D}{\cos\theta_2} + \frac{n_c L_l}{\cos\theta_r} - \frac{D}{\cos\theta_1} \tag{3.5}$$

where

$$\theta_r = \text{arc sin} \left[\frac{\sin\theta_2}{n_c} \right] \tag{3.6}$$

is the angle of refraction in the laser substrate and the subscripts 'a','air' and 'c' denote the path difference through the active region, air and substrate, respectively.

If $D >> 2L_{ext}+n_cL_l$, which is the case for the measurements presented in Sec. 3.2.1, then $\theta_1 \approx \theta_2 \equiv \theta$, and (3.4) and (3.5) become

$$\Lambda_{air} \cong n_a L_l + (2L_{ext} + L_l)\cos\theta \tag{3.7}$$

$$\Lambda_c \cong n_a L_l + 2L_{ext}\cos\theta + n_c L_l \cos\theta_r \tag{3.8}$$

and for constructive interference at fixed θ,

$$\Lambda_i = m_i \lambda \tag{3.9}$$

where i=air or c, and m_i is a positive integer. Equation (3.9) describes fringes of equal inclination in the far field of the laser, which are observed in Figure 3.1.

Figure 3.2(b) is the far field of an SXC laser predicted by (3.2)-(3.6). The length of the laser and external cavity were chosen to approximate the laser that produced the measured far field of Fig. 3.2(a). Refractive indices of 3.5 and 3.4 were used for the active and cladding layers, respectively, and the $1/e^2$ points of the Gaussian profile of the far field in the model were chosen to fit the experimentally measured profile of the solitary laser. Comparison of Figs. 3.2(a) and 3.2(b) indicate that the above analysis can indeed explain the features of the far field of external cavity diode lasers.

The model also explains the change in angular position of the fringes when a mode hop occurs. Consider the change in relative phase between the wavefronts at point P in Fig. 3.4. In Fig. 3.4(a), if $D >> 2L_{ext}+L_l$, then the relative phase at P is given by (3.3) and (3.7):

$$\begin{aligned} \delta &= \frac{2\pi}{\lambda} \Lambda_a \\ &= \frac{2\pi}{\lambda} [n_a L_l + (2L_{ext} + L_l) \cos\theta] \end{aligned} \tag{3.10}$$

The resonance conditions for the laser cavity and external cavity are, respectively,

$$n_a L_l = p \frac{\lambda}{2} \tag{3.11}$$

and

$$L_{ext} = q \frac{\lambda}{2} \tag{3.12}$$

where p and q are positive integers. Substituting (3.11) and (3.12) into (3.10) gives

$$\delta = \pi[p + (2q + \frac{p}{n_a}) \cos\theta] \tag{3.13}$$

When L_{ext} is altered to cause a shift to the next longitudinal mode (of shorter wavelength), then p→ p+1 and q→ q and the change in relative phase at P is

$$\begin{aligned} \Delta\delta_1 &= \delta(p+1) - \delta(p) \\ &= \pi + \frac{\pi}{n_a} \cos\theta \end{aligned} \tag{3.14}$$

If the SXC laser is shifted by two longitudinal modes, then p→ p+2, q→ q, and

$$\begin{aligned} \Delta\delta_2 &= \delta(p+2) - \delta(p) \\ &= 2\pi + \frac{2\pi}{n_a} \cos\theta \end{aligned} \tag{3.15}$$

For $n_a \approx 3.5$ and small θ, $\Delta\delta_1$ is therefore $\sim 1.3\pi$. This is approximately the shift that

is observed in Figure 3.3.

For the case described by Figure 3.4(b), a similar line of reasoning gives

$$\Delta\delta_1 = \pi(1 + \frac{n_c}{n_a}\cos\theta_r) \tag{3.16}$$

and

$$\Delta\delta_2 = 2\pi + 2\pi\frac{n_c}{n_a}\cos\theta_r \tag{3.17}$$

For most diode lasers, $n_c/n_a \approx 1$, so for small θ the phase shift at P is almost a multiple of 2π, regardless of the longitudinal mode; hence, the fringe pattern remains nearly unchanged. Again, this is confirmed by the observations in Figure 3.

Equations (3.14)-(3.17) describe the change in phase of the fringes when a longitudinal mode hop occurs. In the limit of large n_a, for fringes above the laser axis, the phase shifts by π (the fringe pattern inverts) when the mode changes from p to p+1, p+3,... . For a mode hop from p to p+2, p+4,... the fringes would have a phase shift of ≈ 0, and these modes would produce the same fringe pattern. If $n_a/n_c = 1$, the fringes below the axis would always be shifted by a multiple of 2π for any mode hop, so this fringe pattern would not change upon a mode hop. For real InGaAsP lasers, of course, n_a is only ~ 3.2 to 3.5 and $n_a/n_c \approx 1$ so the phase does not alternate by exactly π with successive mode hops, as in the above argument for large n_a.

This analysis shows that the change in the fringe pattern is caused by the change

of relative phase between the laser facets, and not the change in wavelength of the laser. If there are an integral number of wavelengths in the laser cavity, the facets are out of phase by π; for a half-integral number of wavelengths in the cavity, the facets are in phase. Hops from one longitudinal mode to the next alternate between these two resonance conditions, and this is manifested in the change of the apparent radii of the interference maxima above the laser axis. The positions of the maxima do vary with wavelength, but this is a much smaller effect because of the small difference in wavelength between the laser modes (~ 5 cm^{-1}) relative to the frequency of the laser (~ 7000 cm^{-1}).

3.3 Discrimination Signal for Longitudinal Mode Control

3.3.1 Mode Control using Interference Fringes

SXC lasers operate in one dominant longitudinal mode, which has 100 to 1000 times more power than the adjacent side modes. As shown above, each longitudinal mode has a particular interference pattern, so the laser far field is actually an intensity-weighted sum of the interference patterns of all modes. If some perturbation causes a suppressed mode to gain intensity at the expense of the dominant mode, then the total far field distribution will be altered. This is the origin of the discrimination signal for mode

control of SXC lasers.

The optical arrangement for mode control is straightforward. The laser is set to operate in a particular mode and a portion of the laser emission is split off and sent to a detector placed in the far field above the laser axis at a point of constructive interference. The angular size of the detector must be less than that of the interference maximum. If the external cavity drifts in one direction, the intensity of a mode adjacent to the main mode increases, resulting in a change in the angular position of the fringes and a decrease in power on the detector. The power decrease is also observed if the external cavity drifts the other way. The derivative of this power signal is obtained by dithering the length of the external cavity and demodulating the detector signal with a phase-sensitive detector referenced at the dither frequency. The derivative signal indicates both the magnitude and direction of the drift, so it can be used in a feedback loop to restore the external cavity length to its original position, regardless of the direction of drift. A schematic of the feedback loop to achieve mode control is shown in Fig. 3.5.

To implement mode control, it is necessary to monitor a fringe that is above the laser axis, since these fringes exhibit a much greater shift in position upon a change of mode than the fringes below the laser axis. It does not matter which of these above-axis fringes are used, as long as the detector has sufficient angular resolution to distinguish the chosen fringe. Because the relative phase between the interfering wavefronts does not shift by exactly π each time the mode is changed, the detector must be slightly realigned each time the laser is operated on a different mode so that the optimum discrimination

signal is obtained.

Equation (3.9) indicates that there is a very small change in the angular position of the interference maxima when the laser frequency changes by the equivalent of one longitudinal mode spacing (~ 5 cm^{-1}). As mentioned before, it is the change in relative phase of the light from the laser facets on a mode hop that causes the shift in fringe position. This is important because the discrimination signal will not change appreciably when the laser frequency is tuned over an entire mode spacing. It is therefore possible to control a mode while the laser is tuned over one or more mode spacings. For the lasers that have been tested to date, each longitudinal mode can be tuned over at least a mode spacing , leaving no gaps in frequency coverage over the range of tuning of the gain peak of the laser. Complete frequency coverage of 100-250 cm^{-1} is therefore possible by temperature tuning the laser [38].

3.3.2 Comparison with Laser Voltage Mode Control

The use of interference fringes in the far field of the SXC lasers is a significant improvement over the use of the laser voltage for longitudinal mode control. The discrimination signal obtained from the interference fringes in the far field has a significantly better SNR than the voltage signal used in past work with SXC lasers.

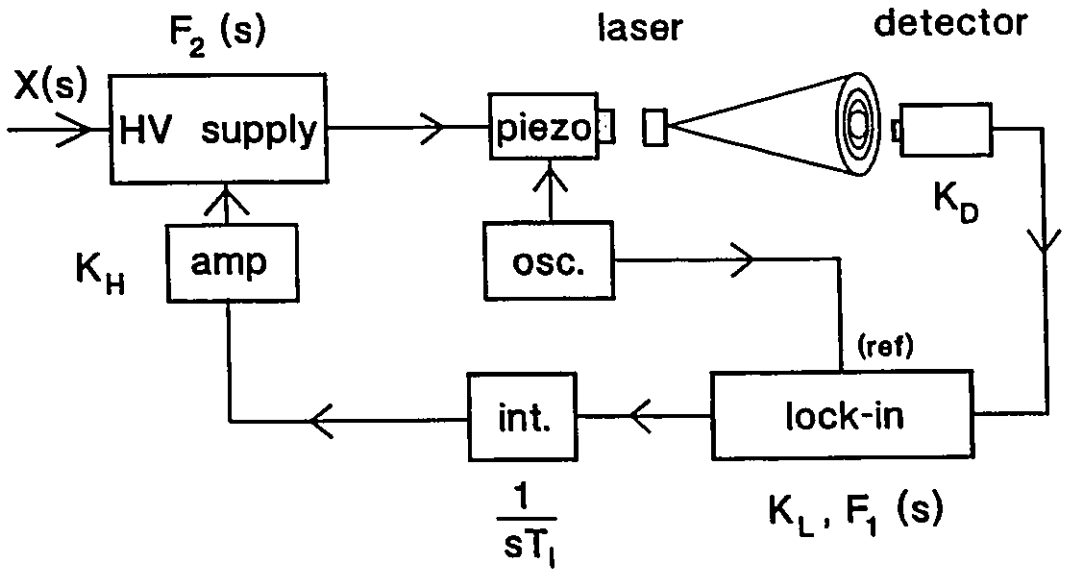

Figure 3.5

A schematic diagram for the feedback control system to maintain single mode operation of an SXC laser.

Figure 3.6 compares the signals taken with the same laser on the same mode while L_{ex} was moved through one FSR of the laser. The higher SNR using the fringes means potentially faster and more stable operation of the negative feedback loop to control the modes (Sec. 3.4).

The hardware requirements are more exact for the detection of laser voltage. Best results are obtained using a low-noise differential preamplifier before the signal is fed to a lock-in amplifier. The modulation of the laser current required for harmonic detection also introduces a modulation of the laser voltage which tends to overload the lock-in that detects the laser voltage. In contrast, the detection of changes in the far field requires no preamplification and there is reduced potential for lock-in overload when laser current modulation is introduced. Some additional equipment is needed to implement mode control with the interference fringes: it is necessary to introduce a beamsplitter and detector into the optical arrangement of an experiment. The detector must be translated about the far field to obtain the optimum discrimination signal for each mode. A small fraction of the total laser emission is required for a discrimination signal: typically only 5% of the laser emission was split off to obtain very fast and stable feedback loop operation. The requirement of an extra detector also detracts from the compactness of the SXC laser itself, but the improvement in control of the modes may for some applications compensate for this disadvantage. However, it may indeed be possible to design a compact, self-contained SXC laser module that allows mode control using the far-field fringes, although this possibility has not yet been pursued.

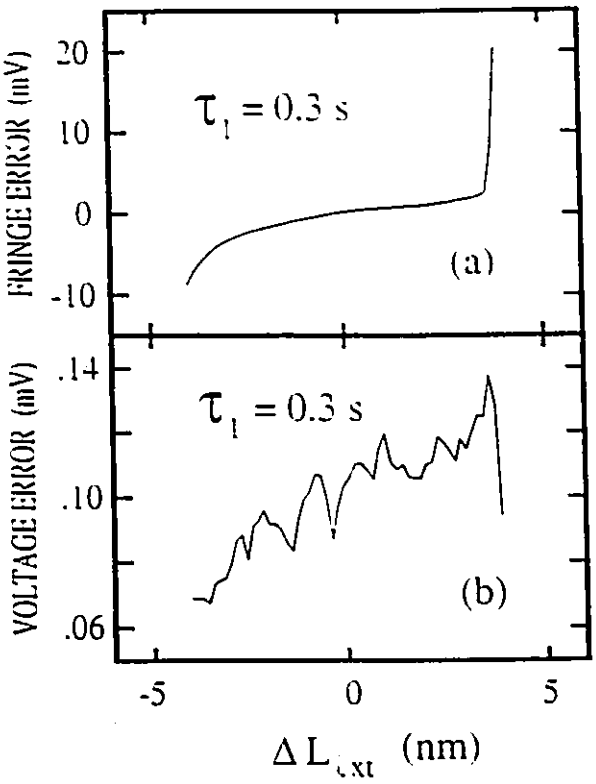

Figure 3.6

The discrimination signal from (a) the far field interference fringes and (b) the laser voltage for the same longitudinal mode of an SXC laser. The external cavity dither frequency was 3.85 kHz.

3.4 Analysis of Feedback System for Mode Control of SXC Lasers

3.4.1 Implementation of Feedback Control of SXC Lasers

A schematic of the system for longitudinal mode control of SXC diode lasers is shown in Figure 3.5. The loop uses the discrimination signal obtained from the far-field interference fringes to maintain the optimum external cavity length for single mode operation. The detector monitors the change in the fringe position, and the resulting signal is passed to a lock-in amplifier referenced to the dither frequency of the external cavity. The output of the lock-in indicates both the magnitude and direction of the displacement of the external cavity away from its optimum position. This signal is then integrated before it is fed back into the high voltage amplifier that controls the piezoelectric positioner onto which the external mirror is attached. With this simple feedback control system, it is possible to maintain single mode operation by correcting for perturbations in the optimum value of L_{ext} caused by laser frequency tuning, temperature changes, thermal or mechanical drift, or mechanical shocks and vibrations. Settling times as fast as 15 ms have been obtained by optimizing the operation of the feedback loop.

3.4.2 Time Response of Mode Control System

The goal of the feedback loop is to provide the voltage v_0 to the piezoelectric positioner that will establish the optimum external cavity length for single mode operation. If the voltage to the positioner is not v_0 but some other voltage v, then an error voltage $e(v_0-v)$ will arise to cause the system to evolve in time toward a condition of zero error. If e vs. v_0-v is linear, the time response v(t) of this system is described by a linear differential equation which can be solved for particular feedback loop parameters. This approach indicates how the system responds, but offers no immediate insight into how specific parameters, such as loop gain, influence its behaviour.

Instead of the differential equation of motion of the loop, consider the Laplace transform of this equation. If a voltage X(s) is input to the piezo positioner, the Laplace transform of voltage response of the entire system is

$$V(s) = H(s)\, X(s) \tag{3.18}$$

where H(s) is the transfer function of the system. Figure 3.5 indicates the transfer function of each component, and the system's total transfer function is given by [47]

$$H(s) = \frac{F_2(s)}{1 + K_D F_1(s) K_L \frac{1}{sT_I} K_H F_2(s)} = \frac{sF_2(s)}{s + AF_1(s) F_2(s)} \tag{3.19}$$

The loop gain A is

$$A = \frac{K_D K_L K_H}{T_I} \tag{3.20}$$

where K_D, K_L, and K_H are the voltage gains of the detector, lock-in amplifier, and high-voltage (HV) amplifier respectively, and T_I^{-1} is the gain of the integrator. The transfer functions of the filter of the lock-in amplifier and the high-voltage supply are $F_L(s)$ and $F_H(s)$. The lock-in filter has a 6 dB/octave rolloff, and can be described by

$$F_L(s) = \frac{1}{1 + s\tau_1} \tag{3.21}$$

where τ_1 is the lock-in time constant. If a 12 dB/octave rolloff is used, the transfer function must be modified accordingly. The HV supply has a time response that can also be approximated by a 6 dB/octave rolloff, and so

$$F_H(s) \cong \frac{1}{1 + s\tau_2} \tag{3.22}$$

where the effective time constant is $\tau_2 \approx 1.2$ ms for this particular HV supply. The piezoelectric positioner also has a time response, but its time constant is an order of magnitude smaller than τ_1 or τ_2 and will be disregarded for this analysis.

If X(s) and H(s) are known, then the time response of the system can be found from

$$v(t) = v_0 + \mathcal{L}^{-1}\,(H(s)\,X(s)) \tag{3.23}$$

The solution of v(t), for certain forms of H(s) and X(s), is a sinusoidal oscillation with an amplitude that exponentially increases or decreases in time, depending on the location in the s-plane of the poles of H(s). For stable operation, the poles must be located in the left-hand side of the plane, and the amplitude of the oscillation will decrease in time. An analysis of the transfer function provides the qualitative behaviour of the system without the need for solving for v(t). The stability of the system is found from the characteristic equation [47],

$$\begin{aligned} D(s) &= s + AF_H(s)\,F_L(s) \\ &= 0 \end{aligned} \tag{3.24}$$

where D(s) is simply the denominator of the transfer function of (3.19). Using (3.20)-(3.22), the stability of the system is determined by applying the Routh stability criterion [47] to (3.24), which requires that

$$A < \frac{\tau_1 + \tau_2}{\tau_1 \tau_2} \tag{3.25}$$

for the system to evolve to a finite steady-state value. Equation (3.25) gives the stability condition in terms of known parameters of the system.

Figure 3.7(a) shows the solution of (3.23) for a unit step perturbation to the optimum voltage for single mode operation. For such an input, X(s)=1/s in (3.23). Time constants of τ_1=1 ms, τ_2= 1.2 ms and a gain of A=650 s^{-1} were used. This choice of gain and time constant results in slightly underdamped oscillations, with a settling time of ~40 ms. Figure 3.7(b) shows the measured response of the control system for a unit step perturbation using the same value of τ_1, τ_2 and A used in Fig. 3.7(a). The output of the HV supply that controlled the piezoelectric positioner was monitored to obtain Fig. 3.7(b). The agreement between model and measurement is not exact, but the general behaviour of the loop response can be reproduced. If the gain in the calculated response was ≈25% larger, then theory and experiment agree quite closely. The discrepancy between the model and experiment likely arises from the approximation made in (3.22); in fact, the HV supply does not exactly follow a 6 dB/octave roll-off. Still, the model presented here can reproduce the trends in behaviour of the feedback system, and is valuable for understanding the behaviour of the system and optimizing its behaviour.

Approximately 5% of the laser emission was split off to obtain this mode control response. The underdamped oscillations in Fig. 3.7 are shown for illustrative

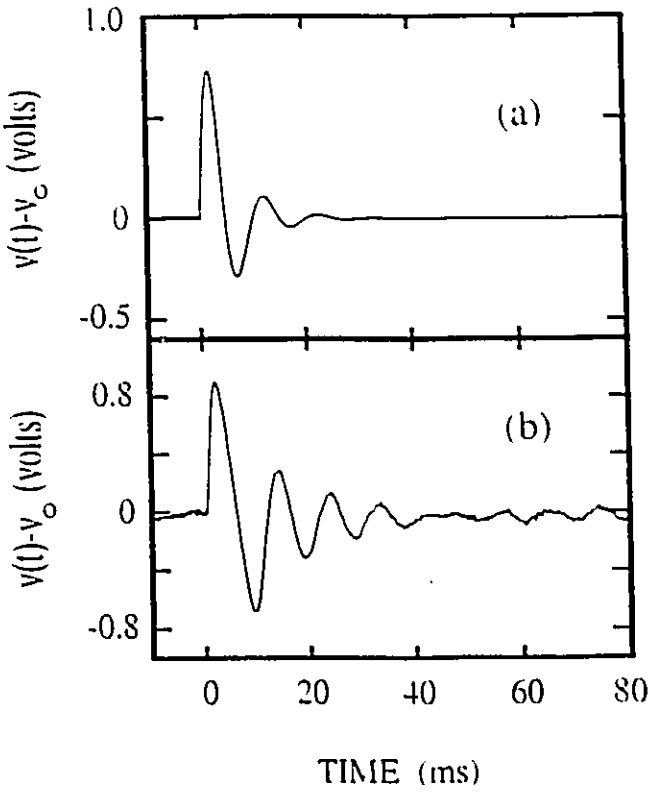

Figure 3.7

(a) Predicted and (b) measured time response of the control system in Fig. 5. The loop gain is 650 s^{-1}, τ_1=1 ms and τ_2= 1.2 ms.

purposes: if A≈260, τ_1=1 ms and τ_2= 1.2 ms, a critically damped response was obtained with a settling time of 15 ms.

3.4.3 Compensation

The response time that was obtained with the mode control system is limited by the values of τ_1 and τ_2. The minimum time constant of the lock-in amplifier is 1 ms, and the effective time constant of the HV supply is 1.2 ms. It is possible to overcome the limits imposed by the time response of these components and increase the time response of the system by using a lead compensation circuit, shown in Figure 3.8.

When the lead compensator is placed in the feedback arm of the control system, then the characteristic equation becomes

$$D(s)=s+\frac{A(s+a)}{(1+s\tau_1)(1+s\tau_2)(s+b)} \qquad (3.26)$$

and a proper choice of a and b can have the effect of replacing one root of the characteristic equation with another. For example, the minimum time constant τ_1 of a lock-in may be too large to achieve a desired response time. Increasing the gain of the system will increase the period of oscillation but will also decrease the stability. If,

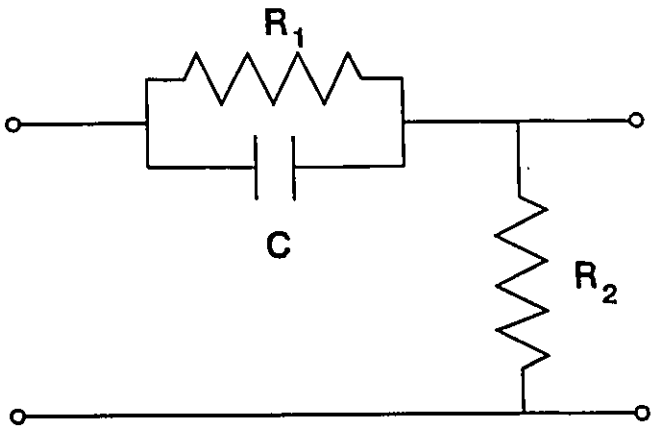

$$\frac{V_{in}}{V_{out}} = \frac{(s+a)}{(s+b)}$$

$$a = \frac{1}{R_1 C}$$

$$b = \frac{1}{R_1 C} + \frac{1}{R_2 C}$$

Figure 3.8

Schematic diagram and Laplace transform of a lead compensator used to enhance the response time of the feedback control system.

however, a is chosen to be $1/\tau_1$ and b=10a, then the factor $(1+s\tau_1)$ in (3.26) is replaced by $(10+s\tau_1)$, and the pole of the system is moved to the left in the s-plane causing the oscillations to decay much more quickly. This technique has been shown to work in the feedback system for mode control, and is a useful technique for compensating an element of the system that is too slow to achieve a desired response time.

3.4.4 Discussion

The compensation technique can in principle be used to improve the maximum response time of 15 ms that was achieved with this system. However, it was found that if the 1 ms lock-in time constant was compensated with a smaller value, then too much noise would pass through the feedback loop and cause mode hops. The main source of noise was laser intensity fluctuations that are intrinsic in all semiconductor lasers. Reduction of this noise would require demodulation of the discrimination signal at a much higher frequency (MHz), but this frequency is limited to the kHz regime by the response of the piezoelectric positioner. Decreasing the bandwidth of the lock-in amplifier reduces the noise at the expense of stability and response time of the feedback loop. It is generally true, for example, that when 12 dB/octave filtering is used to increase the SNR, the stability and response of the feedback system are reduced. For most applications in spectroscopy and trace gas detection, the response time and stability provided by this feedback control system using the interference fringes is quite adequate. The trade off between response time and SNR depends on a given application.

The response time and stability of mode control using the fringes is markedly

superior to that using the laser voltage technique. The small SNR of the laser voltage requires a typical lock-in time constant of 1s with a 12 dB/octave rolloff. The response of the loop under these conditions is typically ~ 10 s, and it is difficult to correct for sudden perturbations in the external cavity length. In addition, the voltage signal is not acceptable for use in a feedback loop for some longitudinal modes on some lasers. However, the fringes appropriate for mode control are produced by most InGaAsP lasers that are mounted active region up, and the behaviour of the fringes does not depend strongly on the alignment of the external cavity.

Finally, it is expected that mode control using the far field fringes can be implemented with most SXC semiconductor diode lasers provided the active region is near the top of the laser. The fringes that are used are produced by the light from the front facet interfering with light from the back facet reflected over the laser by the external reflector. This situation will occur in any SXC diode laser, regardless of its composition.

3.5 Summary

The interference fringes in the far field of SXC semiconductor diode lasers have been described and explained. The interference occurs between light emitted from the front facet and light emitted from the back facet that is reflected forward by the external mirror. If the laser is mounted with the active region up, light from the back facet can (i) reflect over the laser or (ii) through the laser cladding and substrate; each of these instances produces a pattern of semicircular fringes of different radii. A change in

longitudinal mode causes little change in the radii of fringes in case (ii), but causes a substantial change in the apparent radius of the fringes produced by case (i). A simple model was devised that successfully explains the existence and behaviour of the fringes. It was shown that the change in apparent fringe radius in case (i) is caused by the change in relative phase between the front and back facets of the diode laser.

The behaviour of the interference fringes in the far field was used to implement a new method for longitudinal mode control of SXC InGaAsP diode lasers. The realization of a discrimination signal derived from the fringes was presented, and the signal was used in a feedback system to control the modes of the SXC lasers. The control system has a response time as short as 15 ms, and could prevent mode hops caused by drift, laser tuning or mechanical shock. The system allowed complete frequency tuning over the range of operation of the laser: there were no gaps in frequency coverage. Finally, the behaviour of the control system was analyzed to optimize the control system.

CHAPTER 4 -

AN ABSORPTION SPECTROMETER USING SXC LASER DIODES

4.1 Introduction

The tunability, narrow linewidth and high power of NIR diode lasers make them excellent radiation sources for use in molecular spectroscopy and spectroscopic applications. This chapter explores the suitability of SXC laser diodes described in Chapter 2 as tunable sources in an absorption spectrometer that can be used to make high-resolution and high-sensitivity spectroscopic measurements of molecular absorption transitions [48]. Mode control techniques described in Chapter 3 were used to enhance operation of the lasers. The factors that limit the sensitivity of the spectrometer were assessed, and strategies for the optimization of sensitivity were determined. Finally, a comparison will be made of the performance of DFB lasers and SXC lasers used as radiation sources in the absorption spectrometer.

4.2 *Implementation of the Spectrometer*

4.2.1 *Apparatus, Alignment and Detection Techniques*

The SXC laser mounted in the tuning module was used as the radiation source in an absorption spectrometer, which is shown in Fig. 4.1. The laser light was collimated with a broadband anti-reflection (AR) coated singlet lens, was passed through the absorption cell and was focused with another lens onto an InGaAs photodetector. Many absorption cells were used: the cell could be a simple glass tube 1-100 cm in length, or a multi-pass White cell with an effective path length up to 100 m. A beam splitter was used to send a fraction of the light, before it reached the absorption cell, to a scanning monochromator for wavelength calibration and monitoring of the spectral properties of the laser. When high-sensitivity detection was performed, the beam splitter was removed to reduce the amount of unwanted optical feedback to the laser. Careful alignment of all optical surfaces in the path was necessary to achieve maximum sensitivity: planar surfaces were tilted with respect to the optical axis, the laser beam was focused tightly onto the detector material only and not the surrounding case, and all components were cleaned to reduce scattered light. Neutral density filters were often used to reduce optical feedback and unwanted reflection between optical surfaces. The reduction in the intensity of the light is not a problem provided the laser beam noise exceeds the detector noise. Optical feedback can be a serious problem in a high

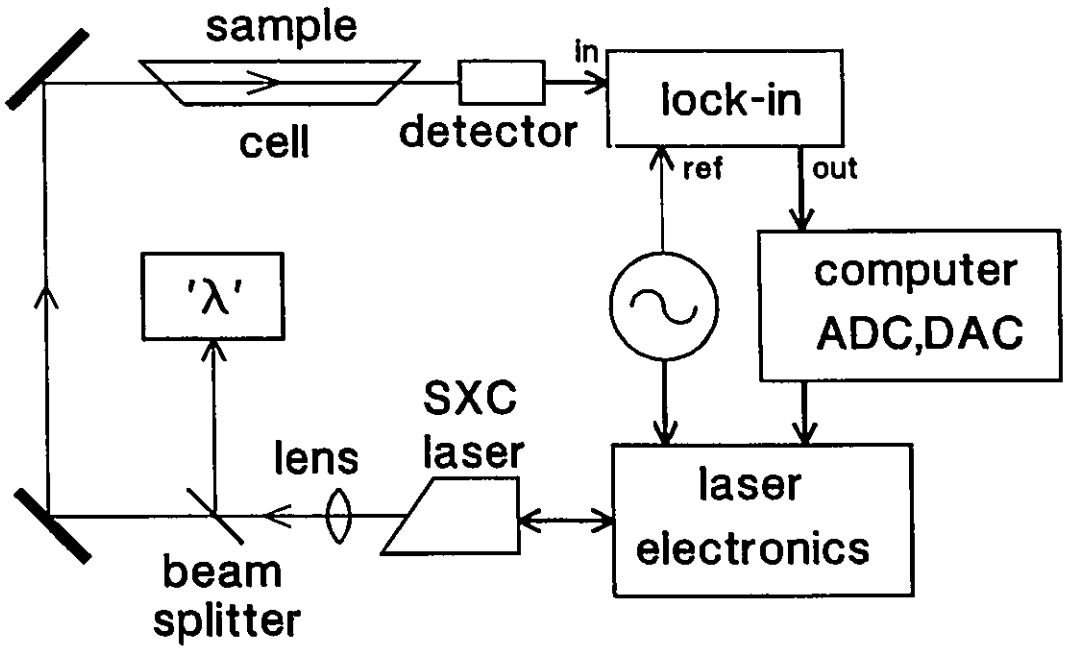

Figure 4.1

The layout of the SXC diode laser absorption spectrometer. The box labelled 'λ' refers to a monochromator or wave-meter, used to monitor the spectral output of the laser.

sensitivity and high-resolution spectrometer because of the degredation of the spectral purity of the laser's output [49].

Second-harmonic detection (2f) was used to obtain high-sensitivity spectra, since it is well-suited to diode laser operation [50]. With this technique, the laser frequency is modulated at audio frequencies, while the mean laser frequency is slowly tuned through an absorption feature. The detector signal is demodulated by a lock-in amplifier referenced at twice the laser modulation frequency. The resulting 2f signal of an absorption line is shaped approximately as the second derivative of the true line shape; the background 2f signal, away from the absorption feature, is ideally zero and thus independent of fluctuations in the laser power [51].

The optical frequency modulation of the SXC laser was accomplished by modulating the laser injection current at audio frequencies of typically 10 to 50 kHz. The mean laser frequency is tuned by slowly ramping the laser current or temperature. The choice of the amplitude of current modulation depended on the particular laser and the frequency width of the line that is to be detected. The optimum 2f signal is achieved when the amplitude of the frequency modulation is $2.2\Delta\nu_{1/2}$, where $\Delta\nu_{1/2}$ is the half-width at half maximum (HWHM) of the absorption line that is to be measured [50]. InGaAsP lasers have a current tuning response of $\approx$ -0.03 cm^{-1}/mA. For a pressure-broadened molecular transition, for example, the HWHM is typically $\approx$0.1 cm^{-1}, so the optimum current modulation amplitude would be 7 mA. AlGaAs lasers tuned $\approx$ -0.25 cm^{-1}/mA, so significantly less current modulation is required to achieve optimum modulation

amplitude for the same linewidth. The sweep rate of the laser frequency is limited by the time constant of the lock-in amplifier.

Although 2f detection should provide a zero background for absorption signals, there are always unwanted signals that appear in a 2f spectrum that arise because of the frequency modulation of the laser. These signals limit the detection of weak absorption features and are termed *modulation noise*. The peak-to-peak height of the 2f background away from an absorption signal is taken to be a measure of the modulation noise, and an equivalent absorption for this noise can be determined by comparing the size of the modulation noise to the size of a 2f absorption line of known absorption. In this way, the modulation noise is independent of laser power and the absorption strength of the line used to calibrate the noise. The main contributions to modulation noise will be discussed in the next section.

When the laser frequency modulation is turned off, the background noise is substantially reduced, but is still present. This is the laser *beam noise*, which is caused by random fluctuations in the laser power within the detection bandwidth. The beam noise is the fundamental limit to the sensitivity of the absorption spectrometer. The laser power fluctuation is caused in part by the random spontaneous photons emitted in the laser cavity. In addition, there is a 1/f component to the laser noise that falls off above $\approx$10 MHz. It is possible to achieve shot-noise-limited sensitivity if the laser is modulated at $\approx$50-500 MHz: this is one advantage of the so-called two-tone frequency modulation spectroscopy (TTFMS) technique [52]. However, TTFMS is still affected

by the same type of modulation noise that is observed with 2f detection, and consequently the shot-noise limit is very difficult to reach. Although absorptions as small as 10^{-5} can be seen with specially coated optics and signal processing techniques using TTFMS, the next section will discuss how absorptions as small as 3×10^{-4}% can be measured with 2f detection with off-the-shelf optics and equipment and techniques that are much simpler to implement than the high-frequency techniques. With narrowband AR-coated optics and optical isolation of the laser, it may be possible to achieve a sensitivity of $< 10^{-5}$. Recent work by Silver, Stanton and Bomse [53,54] does indeed indicate that harmonic detection and TTFMS can attain the same beam noise limit if the modulation frequency in harmonic detection is sufficiently high. Under certain conditions, harmonic detection may be the superior detection technique for diode laser absorption spectrometers.

4.3 Performance of the Absorption Spectrometer

4.3.1 AlGaAs Short-External-Cavity Lasers

Five Mitsubishi ML4095 AlGaAs lasers were tested. These lasers operated in the 760 nm region and lased in a single longitudinal mode over a small range of current before a mode hop occurred. Single-mode operation was considerably enhanced by the SXC in conjunction with mode control techniques.

Bias current tuning and temperature tuning rates of these lasers were -0.24 cm^{-1}/mA and -0.60 cm^{-1}/mA respectively. The bias current tuning allowed 80-120% coverage of a mode spacing at constant heat sink temperature when the SXC was used; only 15% of a mode spacing could be covered without the SXC before a mode hop occurred. The current-tuning rate of these lasers allowed optimum 2f detection of absorption lines at atmospheric pressure with only 0.8 mA peak-to-peak current modulation. This was only a small percentage of the useable range of the laser ($\approx$35 to 70 mA), so non-linearities in the LI curve did not contribute substantially to the 2f background signal. Such signals may limit sensitivity (Sect. 4.2.2(b)). Provided modulation noise is not enhanced at smaller modulation depths, the sensitivity achieved for atmospheric-pressure broadened should also be obtained at lower gas pressures and into the Doppler-broadened regime.

High-sensitivity detection of atmospheric-broadened lines of the $b^1\Sigma^+_g \leftarrow X^3\Sigma^-_g$ electronic transition of O_2 was obtained with SXC AlGaAs lasers in the absorption spectrometer. Modulation noise levels of $\approx 3\times10^{-6}$ were achieved at a 10 kHz modulation frequency and a 1.25 Hz equivalent noise bandwidth (ENBW). Minimal optics were used and the sample was the lab atmosphere. This noise level was $<$2x beam noise. Increasing the modulation frequency to 50 kHz reduced the beam noise by a factor of 3, but provided no improvement in the modulation noise. Similarly, reducing the detection bandwidth reduced the beam noise accordingly, but the modulation noise remained the same. However, 2f signals measured with the lock-in amplifier at quadrature were close

to beam noise at all detection frequencies and bandwidths. This suggests that the limiting noise was some wavelength-dependent effect such as optical feedback, laser temperature fluctuations, or etalon fringes caused by partially reflecting surfaces in the optical path.

The modulation noise and the beam noise did not vary significantly in each of the laser modes obtainable with the SXC. This is important if the full wavelength range of the instrument is to be used. In addition, the presence of the SXC did not affect the sensitivity of the spectrometer. Because these lasers operated in a single mode over a small range of injection current, modulation and beam noise could be easily measured in each mode with and without the SXC. Also, the response time constant and gain of the mode control feedback loop did not affect sensitivity, provided the stability of the external cavity was maintained.

Figure 4.2 is a plot of the 2f signal as a function of optical frequency for an isolated and weak O_2 absorption at atmospheric pressure using the absorption spectrometer. The figure shows a modulation noise of $\approx 5 \times 10^{-6}$ on a gently sloping 2f background, and two small absorption lines. The absorption signal indicated by the arrow is caused by a laser side mode passing through a strong absorption line. This effect may limit the performance that can be achieved with diode laser absorption spectrometers.

As was discussed in Chapter 2, the SMSR of an SXC laser is typically between 0.1-1% and depends strongly upon alignment and laser conditions. The effect of this

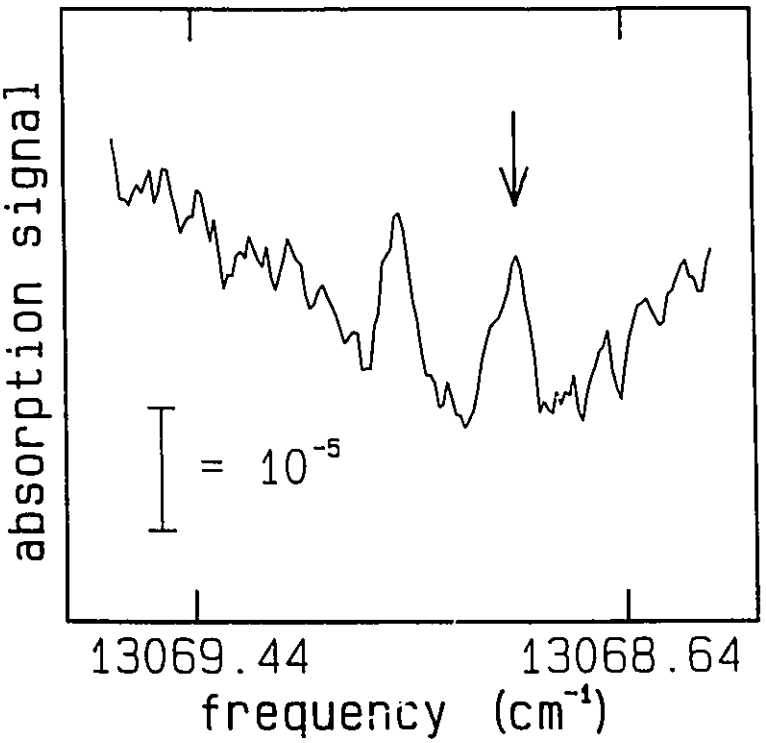

Figure 4.2

The signal indicated by the arrow is caused by a weak side mode passing through an ^{16}O-^{16}O absorption line; the other signal is caused by the main laser mode passing through an ^{18}O-^{16}O absorption line. This 2f scan was done with an SXC AlGaAs laser at a modulation frequency of 10 kHz and a detection bandwidth of 1 Hz.

finite SMSR was discovered and investigated with SXC AlGaAs lasers. The lasing region coincided with absorption lines of both ^{16}O-^{16}O and ^{16}O-^{18}O of the $b^1\Sigma^+_g \leftarrow X^3\Sigma_g$ transition. The ratio of the absorption coefficients of these two molecules is approximately the ratio of the isotopic abundances, which is about [^{16}O-^{16}O]:[^{16}O-^{18}O] = 500:1. However, this is approximately the SMSR of the laser. Thus, it is possible that when the main laser mode is tuned through a region of interest containing a ^{16}O-^{18}O line, a side mode may pass through a an ^{16}O-^{16}O line at a nearby wavelength (Fig. 4.3). This can cause a spurious absorption signal that can easily be confused with the "true" signal (see for example Fig. 4.2). If the positions of the absorption lines of each isotopic species and the mode spacing of the laser are known, then the spurious signals can usually be identified. However, if measurements are made for a molecular species for which the exact positions of the absorption lines of each istopic species are unknown, the spurious signals will be more difficult to identify. An attempt was made to filter out the laser side modes with a monochromator, but this resulted in increased noise and a non-linear 2f background, possibly caused by feedback from the monochromator. Fortunately, the SXC allowed the identification of these unwanted spectra. A 2f absorption spectrum was recorded, the SMSR was slightly altered (increased by 2x) by changing the mode control parameters, then a second spectrum was recorded. The side mode absorption changed relative to the dominant mode signal, as shown in Figure 4.4. It is important to be aware that the side-mode signals may be present when detecting weak absorption lines near stronger lines, and that care must be taken to avoid

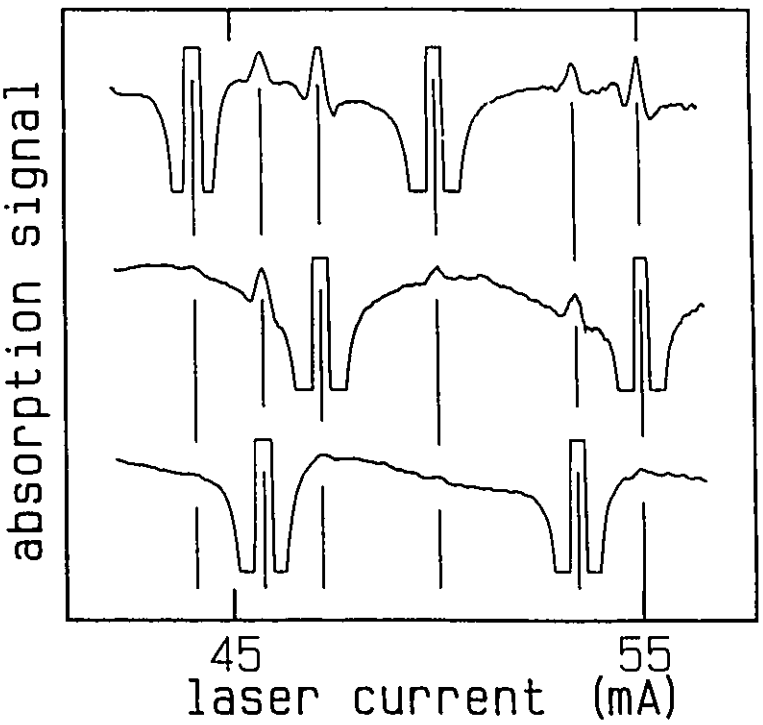

Figure 4.3

Three adjacent AlGaAs laser modes were selected with the SXC and a scan was made in each mode over the identical range of laser injection current. The main mode in one scan becomes a suppressed side mode in another scan. However, the side mode still has sufficient power to cause a signal at exactly the same laser current as it passes through the same strong absorption profile as it did when it was the main mode. The resulting contamination of the spectra is clear.

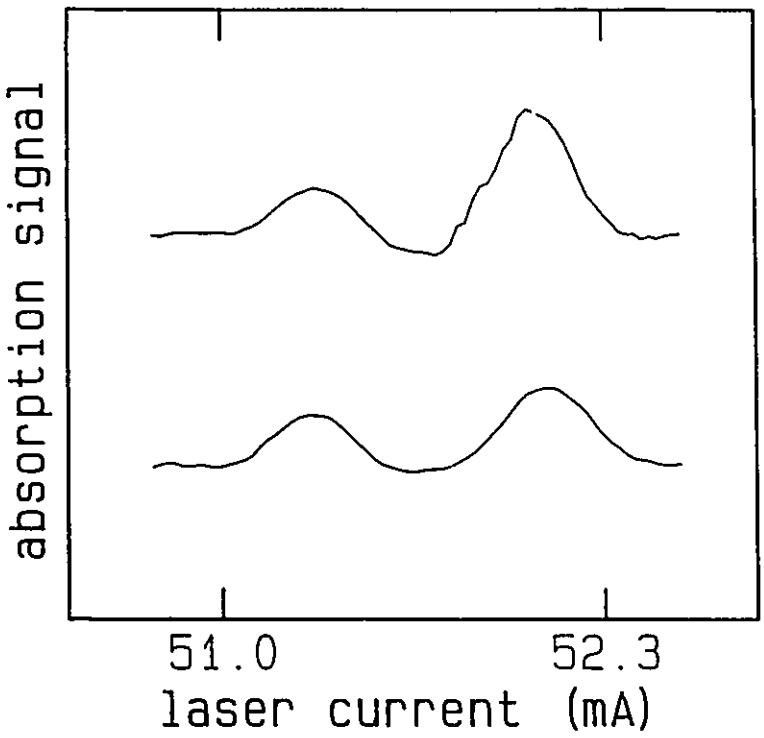

Figure 4.4

Scans through the same spectral region. For one scan, the SMSR was adjusted to alter the fraction of energy in the side modes and yet have a negligible effect on the energy in the main mode. This causes the absorption signal due to the side mode passing through a strong line to change relative to the absorption due to the main mode.

confusing the desired signals with the spurious ones. Side mode signals will occur with any laser with a finite SMSR, including DFB lasers, although SXC lasers offer a way to identify them by altering the SMSR. This is not possible with DFB lasers. It should also be noted that the SMSR is not static because of small drifts and fluctuation in the laser conditions or cavity alignment. The magnitude of the side mode signals may vary over time and give rise to a non-reproducible background that could be interpreted as a contribution to modulation noise.

4.3.2 InGaAsP Lasers

Multi-mode 1.3 μm InGaAsP lasers with gain-guided, IRW (inverted-rib-waveguide) and index-guided structures were forced to operate single mode with a short-external cavity. A SMSR of $\approx$0.5% was obtained on 4 to 12 modes. The tuning characteristics of these lasers is different from the AlGaAs devices. The bias current tuning rate for gain-guided lasers was -0.10 cm^{-1}/mA while IRW and index guided lasers tuned at -0.03 cm^{-1}/mA, which was considerably less that of the AlGaAs lasers; temperature tuning was -0.4 cm^{-1}/K. Only 20-50% of a 5 cm^{-1} mode spacing could be covered by current tuning, but complete single-mode spectral coverage in overlapping segements could be obtained over as much as 250 cm^{-1} with these lasers.

Absorption lines of H_2O at 100 Torr were used to determine the sensitivity of the system. Etalon fringes from the collimating lens and detector surfaces limited the

sensitivity of the system when 2f detection was used. Tilting of the optical surfaces reduced the fringes to an equivalent absorption of 10^{-4}. The modulation noise could be reduced to $<2x$ the beam noise at a detection frequency of 10 kHz and detection bandwidth of 1.25 Hz by adding ND filters between the laser and collimating lens and between the detector and focusing lens. A total attenuation of 10-15x was required. The beam noise was measured in each laser mode and was found to be $\approx 3x10^{-4}$. Figure 4.5 shows the beam noise in three different modes. The beam noise could be further reduced by detecting at higher frequencies or reducing the detection bandwidth, but the modulation noise limit remained the same. The results are consistent with the results obtained with AlGaAs lasers and suggest the modulation noise is caused by a wavelength-dependent effect such as fringes, feedback to the laser or side modes passing through strong absorption lines. Again, as with AlGaAs lasers, the presence of the external cavity did not substantially affect the modulation noise or the beam noise. The small current-tuning rate of the IRW and index-guided InGaAsP lasers did not permit sensitive detection of atmospheric pressure-broadened absorption lines. With tuning rates of -0.03 cm^{-1}/mA, the laser must be modulated over a considerable portion of its LI curve to detect optimally an atmospheric pressure-broadened line, which have a HWHM of ~ 0.1 cm^{-1}. The difficulties arise from the non-linearities in the LI curves that become increasingly important at larger current modulation amplitudes. Non-linearities cause offsets in the 2f background that increase the modulation noise and obscure the identification of weak absorption features [51]. Figure 4.6 shows the change in the 2f

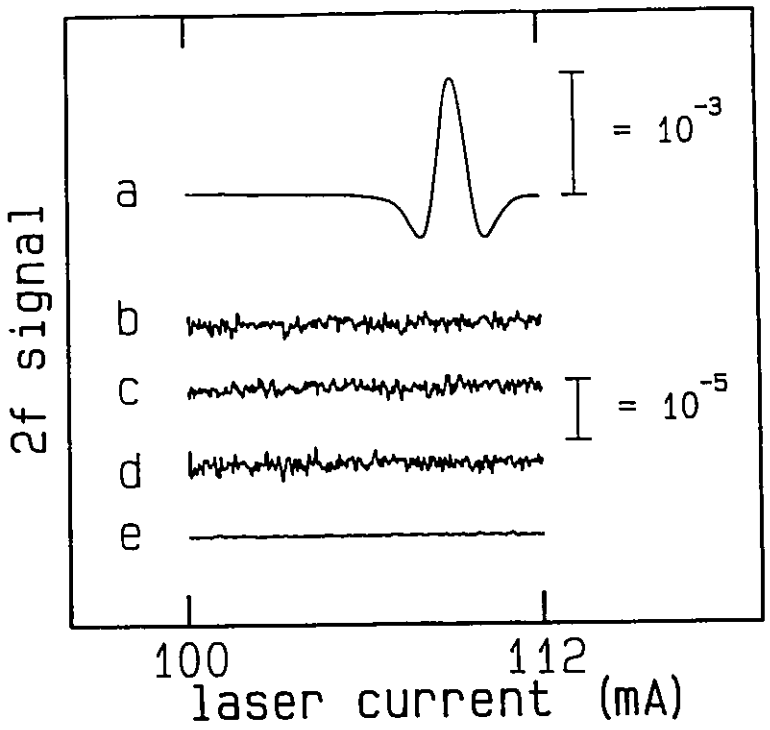

Figure 4.5

(a) Typical 2f absorption signal obtained with a 1.3 μm SXC InGaAsP laser. (b)-(d) are scans of beam noise (no laser modulation) in three different laser modes selected with the SXC, normalized to the power in each mode. (e) is detector noise. All scans are for a detection frequency of 20 kHz and a bandwidth of 1.25 Hz.

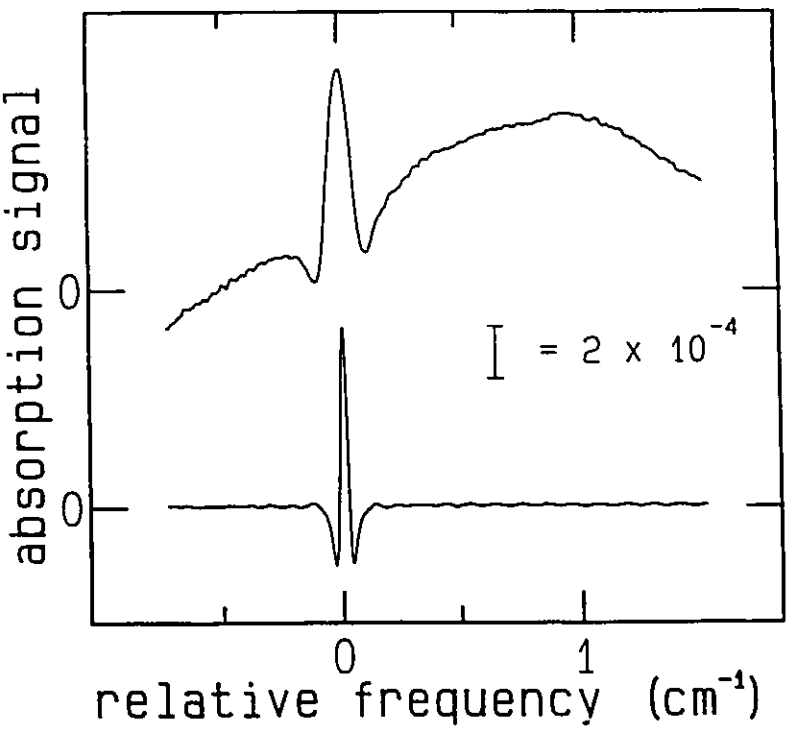

Figure 4.6

Profiles of H_2O absorption obtained using an SXC InGaAsP laser and 2f detection with optimum depth of modulation. The absorption in the upper trace is atmospheric-pressure broadened, while the lower trace shows the same absorption at a total gas pressure of 100 torr (20 torr H_2O). The 2f background obvious in the atmospheric-broadened scan is caused by the increased depth of current modulation that sweeps over a greater range of the slightly non-linear LI curve of the laser.

background signal when optimum 2f modulation was used for the same absorption line at 100 Torr and 760 torr.

Gain-guided InGaAsP lasers that were tested allowed current tuning of -0.1 cm^{-1}/mA, which is 3.3x better than IRW and index guided lasers. The reason for this difference is not clear, although it may be caused by the larger Ohmic heating from lower quality of epitaxial or metallization layers in the laser structure.

Evidently, then, not all NIR diode lasers can be used with 2f dtection for high-sensitivity measurements of broad absorption lines. The 2f background signal arising from non-linearities in the LI curve can be reduced by detecting at the fourth or sixth harmonics of the modulation frequency. Although this approach would be at the expense of absorption signal, the background should decrease considerably.

c) Distributed-Feedback (DFB) Lasers

Single mode operation is also obtainable from DFB lasers. As discussed in Chapter 1, these devices have been used by spectroscopists to study overtone transitions at 1.3 μm and 1.55 μm. However, DFB lasers are costly, difficult to construct and very difficult to obtain at wavelengths in between 1.3 μm and 1.55 μm. It is of interest, then, to compare the operation of DFB and SXC lasers under similar conditions in an absorption spectrometer.

Two 1.31 μm DFB lasers with similar operating characteristics were tested.

Single-mode operation was possible at an injection current of 25-65 mA (I_{th}=20 mA) for one laser, and 45-75 mA (I_{th}=40 mA) with the second laser. Instabilities in the laser modes occurred above these limits. The SMSR was <0.1%, and the mode spacings and current tuning and temperature tuning rates were 5 cm^{-1}, -0.04 cm^{-1}/mA and -0.5 cm^{-1}/mA respectively. These values are comparable to Fabry-Perot type InGaAsP lasers with IRW or index guiding. The limited current-tuning made difficult the highly-sensitive detection of atmospheric-broadened lines, so H_2O lines at 100 Torr were used for sensitivity measurements.

The sensitivity limit of the spectrometer with the DFB lasers used as a source is comparable to that found with SXC lasers. The beam noise was 10^{-6} at 2f=20 kHz and a 1.25 Hz detection bandwidth; it could be reduced by detecting at higher frequency or decreasing the detection banwidth. However, when 2f detection was attempted, etalon fringes limited the modulation noise to $5x10^{-5}$. The fringes were caused by reflections between the laser and the collimating lens and detector. The fringes were much more pronounced than with the InGaAsP SXC lasers even though both types of lasers had had similar emission wavelength and identical optical arrangements. It is possible that the larger fringes were caused by the greater susceptibility of DFB lasers to optical feedback.

The sensitivities achieved with these DFB lasers compare favourable with the results of Sasada [55], who attained sensitivities of 10^{-5} with a 1 ms time constant. The DFB lasers used here did not have a noticeably better sensitivity compared with the

SXC lasers and may be more susceptible to optical feedback. Neutral density filters were required to remove fringes and feedback to the lasers, reducing the available laser power. The DFB lasers were easier to use in practise, since different laser modes did not have to be selected by changing the external cavity length. Also, there is little danger of a mode hop with DFB lasers. However, the superior tuning range and flexibility of SXC lasers justify their use in many applications in trace-gas detection and spectroscopy.

Fiugre 4.7 is composed of plots of the 2f signal as a function of optical frequency for detection with an SXC AlGaAs laser (a), an SXC InGaAsP laser (b), and a DFB InGaAsP laser (c). The plots have been adjusted such that the ordinate scale is the same.

4.4 Summary

The characteristics of a tunable diode laser absorption spectrometer with InGaAsP and AlGaAs short-external-cavity diode lasers and InGaAsP distributed feedback diode lasers were investigated and compared. Second harmonic detection at audio frequencies was used to obtain noise levels equivalent to line-centre absorptions of 3×10^{-6} with all lasers tested. The noise levels did not appear to be affected by the presence of the external cavity or by the operation of the electrical feedback loop that maintains single-mode operation of the lasers. The limiting noise source was found to be modulation

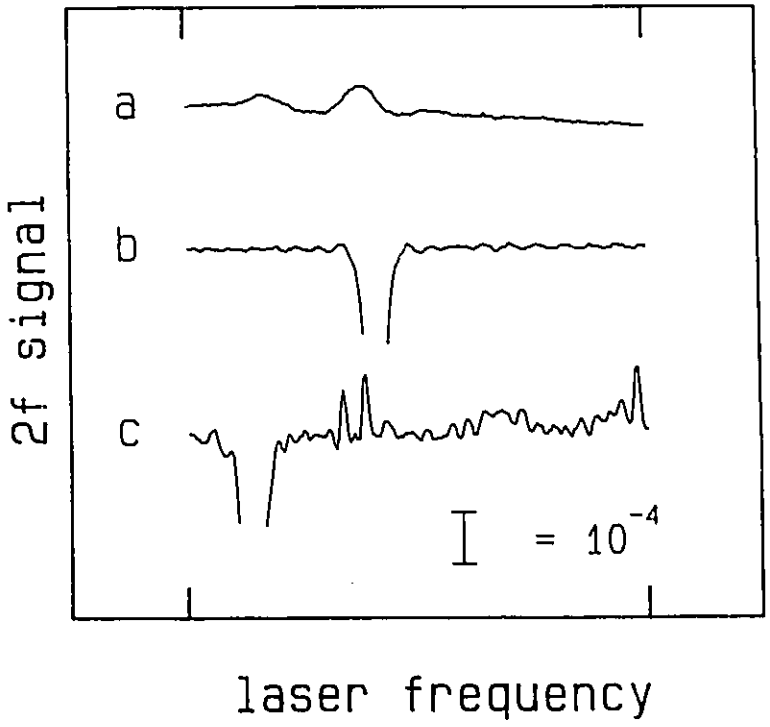

Figure 4.7

Plot of 2f signals as a function of optical frequency for operation of the spectrometer with (a) an SXC AlGaAs, (b) an SXC InGaAsP, and (c) a DFB laser.

noise caused by optical feedback to the laser diode and etalon fringes from reflection off surfaces in the optical path. Contamination of the measured absorption spectra by side modes passing through strong absorption lines while the main laser mode passed through a weak absorption line was shown to be a limitation of the spectrometer when the ratio of the absorption coefficients is of the order of the SMSR. This effect could be investigated with the SXC lasers. Some lasers had small frequency-tuning rates when the current was varied and had slightly non-linear LI curves that resulted in large 2f background offsets when detecting atmospheric pressure-broadened lines. These offsets made sensitive detection ($< 10^{-4}$) of such lines difficult. Finally, a comparison was made of the operation of the spectrometer with SXC and DFB lasers. Both lasers offered similar sensitivity, but the DFB lasers may be more susceptible to optical feedback. Although the DFB lasers are easier to use, the SXC approach is potentially less expensive and offers greater flexibility in selecting diode lasers that operate at wavelengths other than what is usually available in the tight tolerances around ~ 0.8, 1.3 and 1.55 μm.

CHAPTER 5 -

SPECTROSCOPIC INVESTIGATIONS WITH SXC DIODE LASERS

5.1 Introduction

The diode laser absorption spectrometer described in Chapter 4 has been used in several pure and applied spectroscopic investigations. Two such applications are discussed in this chapter. First, the accuracy with which the relative isotopic abundances of water vapour (HDO/H_2O) and carbon dioxide ($^{13}CO_2/^{12}CO_2$) can be determined has been assessed. The determination of these relative abundances is important in such diverse fields as medicine, industrial pollution monitoring, and petroleum exploration. The results presented here demonstrate the feasibility of using these lasers in performing such measurements using a potentially compact and reliable near-IR laser source. Second, a more fundamental investigation is performed of the $W_{1,-1}(0)$ multipole absorption transition of solid para-hydrogen [56]. The measurement of the $W_{1,0}(0)$ transition at high sensitivity and resolution yields improved parameters for the Hamiltonian that

describes this unique physical system [57].

5.2. *Relative Abundances of Isotopic Species of Water Vapour and Carbon Dioxide*

5.2.1 *Significance of the Measurements*

The main purpose of the investigation of the ratio of HDO/H_2O abundance is to demonstrate the feasibility of monitoring heavy-water vapour emission from nuclear generating plants. A rise in this ratio above the ambient natural value of ≈ 150 parts-per-million (ppm) near a reactor could indicate the presence of unwanted leakage in some part of the generating plant. Diode laser spectrometers could provide the sensitivity and selectivity necessary to simultaneously determine the concentration of each of these constituents. It is also possible with these lasers to monitor in real time the variation in this abundance ratio: this is crucial if prompt corrective action must be taken to reduce unwanted heavy water emission. The tunability of SXC lasers provides the versatility and sensitivity to measure this abundance ratio in the lab; the techniques and apparatus presented here could be the basis of a field monitor for trace-gas detection.

The measurement of the relative abundance of $^{13}CO_2$ and $^{12}CO_2$ has industrial, medical, and environmental significance. The relative abundance serves as a probe of the conditions in which the reaction of ^{12}C and ^{13}C with oxygen takes place. The rates

of reaction of ^{13}C and ^{12}C are slightly different because of the kinetic isotope effect [58], and the temperature and pressure of the reaction can determine the ratio of the abundance of these isotopes in the reaction products.[2] This effect can be used to probe conditions in several disparate circumstances. For instance, ^{13}C can be used as a tracer in the human body to monitor metabolism and detect diseases such as diabetes and liver dysfunction through measurement of the $^{13}CO_2/^{12}CO_2$ ratio in exhaled breath [59]. The advantage of ^{13}C is that it is not radioactive, which is a major disadvantage of using ^{14}C as a tracer in the human body. In addition, the relative abundance of carbon isotopes can be used to monitor past environmental conditions and climatic variations [60] and to trace the source of petroleum deposits [61]. Several groups using Pb-salt diode lasers have initiated efforts to measure the $^{13}CO_2/^{12}CO_2$ isotopic ratios of carbon dioxide and carbon monoxide [61,62,63,64], but near-IR lasers give the possibility of constructing a more compact, reliable, and economical monitor for such purposes. The feasibility of using near-IR SXC lasers in this type of monitoring was considered. Diode laser spectroscopy has advantages over traditional mass spectroscopic techniques because less sample preparation and no sample purification is required.

---

2 Of course, the same effect occurs for other isotopic combinations of carbon dioxide, but $^{13}CO_2$ has the highest natural abundance ($^{13}CO_2/^{12}CO_2 \approx 1{:}90$) and is therefore easiest to detect.

5.2.2 *Techniques and Requirements for Monitoring Abundance Ratios*

There are several methods to determine the abundance ratios. A most convenient technique would involve scanning the laser frequency over two closely spaced (less than a laser mode spacing) absorption lines, one from each isotopic species. Harmonic detection could be employed to enhance sensitivity. The concentration of the molecule is related to the strength and shape of the line profile, as will be described below. Subsequent signal processing of the measured absorption lines can easily yield the concentrations. The advantage of this technique is that a single laser in a single longitudinal mode can be used to record both molecules. A scan of both lines using harmonic detection requires only a few seconds, allowing real-time detection of changes in concentration.

To implement this technique, a requirement is that two absorption lines, one from each isotopic species, lie within ~ 5 cm^{-1} of each other but are still far enough apart to be resolved (~ 0.1 cm^{-1}). A further requirement is that each line that is detected be of comparable strength so that problems of dynamic range are not encountered in the detection electronics. The strength of the detected absorption line is proportional to the intrinsic strength of the transition (the dipole transition moment) and the number of absorbers in the optical path. Since there are far fewer molecules of $^{13}CO_2$ or HDO than $^{12}CO_2$ or H_2O, for example, the two adjacent absorption lines must have very different intrinsic absorption strengths to satisfy the above criteria. Finally, each absorption line

must be sufficiently strong to be detected by the SXC laser absorption spectrometer with an adequate SNR; this allows more accurate determination of relative isotopic abundances for a particular requirement. The effect of SNR on the accuracy is discussed below.

A compilation of spectroscopic information on absorption transitions of atmospheric molecules, including carbon dioxide and water, is given in the HITRAN database produced by the U.S. Air Force [65]. Further spectral data on HDO was obtained from R. Toth [66]. An examination of this data indicates the strongest lines of water and carbon dioxide occur at frequencies at which InGaAsP diode lasers are available (1.3-1.6 μm). Weaker bands can be observed with AlGaAs lasers, but these bands were not used here. To determine which satisfy the frequency proximity requirements of the lines, several bands were examined. The optimum region for simultaneous detection of HDO and H_2O was determined to be around 6620 cm^{-1} (1.51 μm), where there are strong HDO lines, many weak H_2O lines, and very few molecules such as CO_2 that may contaminate the spectra. Many adjacent pairs of HDO and H_2O lines lie in this region. For simultaneous detection of $^{13}CO_2$ and $^{12}CO_2$ with a single laser, the optimum frequency is around 6350 cm^{-1} (1.57 μm), although the absorption lines here are somewhat weak. Stronger lines are available, if necessary. The strongest $^{13}CO_2$ lines in the near-IR are in the $(00^03)\leftarrow(00^00)$ band at 6780 cm^{-1} (1.475 μm). $^{12}CO_2$ lines of similar strength are found in the $(30^01)\leftarrow(00^00)$ band at 6490 cm^{-1} (1.541 μm). To determine the relative isotopic abundance using these strong bands would require two separate lasers. This is an inconvenience, not a serious problem.

5.2.3 *Determination of Molecular Concentration from the Measured Spectra*

The amount of absorption of laser light of frequency ν caused by a single absorption transition from the lower state n to upper state m is given by [67]

$$I(\nu)=I_0(1-\exp(-\alpha(\nu)L)) \tag{5.1}$$

where I_0 is the intensity of light incident upon the gas sample, L is the length of the sample, and $\alpha(\nu)$ is the absorption coefficient. This is the absorption that is detected experimentally, and it is theoretically given by

$$\alpha(\nu)=\frac{c^2}{8\pi\nu^2 g_n} N_n A_{mn} (1-\exp(-h\nu_{mn}/kT)) \Phi(\nu) \tag{5.2}$$

where ν_{mn} is the resonant frequency of the transition, g_m and g_n are the statistical weights of the upper and lower states, A_{mn} is the Einstein coefficient for the transition, N_n is the population density of the lower state, k is Boltzmann's constant, h is Planck's constant, and T is absolute temperature. The function $\Phi(\nu)$ is the lineshape function which depends on the mechanism of line broadening of the absorbing molecules. Proper normalization requires that

$$\int_0^\infty \Phi(\nu)d\nu = 1 \tag{5.3}$$

regardless of the shape of $\Phi(\nu)$. If there is a Boltzmann distribution among the energy

levels of the absorber, then

$$N_n = \frac{g_n N_a \exp(-E_n/kT)}{Z(T)} \tag{5.4}$$

where N_a is the total number of absorbing molecules, E_n is the energy of the lower level above the ground state, and Z(T) is the partition function. Also, at near-IR frequencies and terrestrial temperatures, $h\nu \gg kT$, so the absorption coefficient reduces to

$$\alpha(\nu)=\frac{c^2 N_a}{8\pi\nu^2 Z(T)} \exp(-E_n/kT) A_{mn} \phi(\nu) \tag{5.5}$$

The total strength of the line is

$$\begin{aligned} S &= \int_0^\infty \alpha(\nu)\, d\nu \\ &= S_a(T) N_a \end{aligned} \tag{5.6}$$

where $S_0(T)$ is a measure of the intrinsic strength of the transition and N_a is the number density of absorbers in the path.

Using the definition of line strength in (5.6), the normalized phenomenological absorption coefficient is, for a Doppler-broadened transition [68]

$$\alpha_D(\nu)=\sqrt{\frac{\ln 2}{\pi}} \frac{S}{\gamma_D} \exp(-\ln 2 (\frac{\nu-\nu_{mn}}{\gamma_D})^2) \tag{5.7}$$

where the Doppler half-width at half maximum (HWHM) is

$$\gamma_D = \sqrt{\frac{2\ln 2kT}{mc^2}}\ \nu \tag{5.8}$$

At higher gas pressure, pressure broadening of the transition dominates Doppler broadening. For a pressure-broadened transition, which generally have a Lorenztian frequency dependence,

$$\alpha_L(\nu) = \frac{S}{\pi}\frac{\gamma_L}{(\nu-\nu_{mn})^2+\gamma_L^2} \tag{5.9}$$

for a pressure-broadened HWHM of γ_L, which is given by

$$\begin{aligned}\gamma_L &= \gamma_L^o\ P_b \\ &= \gamma_L^o\ \frac{N_b}{kT}\end{aligned} \tag{5.10}$$

for a pressure P_b of broadening gas with number density N_b. The quantity γ_L^0 is the line broadening constant of a given spectral line by a particular type of absorber. It is usually given in units of (frequency/unit pressure of broadening gas), hence the above definition. Pressure broadening is dominant when $\gamma_L \gg \gamma_D$, while Doppler broadening dominates in the opposite case. When $\gamma_L \approx \gamma_D$, the absorption line is a convolution of the Gaussian and Lorenztian profiles: such a convolution is called a Voigt profile, and is given

explicitly by

$$\alpha_\nu(\nu) = \sqrt{\frac{\ln 2}{\pi}}\,\frac{S}{\pi\gamma_D}\int_{-\infty}^{\infty}\exp(-\ln 2(\frac{y}{\gamma_D})^2)\,\frac{\gamma_L}{(\nu-\nu_{mn}-y)^2+\gamma_L^2}\,dy$$
$$= \sqrt{\frac{\ln 2}{\pi}}\,\frac{S}{\gamma_D}\,H(u,a) \qquad (5.11)$$

where

$$u = \frac{\sqrt{\ln 2}}{\gamma_D}(\nu-\nu_{mn}) \qquad (5.12)$$

and

$$a = \frac{\gamma_L}{\gamma_D}\sqrt{\ln 2} \qquad (5.13)$$

and H(u,a) is a tabulated function [69].

In general, according to (5.6), it is necessary to integrate the measured absorption line to recover the number density N_a of absorbers in the path. In some cases, however, this is not necessary: N_a becomes proportional to the line centre absorption. This simplifies the analysis of the measured data. For a Doppler-broadened transition, for example, the line-centre absorption is

$$\alpha_D(\nu_{mn}) = \sqrt{\frac{ln2}{\pi}}\,\frac{S_o N_a}{\gamma_D} \tag{5.14}$$

Clearly, the line centre absorption is directly proportional to the number of absorbing molecules. In the pressure-broadened regime at line centre

$$\alpha_L(\nu_{mn}) = \frac{S_o N_a kT}{\pi \gamma_l^o N_b} \tag{5.15}$$

If the absorbing and broadening gas are the same (self broadening in a pure gas, for example) then the line-centre absorption is *independent* of the concentration of absorbing molecules. In this case, the entire line must be integrated over frequency to recover the absorbing gas concentration [64]. However, if the absorbing gas is present in only trace amounts in a buffer gas of fixed partial pressure P_b, and the contribution of self-broadening is small compared to buffer-gas broadening, then (5.15) shows that the line-centre absorption is indeed nearly proportional to the trace-gas pressure. The same relation is true for a Voigt profile at line centre. In the cases of water or carbon dicxide in air, then these conditions are met because these gases have much smaller partial pressures than the main constituents of air. Therefore, the determination of the accuracy to which a trace-gas concentration can be monitored reduces to the experimental problem of determining the accuracy with which the line centre absorption can be measured. The arguments made here for monitoring the concentration of a trace gas also apply when

second-harmonic detection is used to enhance the sensitivity.

Another important consideration in monitoring the relative concentration of two molecules is the temperature dependence of the lower state population, which is demonstrated by (5.5). If the two molecular transitions considered have different lower state energies, then the measured relative concentration of molecules 1 and 2 will be temperature dependent:

$$\frac{\alpha_1}{\alpha_2} = K \exp(-(E_{m1} + E_{m2})/kT)$$

where K is a quantity that varies weakly with temperature. Stabilization or precise measurement of the temperature of the sample gas may therefore be necessary in some circumstances.

5.2.4 Results

The spectrometer system described in Chapter 4 was used to make the concentration measurements. To determine the accuracy with which changes in concentration could be monitored, several scans were made over the molecular absorption lines and the variation in magnitude of these lines was analyzed. The gas samples were held at a constant total pressure in a 35 cm glass cell or a White cell with an absorption

length of 12 m.

Several HDO and H_2O lines were found in a 3 cm^{-1} (0.5 nm) region at 6595 cm^{-1} (1.51 μm) with a single SXC laser. Figure 5.1 shows the 2f spectra and identifies the lines. The gas was held in a 35 cm cell with saturated H_2O in 180 torr of air. The differences in energy of the lower states of these transitions were such that a change in temperature of greater than 5 °C was necessary to change the relative concentration by 1%; such a change in temperature did not occur during the following measurements. The water in this sample was enriched so that the concentration ratio of HDO/H_2O was 1:25. Thirty scans were made of this region. Data in Table 5.1 shows the magnitudes of each absorption line in Fig. 5.1 and the mean magnitude and standard deviation of each line.[3] Table 5.2 contains the ratios of several pairs of HDO and H_2O lines and the mean and standard deviation (σ) of these ratios. The standard deviation of these ratios divided by the mean is the crucial quantity. Any real change in the concentration ratio of the molecules must exceed 2σ to be detected with 95% certainty. Hence, relative concentration difference of 9% can be detected in this circumstance. Further measurements over longer paths in a White cell with natural HDO abundance gave very similar results.

The results in Tables 5.1 and 5.2 suggest that large ratios of line centre absorptions result in larger uncertainties. In fact, if σ is plotted against ratio, the value

---

[3] Line 'F' in Fig. 5.1 is likely caused by a side mode passing through a strong H_2O line.

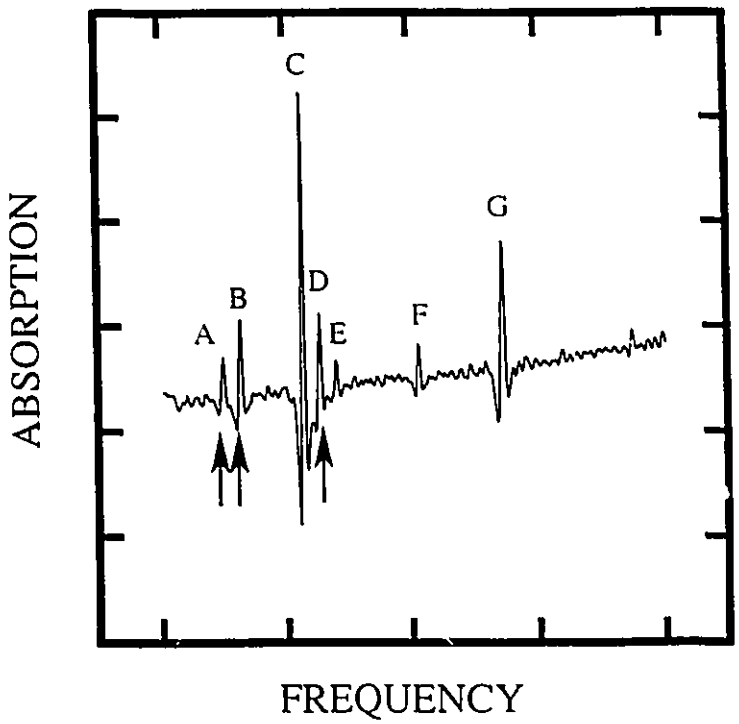

Figure 5.1

A spectrum of H_2O and HDO measured using second harmonic detection. The HDO lines are indicated with an arrow; all others are from H_2O. The line marked 'F' is caused by a laser side mode passing through a strong H_2O line.

of σ saturates at 2% when the ratio approaches unity. Thus it is estimated that for two lines of nearly equal absorption strength, the concentration could be monitored to 4% with 95% certainty.

This limit of 4% uncertainty is not fundamental. Previous work [24,64] indicate that concentrations can be monitored to within $\pm$0.2-0.6%. The higher limit presented here is a result of the poor SNR caused by interference fringes. Reduced fringes or increased signal could lead to improved results. Increasing the path length through the White cell will in principle increase the signal. However, with the present cell, increasing the path beyond 12 m results in no increase in SNR because of increased interference fringes in the cell at longer pathlengths. Other contributions to the uncertainty might include laser frequency fluctuations caused by drift in the laser current and temperature driver electronics and frequency-pulling effects caused by small fluctuations in the length of the external cavity.

To monitor the relative concentration of $^{13}CO_2$ and $^{12}CO_2$, two separate SXC lasers were used. One laser measured the P(18) line of the $(00^03)\leftarrow(00^00)$ band of $^{13}CO_2$ at 6763.4474 cm^{-1}. The second laser measured the P(18) line of the $(30^01)\leftarrow(00^00)$ band of $^{12}CO_2$ at 6488.6213 cm^{-1}. These transitions have very similar lower-state energies. The gas sample was 10 torr of CO_2 of natural isotopic abundance in 240 torr of buffer gas (air). This ratio approximates composition of exhaled human breath. The SNR for these lines is vastly improved over the measurements for water (Fig. 5.2). The analysis was similar to that for water. Several scans were made of each absorption line, and the

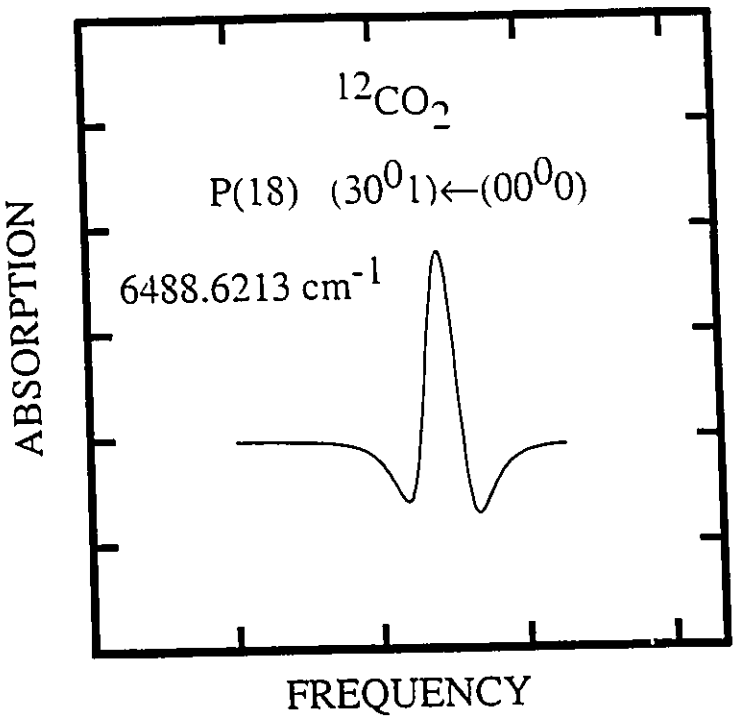

Figure 5.2(a)

A spectrum of the P(18) line of the $(30^01)\leftarrow(00^00)$ band of $^{12}CO_2$ measured with second harmonic detection. The sample path length was 12m in a multipass cell with 10 torr of CO_2 and 240 torr air.

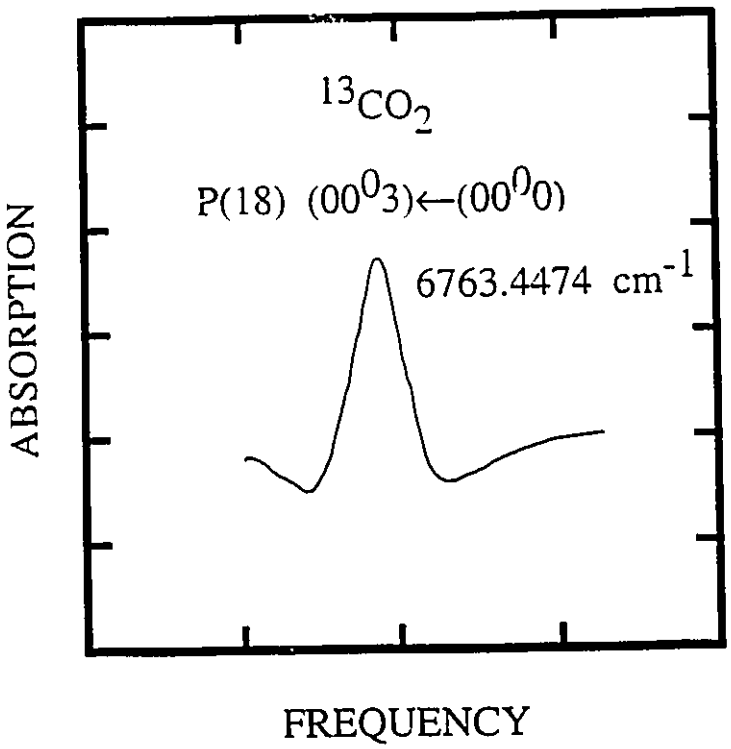

Figure 5.2(b)

A second harmonic spectrum of the P(18) line of the $(00^03)\leftarrow(00^00)$ band of $^{13}CO_2$ with the same path length and partial pressures as in Fig. 5.2(a).

TABLE 5.1

Magnitude of absorption lines for H_2O and HDO.

Run	ABSORPTION LINES					
	B (HDO)	C (H_2O)	D (HDO)	E (H_2O)	F see text	G (H_2O)
1	157.3	714.8	157.8	38.7	19.9	72.1
2	154.5	715.1	162.1	45.7	25.2	64.4
3	148.7	693.1	151.8	48.5	19.7	68.8
4	160.7	734.4	154.5	50.8	-	70.2
5	145.0	698.5	155.5	46.9	-	71.7
6	150.4	734.4	152.6	47.3	18.0	71.8
7	144.4	775.1	148.4	57.5	-	66.5
8	144.8	708.3	146.0	59.7	-	60.2
9	145.8	737.8	144.1	49.0	-	61.8
10	142.1	722.4	150.0	47.6	20.4	73.0
11	142.2	702.4	147.1	47.6	16.8	65.8
12	134.5	696.5	145.7	45.0	20.3	68.5
13	154.1	747.8	151.1	44.2	26.2	75.4
14	147.6	735.1	151.5	47.9	24.5	75.3
15	143.2	727.8	149.9	47.3	22.6	67.7
16	158.2	754.9	145.1	50.0	29.7	77.6
17	153.1	743.4	145.8	49.3	21.6	69.9
18	149.0	730.5	147.5	59.6	25.9	72.7
19	154.3	782.9	150.3	62.2	23.9	72.6
20	158.3	744.6	150.0	53.4	26.6	77.5
21	150.9	725.8	143.2	55.5	28.5	72.3
22	164.6	769.0	147.4	44.9	32.4	79.1
23	153.1	750.5	153.9	68.4	21.8	71.5
24	158.0	743.7	148.0	46.1	28.6	79.1
25	152.4	728.8	143.9	51.1	26.9	73.5
26	162.9	752.4	151.9	54.4	21.9	74.2
27	154.2	741.5	141.0	50.7	26.9	76.8
28	150.7	723.6	141.8	59.8	15.6	72.9
29	170.8	755.4	141.8	56.6	19.0	71.7
30	182.8	747.6	149.5	58.7	15.8	68.2
mean	153.0	734.6	149.0	51.5	23.1	71.4
σ	9.3	22.1	4.8	6.4	4.4	4.6
σ(%)	6.1	3.0	3.2	12.5	19.1	6.5

TABLE 5.2

Ratios of absorption line magnitudes for H_2O and HDO.

ABSORPTION LINES RATIOS

Run	C/A	C/B	10*G/D	C/D	C/E	C/F	C/G
1	8.7	4.5	4.6	4.5	18.5	35.9	9.9
2	9.7	4.6	4.0	4.4	15.6	28.4	11.1
3	11.7	4.7	4.5	4.6	14.3	35.2	10.1
4	13.9	4.6	4.5	4.8	14.5	-	10.5
5	12.3	4.6	4.6	4.5	14.9	-	9.7
6	12.4	4.9	4.7	4.8	15.5	40.8	10.2
7	14.4	5.4	4.5	5.2	13.5	-	11.7
8	13.6	4.9	4.1	4.9	11.9	-	11.8
9	14.6	5.1	4.3	5.1	15.1	-	11.9
10	11.8	5.1	4.9	4.8	15.2	35.4	9.9
11	11.7	4.9	4.5	4.8	14.8	41.8	10.7
12	13.1	5.2	4.7	4.8	15.5	34.3	10.2
13	11.2	4.9	5.0	4.9	16.9	28.5	9.9
14	10.7	5.0	5.0	4.9	15.3	30.0	9.8
15	10.9	5.1	4.5	4.9	15.4	32.2	10.8
16	10.7	4.6	5.4	5.2	15.1	25.4	9.7
17	10.6	4.9	4.8	5.1	15.1	34.4	10.6
18	10.8	4.9	4.9	5.0	12.2	28.2	10.0
19	11.2	5.1	4.8	5.2	12.6	32.8	10.8
20	11.2	4.7	5.2	5.0	13.9	28.0	9.6
21	11.6	4.6	5.0	5.1	13.1	25.5	10.0
22	11.4	4.7	5.4	5.2	17.1	23.7	9.7
23	10.5	4.9	4.6	4.9	11.1	34.4	10.5
24	12.2	4.7	5.3	5.0	16.1	26.0	9.4
25	10.7	4.8	5.1	5.1	14.3	27.1	9.9
26	11.1	4.6	4.9	5.0	13.8	34.4	10.1
27	12.9	4.8	5.4	5.3	14.6	27.6	9.7
28	10.3	4.8	5.1	5.1	12.1	46.4	9.9
29	12.7	4.4	5.1	5.3	13.3	39.8	10.5
30	12.0	4.1	4.6	5.0	12.7	47.3	11.0
mean	11.7	4.820	4.8	4.9	14.5	32.9	10.3
σ	1.3	0.2	0.4	0.2	1.6	6.3	0.6
σ(%)	11.4	5.0	7.5	4.7	11.3	19.3	6.3

mean and standard deviation of the magnitude of the lines were calculated. The results indicate that each line could be monitored with an uncertainty of $\pm 0.5\%$ (2σ result). The relative concentration can therefore be monitored to $\pm 1\%$, which is 4x better than the water measurements.

These simple measurements demonstrate that the relative concentration of two molecules, in this case two isotopic species of the same molecule, can be monitored to $\pm 1\%$ with very little specialized data processing or measurement techniques. Opportunity remains to identify the sources that limit this accuracy and to improve on this limit. Near-IR lasers offer the chance of developing field instruments for monitoring the concentration of molecules of medical, environmental, and industrial significance.

5.3 Measurement of the $W_{1\leftarrow 0}(0)$ Transition of Solid Hydrogen

5.3.1 Spectroscopy of Solid Hydrogen

The narrow linewidth of lasers is very valuable for measurements of the spectra of atoms and molecules in the gas phase. Such spectra are typically characterized by discrete and narrow spectral line profiles. Atoms and molecules in the condensed phase usually display much broader spectral features caused by strong interatomic or intermolecular interactions. Consequently, spectroscopic measurements of solids can

often be accomplished with broadband light sources. Solid hydrogen is an exception to this behaviour. The physical nature of this solid is such that rotational and vibrational transitions have very narrow linewidths that approach those of gas-phase spectra. High-resolution spectroscopic techniques developed for gas-phase spectroscopy can therefore be employed to study solid hydrogen. This section describes the use of an SXC InGaAsP laser to observe the $W_{1\leftarrow0}(0)$ transition of solid hydrogen at 6441cm^{-1} (1.55 μm). The spectral purity and low noise of these lasers when used with harmonic detection allowed the observation and measurements of the fine structure of this transition that has not been previously observed.

Only an overview of the spectroscopy of solid hydrogen is given here. A complete quantitative explanation of the spectroscopy of solid hydrogen requires a detailed consideration of the simultaneous interaction of a each single hydrogen molecule with the molecules of the entire crystal. Such a description has been given by van Kranendonk [70,71,72].

Solid hydrogen forms a hexagonal closed-packed (hcp) crystalline structure with an H_2 molecule at each lattice site. The crystal is bound by very weak and slightly anisotropic intermolecular forces that allow each molecule to rotate and vibrate freely about its equilibrium position in the lattice. An isolated H_2 molecule has no permanent dipole moment and therefore no electric-dipole-allowed rotational or vibrational transitions. In the solid state, however, the multipole moment of each H_2 molecule induces dipole moments in the surrounding molecules. Absorption of light is caused by

these induced dipole moments through many-body interactions. These multipole-induced dipole transitions follow the selection rules of the multipole transitions, and the intensity of the dipole transitions is governed by the magnitude of the many-body interactions that induce the dipole moments. Correlation of the solid spectra with gas phase spectra indicate that the vibrational and rotational quantum numbers υ and J are still good quantum numbers, and the transition frequencies of the gas-phase and solid-state spectra are within 15 cm^{-1}.

Narrow transitions are observed only in nearly pure para-hydrogen (J=0 for each molecule). Linewidths (HWHM) of as low as 50 MHz for the $W_0(0)$ transition have been observed [73,74]. The presence of ortho-hydrogen (J=1) broadens the linewidth and gives rise to impurity splitting of each transition. The transitions also exhibit fine structure caused by interaction with the crystal field (for the U and W branches), or by the dynamics of the rotational excitation (for the S branch). The observed narrowness of the linewidths of the U and W transitions are as yet not fully explained.

Several IR transitions of solid hydrogen have already been observed. The Q and S branches[4] were observed in the first spectroscopic study of solid hydrogen

---

[4] The notation of the solid hydrogen transitions follows that of electric-dipole induced transitions in gases, which denote a $\Delta J=-1$ transition as P, a $\Delta J=0$ transition as Q and a $\Delta J=1$ transition as R. S therefore refers to a transition with $\Delta J=2$, U to $\Delta J=4$ and W to $\Delta J=6$, etc. The number in brackets is the J value for the ground state and the subscript describes the change in vibrational quantum number.

[75]. Since then, the much weaker $U_{1\leftarrow0}(0)$ and $U_0(0)$ transitions have been observed [76,77]. Most recently, the $W_{1\leftarrow0}(0)$ and $W_0(0)$ transitions were observed with a Fourier-transform spectrometer at 6441.81cm^{-1} and 2410.538 cm^{-1} respectively; the latter was also observed at high resolution with a difference frequency (DF) laser spectrometer operating in the 2400 cm^{-1} region [73,74], and the crystal field splitting was measured [74]. The W transitions are 5 orders of magnitude smaller than the S branch. A 6440 cm^{-1} (1.55 μm) SXC laser was used to measure the crystal field splitting and impurity splitting of the $W_{1\leftarrow0}(0)$ transition. The measurements are presented here: further details on the assignment of the spectra appear in references [56,57].

5.3.2 Experimental

With some exceptions, the observation of the $W_{1\leftarrow0}(0)$ transition is accomplished with the same absorption spectrometer and detection techniques used in Chapter 4 and Section 5.2. The following experiments were carried out during a collaboration with T. Oka, K.E. Kerr, T.J. Byers, and T. Momose of the University of Chicago, Departments of Chemistry and Astronomy and Astrophysics.

The sample in this experiment is a crystal of solid para-hydrogen. The crystal was grown in a cylindrical copper cell 11.5 cm in length and 2 cm in diameter. The cell was fixed to the bottom of the vessel of an Infrared Laboratories HD-3 liquid

helium dewar outfitted with wedged calcium fluoride windows. The cell was sealed with planar sapphire windows and indium gaskets. The crystals were grown by continuously flowing ultra-pure hydrogen gas over a catalyst held at 20 K and into the cell, which was kept at a temeprature of 10 K. Once growth was complete, the crystal was cooled to 4.2 K; the catalyst converts the hydrogen in the crystal to 99.8% para-hydrogen. The dewar then had to be re-filled with liquid He every 4-5 hours. The concentration of ortho-hydrogen was measured by integrating the absorption profile of the $Q_{1\leftarrow 0}(1)$ ortho transition measured at 4146.4 cm^{-1} with a Fourier-transform spectrometer. The crystals were nominally optically transparent at optical and near-IR frequencies. Several crsytals were grown and measured, and the optical quality of each varied only slightly.

Single-mode near-IR radiation from the SXC InGaAsP laser was collimated and passed obliquely (to avoid unwanted etalon fringes from the cell windows) through the dewar and sample cell and focused onto an InGaAs detector. The SMSR of the SXC laser was nominally ~0.5%. The laser mode was stable during the experiments: mode hops rarely occured during laser frequency tuning. For this reason, the mode control techniques were not implemented. About 0.2 mW of radiation was incident on the detector. The crystal and dewar transmitted ~35% of the laser radiation when the laser frequency was tuned away from the $W_{1\leftarrow 0}(0)$ transition. Losses were caused by reflection at the windows of the dewar and sample cell and by scattering from defects in the crystal.

The laser injection current was maintained at 2x threshold, which gave an

output of ~1 mW. The frequency was tuned by changing the temperature of the small Peltier cooler underneath the laser, or by changing the laser current, which also causes a change of temperature of the laser through ohmic heating. Both laser current and cooler temperature were controlled by a digital-to-analog converter and a microcomputer.

The laser frequency was modulated by applying a sinusoidal modulation on the injection current. The a.c. tuning rate of the laser at 10 kHz modulation was 0.022 cm^{-1}/mA (± 20%). The amplitude of the frequency modulation was varied to achieve the optimum SNR for each type of spectroscopic measurement, as will be explained below. The detector signal was sent to a lock-in amplifier referenced to twice the modulation frequency, and the output of the lock-in was collected by an analog-to-digital converter and a microcomputer.

A Burleigh 20 cm confocal etalon (FSR=150 MHz) was used for frequency calibration of the measurements of the crystal field splitting. While the laser frequency was tuned, a portion of the laser beam was split off before passing through the crystal, mechanically chopped, sent through the etalon and focused onto a detector. A second lock-in amplifier referenced to the chopping frequency was used to demodulate the signal, and the output of this lock-in was simultaneously collected with the solid hydrogen absorption signal by the analog-to-digital converter and microcomputer.

Reference lines of HCN were used for frequency calibration of the impurity splitting. The frequencies of these lines were provided by Sasada [78]. A portion of the laser beam was sent through a 50 cm long cell containing 10 torr of HCN, and the

absorption of the reference lines were monitored with 2f detection. Absorption of the HCN and solid hydrogen was recorded simultaneously, and linear interpolation between the HCN lines was used to determine the frequencies of the solid hydrogen transitions. Accuracy of this technique was estimated to be ~ 0.02 cm^{-1}. Improved accuracy could be achieved by using an etalon to measure the change in frequency in between the HCN absorption lines, but such an etalon was not available. The FSR of the Burleigh etalon described above was inconveniently small for this purpose.

5.3.3 Results

(a) Crystal-Field Splitting

The detection of the $W_{1\leftarrow 0}(0)$ transition was straightforward, since it was previously observed at lower resolution [74]. It was expected from the study of the $W_0(0)$ transition that the crystal field would split the $W_{1\leftarrow 0}(0)$ into three components [74] that had not yet been resolved. The previous frequency measurement [74] was found to be somewhat inaccurate: a frequency of 6441.75 ± 0.02 cm^{-1} was determined with the SXC diode laser spectrometer.

At line centre in an 11.5 cm-long crystal, the transition absorbs about 2.7% of the incident laser radiation. Detection of this transition was not difficult given the

sensitivity of the laser spectrometer using 2f detection. However, when the amplitude of the laser frequency modulation was set to produce the largest possible 2f signal, no splitting of the transition was observed. This amplitude was determined to be 0.08 cm^{-1} $\pm$ 20% peak-to-peak (2.4 GHz). This result suggests that the full-width at half-maximum (FWHM) of the transition is around 2.4 GHz/2.2 = 1.1 GHz (see Section 4.2.1), which is unreasonably large considering the observation that each component of the $W_0(0)$ transition has a FWHM of $\sim$140 MHz; there is no reason to believe that $W_{1\leftarrow0}(0)$ should have an appreciably larger linewidth. Possibly, because the three components are nearly blended, the combined linewidth is what is measured by 2f detection. If each component has a FWHM of 140 MHz, then the amplitude of modulation that produces the largest signal should be (3x140 MHz)x2.2 = 925 MHz, which is much closer to the observed results.

The frequency-modulation amplitude had to be reduced far below the value of 0.08 cm^{-1} required to produce the maximum 2f signal to reduce the modulation broadening. Such broadening prevented the observation of the crystal-field splitting. The modulation amplitude must be less than the splitting of the features to be resolved, but must still be sufficient to provide an adequate SNR. A peak-to-peak modulation amplitude of 60 MHz provided a good compromise between resolution and sensitivity.

Frequency scans were made with the laser emission polarized perpendicular to the c-axis of the crystal, which is the normal case for InGaAsP diode lasers. Scans were also made with the the laser emission rotated 90°. The result of the splitting of the

J=6 state by the crystal field is shown in Fig. 5.3. The dependence of the amplitude of the each component on the laser polarization is clear, and it indicates a specific orientation of the c-axis of the crystal. By probing different regions of the crystal with both laser polarizations, it was determined that the c-axis was oriented radially away from the longitudinal axis of the cylindrical crystal sample. Assignment of the three components is based on the predicted ordering of their frequencies and relative intensities, and follows the assignment of the splitting for the $W_0(0)$ transition found in [18]. The frequency difference between the $M=\pm4$ and the $M=\pm3$ transitions is 330 MHz ($\pm$ 15 MHz) and the difference between the $M=\pm2$ and the $M=\pm3$ is 420 MHz ($\pm$ 15 MHz).

(b) Impurity Splitting

The SXC laser and harmonic detection were used to detect and measure the splitting of the $W_{1\text{-}0}(0)$ transition caused by ortho-hydrogen impurities in the crystal. The splitting consists of several very weak transitions scattered through the 6438-6444 cm^{-1} frequency range. These transitions absorb only 10^{-2}% to 10^{-3}% of the incident radiation, so high sensitivity is required to observed them. Laser frequency modulation amplitude of 2.0 GHz ($\pm$ 20%) optimized the magnitude of the detected 2f lineshapes. However, the detected spectrum was badly contaminated by etalon fringes from the windows of the

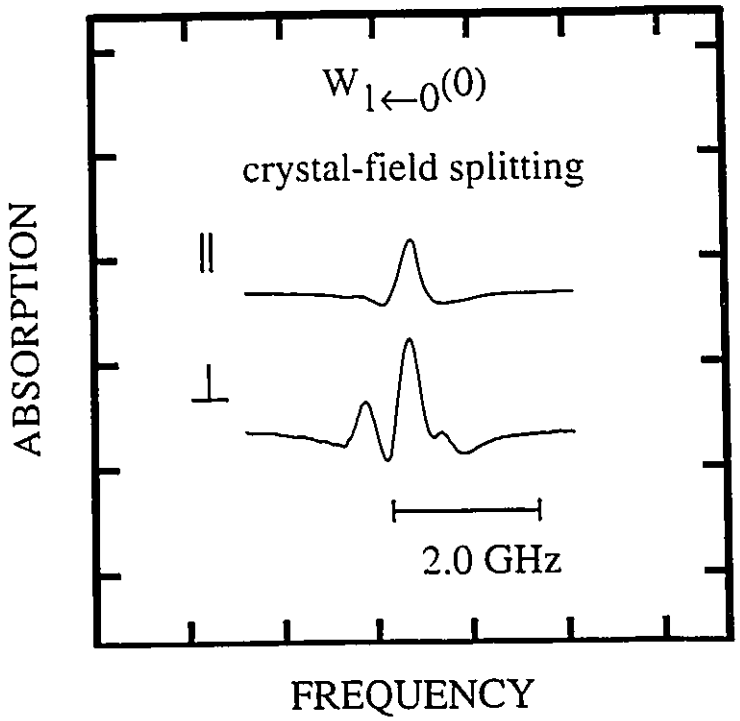

Figure 5.3

The crystal-field splitting of the $W_{1\leftarrow0}(0)$ transition of solid para-hydrogen. The incident laser radiation was polarized parallel to the crystal c-axis for the top trace, and perpendicular to the c-axis for the bottom trace.

sample cell, which had an FSR of 1.3 GHz. Only a few lines could be seen. However, the impurity splitting transitions likely have a linewidth that is about an order of magnitude smaller than the etalon fringe spacing, so the fringes and the spectral lines have a very different dependence on the frequency modulation amplitude. It was found that reducing the modulation amplitude to 400 MHz yielded the optimum signal for the impurity transition lines: the detected lines were reduced in size, but the fringes were reduced even further. In this way, a sensitivity of $\sim 10^{-5}$ was achieved. Figure 5.4 shows a sample of second-harmonic detection of the impurity transitions near the main $W_{1-0}(0)$ feature. The laser polarization in Fig. 5.4(b) is orthogonal to that of Fig. 5.4(a). From 6438 to 6444 cm^{-1}, several transitions were observed in both laser polarizations. Tabulation and assignment of the transitions was performed by T.J. Byers and K.E. Kerr and appears in [56,57].

5.4 Summary

An absorption spectrometer using SXC InGaAsP laser diodes was employed in two spectroscopic investigations. The accuracy to which the concentration of two isotopic species of the same molecule could be monitored was determined by finding the accuracy at which the magnitude of the second harmonic signal could be measured. It was found that the concentration ratio of HDO/H_2O could be monitored to within $\pm 4\%$.

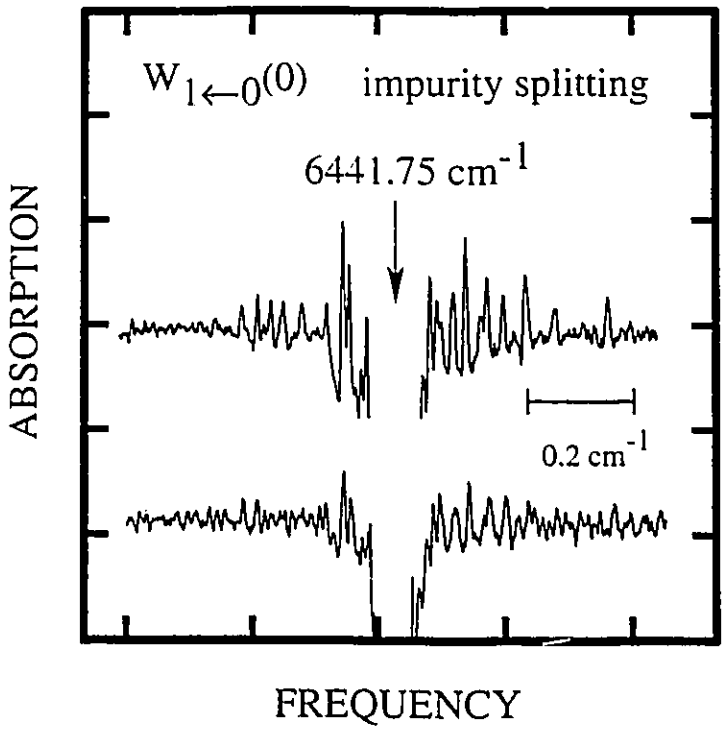

Figure 5.4

A portion of the splitting caused by the J=1 impurity transitions in solid para-hydrogen, in the vicinity of the main transition. Several more such transitions were found in the 6437-6445 cm^{-1} range. The signal-to-noise ratio allows transitions as small as 10^{-3}% to be detected.

Etalon fringes from the White cell used to hold the sample limited this number. The ratio of $^{13}CO_2/^{12}CO_2$ could be monitored to within $\pm 1\%$ because of improved SNR. The results presented here demonstrate the feasibility of using near-IR lasers in field monitors for detecting relative molecular concentrations. Applications exist in the fields of medicine, industrial monitoring, environmental studies, and petroleum exploration. The laser spectrometer was also used to measure the crystal-field and ortho-hydrogen impurity splitting of the $W_{1\leftarrow 0}(0)$ transition of solid para-hydrogen. The results are of interest to chemical physicists studying this fundamental quantum solid.

CHAPTER 6 - SPECTROSCOPY OF THE $3\nu_2 \leftarrow 0$ BAND OF H_3^+

6.1 Introduction

This chapter describes the use of SXC laser diodes in the measurement of the second vibrational overtone ($3\nu_2 \leftarrow 0$) band of the H_3^+ molecular ion. This ion is of great importance in the physics and chemistry of plasmas that consist predominantly of hydrogen, including those found in the interstellar medium and in laboratory-based hydrogen plasmas. It is also of fundamental interest to chemical physicists because it is the simplest stable polyatomic molecule and can provide an excellent test of *ab initio* calculations of molecular structure. SXC InGaAsP diode lasers are well-suited to the measurement of the $3\nu_2 \leftarrow 0$ spectrum because high sensitivity is required: the strongest absorption in the band is expected to be 10^{-3}%. The tunability of the SXC lasers is also an advantage, since the spectrum is widely and unevenly scattered over the 6800-7300 cm^{-1} spectral range. *Ab initio* calculations weer used to facilitate assignment of the spectra and to narrow the frequency range that was searched with the lasers. The results reported in this chapter are the first observation of the second vibrational overtone band

of any molecular ion, and they demonstrate the use of diode lasers in this area of molecular spectroscopy [79]. The following measurements were carried out during a collaboration with T. Oka, S.S. Lee, Z. Guo, and S. Joo of the University of Chicago, Departments of Chemistry and Astronomy and Astrophysics.

6.2 *History and Importance of the H_3^+ Molecule*

H_3^+ was first observed by J.J. Thompson in 1912 [80] during his investigations of "positive rays" in low-pressure, high-voltage electrical discharges. Later studies by Dempster [81] confirmed the existence of the molecule and greatly enhanced the yield by using electron bombardment of hydrogen gas; under certain conditions H_3^+ was the most abundant ion in the ionized gas. In 1925, Hogness and Lunn [82] deduced for the first time the reaction that forms H_3^+ in a discharge:

$$H_2 + H_2^+ \rightarrow H_3^+ + H \qquad (6.1)$$

Pioneering theoretical studies in the 1930's [83] indicated that H_3^+ should have a triangular rather than linear structure and that the above reaction is exothermic. Little more was known about the molecule at this time, although its existence was said to be "the scandal of modern chemistry" [84], particularly because the valency was not well understood. Interest in H_3^+ waned for the next 25 years, but was rekindled with the

advent of modern digital computers that could be used to perform detailed theoretical calculations. Since 1964 there have been dozens of theoretical papers describing the structure of H_3^+. Christoffersen [85] showed that the equilateral triangle configuration is the most stable and obtained more accurate values of bond length and formation energy. The *ab initio* calculations of Carney and Porter [86,87] provided very accurate predictions of vibrational frequencies and rotational and rotational-vibrational constants of the molecule. More recently, remarkably accurate *ab initio* calculations [88,89,90,91,92,93] by Miller and Tennyson at University College, London have mapped the energy structure of H_3^+ up to the $4\nu_2$ vibrational level using the potential surface calculated by Meyer, Botschwina and Burton [94]. These calculations have facilitated the assignment and identification of overtone, hot-band and forbidden bands of the molecule, as will be discussed in the next section.

The exceptional interest in H_3^+ is a result of the fundamental importance of the molecule in the chemistry of the interstellar medium (ISM) and in plasma discharges. The efficiency of (6.1) causes H_3^+ to be the most abundant molecular ion in hydrogen discharges [95]. The presence of the molecule also strongly influences the chemistry in the plasma. The abundance and distribution of H_3^+ in the discharge can therefore yield information on the conditions of the plasma, and measurement of these quantities can be accomplished non-intrusively by measuring the IR spectra of the molecules. Understanding the spectra of H_3^+ is therefore critical for spectroscopic plasma diagnostics of hydrogen discharges produced in the laboratory or in industrial processes. Details of

the production of H_3^+ in a laboratory plasma discharge cell will be described in detail in Section 6.4.1.

H_3^+ also has a crucial role in the chemistry of the interstellar medium [96]. It is produced by the ionization of H_2 by cosmic ray bombardment followed by reaction (6.1). The molecule then causes the protonation of other molecules by the reaction

$$H_3^+ + X \rightarrow HX^+ + H_2 \qquad (6.2)$$

which is favoured because of the high proton affinities of many common interstellar molecules compared to H_2 (proton affinity 4.4 eV). Some examples of molecules that react with H_3^+ (and corresponding proton affinities) are CO (6.1 eV), NH_3 (8.5 eV), CH_4 (5.4 eV), HCN (7.5 eV) and H_2O (7.3 eV). The resulting species are HCO^+, NH_4^+, CH_5^+, H_2CN^+, and H_3O^+; HCO^+ has already been observed in interstellar space.

H_3^+ is also responsible for the anomalous abundances of deuterated molecular ions such as DCO^+ and DN_2^+ observed in the ISM [97]. Fractionation of H_3^+ occurs through

$$H_3^+ + HD \leftrightharpoons H_2 + H_2D^+ \qquad (6.3)$$

which has an exothermicity of 7 meV (81 K) because of the lower zero-point energy of H_2D^+. Thus, H_2D^+ has a higher abundance in cool interstellar clouds than is expected from the natural abundance of HD. The apparent overabundance of deuterated molecular ions is then a result of the reaction

$$H_2D^+ + X \rightarrow DX^+ + H_2 \qquad (6.4)$$

which is similar to reaction (6.2).

Despite the inferred importance of H_3^+ in the chemistry of the ISM, the molecule has not yet been observed in interstellar space. A recent search by Oka and Geballe [98] has established an upper limit on the column density of 4×10^{14} cm^{-2}. More searches are planned and it is expected that improvements in the technology of IR telescopes and detectors will soon enable the detection of H_3^+ in the ISM.

However, emission lines of H_3^+ have been detected, quite by accident, in the northern auroral "hot spot" in the polar regions of Jupiter's atmosphere [99,100,101]. The detected lines were from ro-vibrational transitions of the fundamental ($\nu_2 \rightarrow 0$) and first overtone ($2\nu_2 \rightarrow 0$) bands of H_3^+. Analysis of the strengths of the transitions indicate a high temperature (1100 K) in this part of Jupiter's atmosphere. The presence of H_3^+ itself suggests a source of H_2^+; the ionizing mechanism is believed to be electron impact on H_2 from the Io flux torus [102]. In addition, the presence of H_3^+ in the upper atmosphere may affect the chemistry of the lower atmosphere through (6.2). H_3^+ has most recently been discovered in the equatorial regions of Jupiter, although the lines observed there are much weaker than in the polar regions [103].

H_3^+ has also been discovered recently in the atmospheres of Uranus and Saturn [103]. It is not known at what latitude the molecule was found in Uranus because of the difficulty in locating its polar axis. However, the discovery was a surprise because

Uranus has a much smaller magnetic field than Jupiter ($\sim 1/410$). No mechanism has been proposed for the production of strong plasma activity in the atmosphere of Uranus. The H_3^+ in Saturn is found in the polar regions, and is much weaker than in Jupiter.

6.3 Spectroscopy of H_3^+

A brief description of the ro-vibrational energy levels and selection rules of H_3^+ is given here. A more detailed description of the H_3^+ spectrum is given in [104,105], and general discussions of the spectroscopy of polyatomic molecules is found in [106,107].

The H_3^+ molecule has the geometry of an equilateral triangle, with a proton at each vertex, and is classified as an oblate symmetric rotor. It has no permanent dipole moment and therefore no purely electric-dipole-allowed rotational spectrum. In addition, it has no stable excited electronic states and therefore no discrete electronic spectrum. As a result, the only means of obtaining spectroscopic information is through the strongly allowed ro-vibrational electric-dipole transitions. This spectrum also provides perhaps the best method of detecting the molecule in space.

H_3^+ has three normal modes of vibration (Fig. 6.1). The

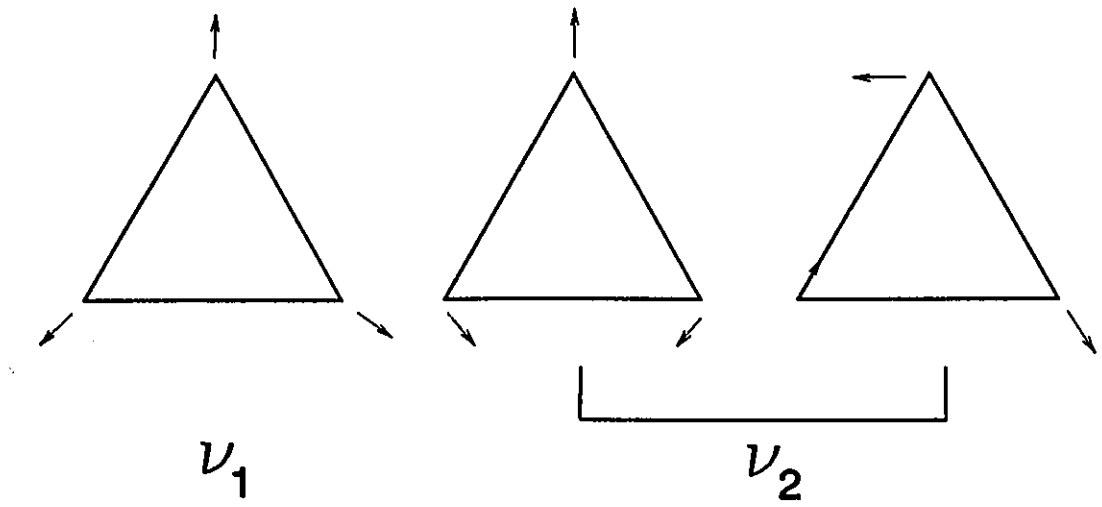

Figure 6.1

The normal vibrational modes of H_3^+.

ν_1 mode is a totally symmetric stretching vibration which has energy of 3178 cm^{-1}, and the ν_2 mode is a doubly-degenerate stretching vibration with energy 2521 cm^{-1}. Dipole transitions between the vibrational ground state and the ν_1 state are not strongly allowed, although weak forbidden transitions to this mode can occur. The transition between the ν_2 mode and the ground state is strongly allowed, and is in fact the strongest of all H_3^+ vibrational transitions: it is called the fundamental transition. The $\nu_2 \leftarrow 0$ absorption band was the first to be observed in the laboratory [108].

Transitions from the ground state to higher vibrational levels $(\upsilon_2)\nu_2$ with quantum number $\upsilon_2=2,3,\ldots$ are also allowed. These are called overtone transitions. In most molecules, the overtones are much weaker than the fundamental. In H_3^+, however, the light protons have very little inertia and the molecule undergoes large-amplitude vibrations which results in the relatively large intensity of overtone transitions. In fact, the Einstein coefficient for the first overtone $2\nu_2 \leftarrow 0$ transition is larger than that of the fundamental [93]. The Einstein coefficient for the $3\nu_2 \leftarrow 0$ ro-vibrational band is $\sim 8x$ weaker than the fundamental, but still has enough intensity to be observed in the lab.

Figure 6.2 is a diagram of the vibrational levels of H_3^+; the transitions that have been observed are indicated with an arrow. The first overtone was observed in emission by Majewski et al. [109] and in absorption by Xu et al. [110]. Hot and forbidden bands were observed by Bawendi et al. [111].

Each vibrational energy level has closely-spaced rotational levels associated

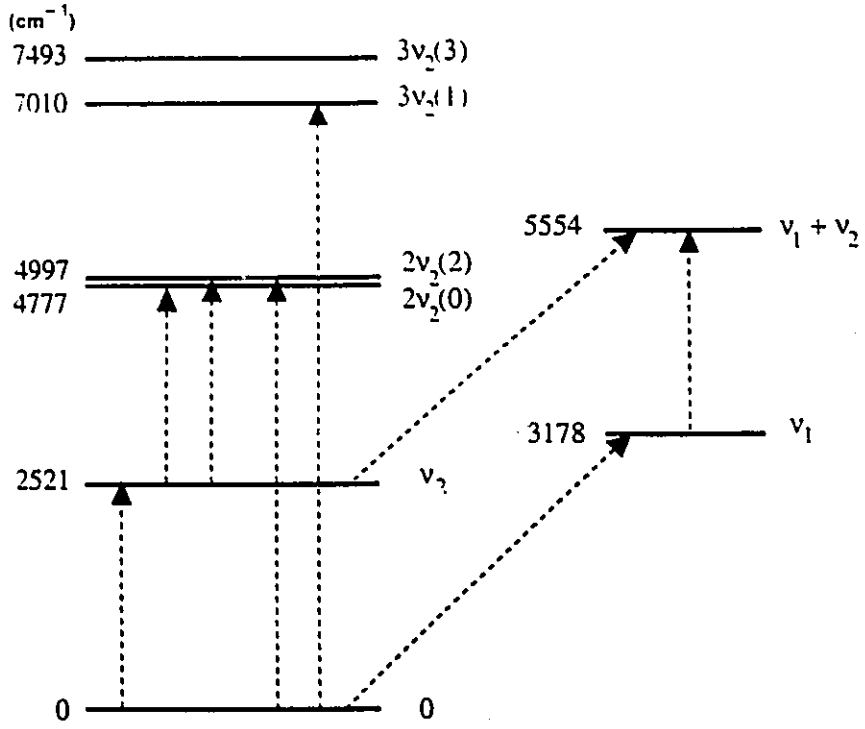

Figure 6.2

The vibrational energy levels of the H_3^+ molecule. Transitions that have been observed are indicated with a dashed line.

with it. The rotational wavefunctions are associated with the angular momentum quantum number J, and the projection of the angular momentum along the molecular axis, described by the quantum number k which has the values k=0,...,±J. For a completely rigid oblate rotor, the rotational energy is given by

$$E_{JK} = BJ(J+1) + (C-B)K^2 \qquad (6.5)$$

where B and C are the rotational constants of the rotor, C<B, and K= | k | . If the molecule is not completely rigid, there are additional terms of smaller magnitude in this equation that are proportional to higher orders of J and K and describe centrifugal distortion, Coriolis motion, and various types of interaction with the vibrational motion.

The ro-vibrational levels of the ground state of the degenerate vibrational mode are described by the quantum numbers v_2=0, J, and k. For the excited vibrational states of ν_2, there is a modification to the quantum numbers. The linear combination of the degenerate vibrational modes produces another component of angular momentum projected on the molecular axis described by the quantum number ℓ, which has allowed values of ℓ=0,...$\pm v_2$. This vibrational angular momentum couples strongly with the rotational angular momentum so that k and ℓ are no longer good quantum numbers. However, the combination G= | k-ℓ | is a good quantum number [105], so the excited vibrational states of the ν_2 mode therefore have quantum numbers v_2, J, and G. The degeneracy between the positive and negative ℓ states is lifted by vibration-rotation

interactions, and the quantity U is employed to distinguish between the (J,G) states. U is defined by $|U| = |\ell|$, and has a negative value for the (J,G) state with lower energy and positive value for the state with higher energy.

Requirements of symmetry and quantum mechanics greatly influence the observed spectra of all molecules. In H_3^+, the Pauli exclusion principle requires that the total wavefunction of the molecule be antisymmetric with respect to the exchange of two protons, because the protons are fermions. A consideration of the symmetry of each component of the total wavefunction in the ground vibrational state indicates that if k=0 and J is even, then the requirements of the exclusion principle are not fulfilled. These states therefore do not exist. In addition, an analysis of the symmetry of the nuclear spin wavefunctions shows that there are both ortho and para rotational states. The ortho states have K= 0,3,6,.., have total nuclear spin I=3/2, and have a statistical weight of 4. The para states have K≠ 0,3,6,..., have I=1/2, and have a statistical weight of 2. The rotational energy levels of the ground state are illustrated to scale in Fig. 6.3, which also shows the parity of the levels, given by $(-1)^k$. The ν_1, $2\nu_2(\ell=0)$ also have rotational structure similar to that of the ground vibrational state.

The excited vibrational states have a symmetry that does not preclude the existence of any rotational levels, but each G level is split into two, as mentioned above. Ortho states have quantum numbers G=0,3,6,... and all other states are para.

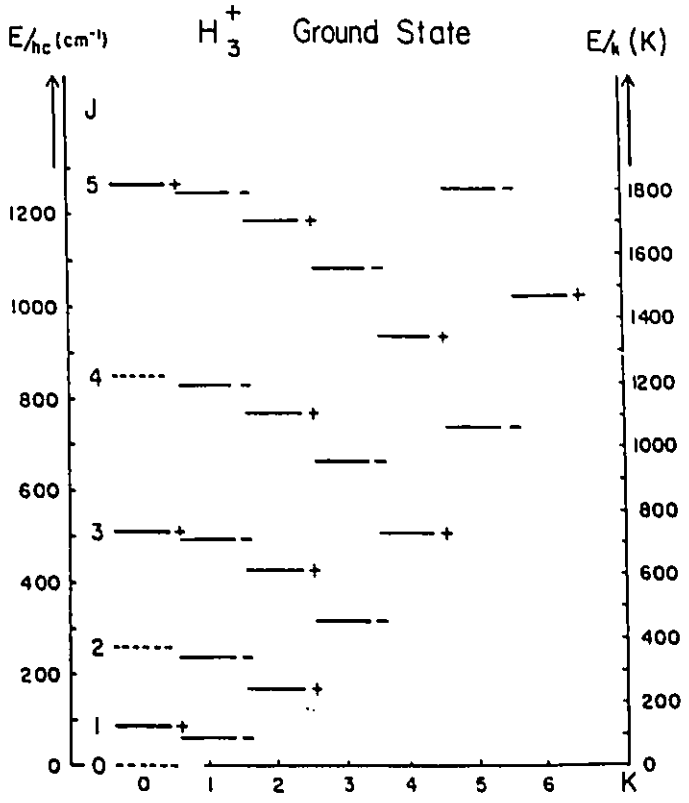

Figure 6.3

The rotational levels of the ground vibrational state of H_3^+. Forbidden levels are shown as dashed lines, ortho levels as bold lines, and para levels as fine lines. The parity is shown beside each level.

The rotational structure of the ν_2 state is shown in Fig. 6.4; the $2\nu_2(\ell=2)$ and $3\nu_2(\ell=1)$ states have structures similar to that of ν_2.

The selection rules are found by determining the constraints on the quantum numbers that are necessary to satisfy the condition

$$\langle v' J' G' \mid \mu \mid v'' J'' G'' \rangle \neq 0 \tag{6.6}$$

where ' and '' denote the upper and lower state quantum numbers, and μ is the dipole moment operator. This expression is most easily analyzed with the help of group theory, which gives the circumstances under which this condition is true [112]. The strongest H_3^+ transitions for $n\nu_2 \leftarrow 0$ are found to have the selection rules

$$\begin{aligned} \Delta J &= 0, \pm 1 \\ \Delta k &= \pm 1 \\ \Delta G &= 0, \ \ell = \pm 1 \quad (n \ odd) \\ \Delta G &= 3, \ \ell = \pm 2 \quad (n \ even) \end{aligned} \tag{6.7}$$

$\Delta J = -1, 0,$ and $+1$ correspond to the P, Q, and R branches, respectively.

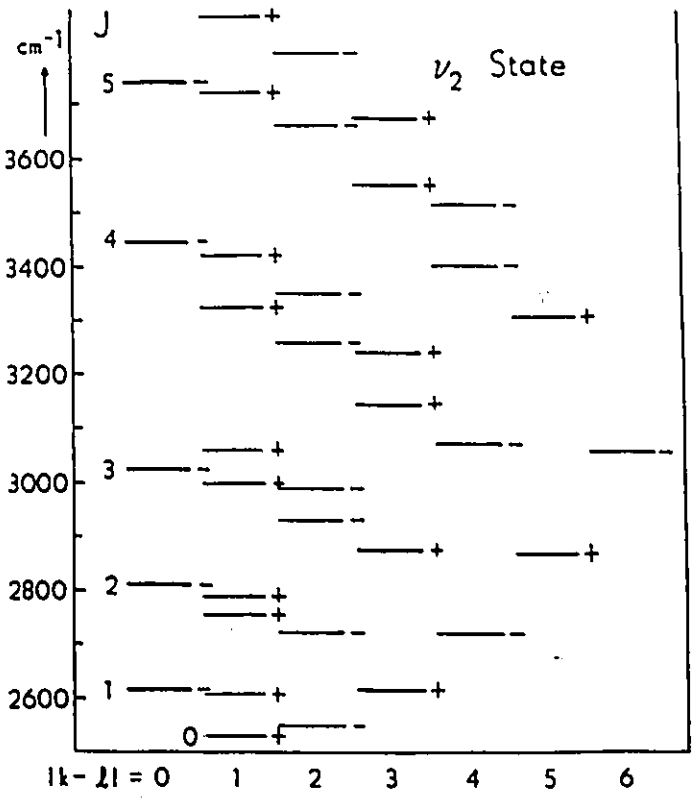

Figure 6.4

The rotational levels of the ν_2 vibrational state of H_3^+. Ortho levels are shown as bold lines, and para levels as fine lines. The parity is shown beside each level. Each $G = |k-\ell|$ state is split into two separate states by the vibration-rotation interaction.

6.4. *Experimental Method*

6.4.1. *Overview*

The H_3^+ transitions were detected by straightforward absorption spectroscopy. The laser vacuum module described in Chapter 2 was used for all measurements. Several SXC diode lasers with mode control techniques were used as radiation sources. The diode laser beam was collimated by two plano-convex f/1.3 lenses, focused at the entrance of a multi-pass a.c. discharge cell (Sect. 6.4.2) and passed through the cell. The light was collected by an InGaAs detector with a transimpedance amplifier which measured the change in laser power caused by absorptions from the molecules. If a single detector was used, the laser beam was first passed through a monochromator to filter out light from the discharge. If intensity noise subtraction was used (Sect. 6.4.3) the monochromator was not necessary because the extraneous light from the discharge was subtracted. The detector signal was demodulated by a lock-in amplifier referenced to a multiple of the discharge frequency (Sect. 6.4.3). A sample of the laser beam was split off before the absorption cell and sent to a wavelength meter (Burleigh model WA-20, modified for IR use) for frequency calibration of the spectra. The wavelength meter was calibrated using H_2O absorptions lines from the AFGL database [65]. The

SXC lasers were tuned manually to the frequency region of interest, then scanned by a microcomputer over a range of a few wavenumbers. The microcomputer simultaneously collected the absorption spectra.

Although the basic concept of this experiment is simple, there are several complications that arise in ion absorption spectroscopy that require further discussion.

6.4.2. Production of H_3^+

The production and behaviour of plasmas is still poorly understood despite a century of study. Non-intrusive measurement of molecular and electron concentrations and velocity and temperature distributions are notoriously difficult. The chemical reactions that occur in a plasma are also difficult to analyze: plasma chemistry is therefore almost like alchemy. As a result, adjusting the composition and conditions of a plasma to yield the optimum concentration of a particular molecular ion is usually accomplished empirically.

In this experiment, H_3^+ ions were produced in a liquid-nitrogen-cooled a.c. discharge cell dubbed "The Black Widow" (Figure 6.5). The cell was made of Pyrex and has three concentric chambers: the outer chamber is evacuated to provide insulation, the middle chamber is filled with liquid N_2 from an external dewar, and the central cylindrical chamber contains the gas that is to be ionized. The bellows on the outer chamber provide relief from the strain caused by expansion and contraction

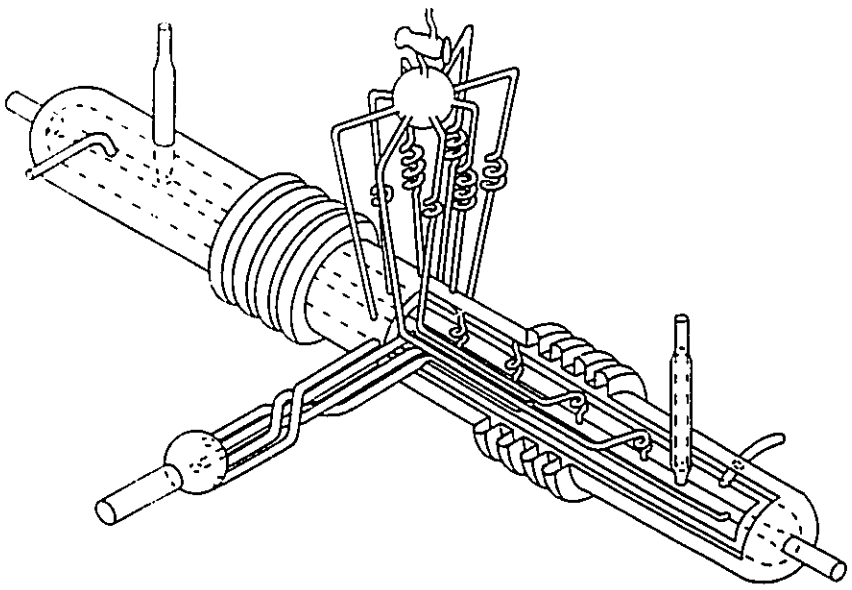

Figure 6.5

A drawing of the liquid-nitrogen-cooled discharge cell used to produce H_3^+ (courtesy of M-F. Jagod, University of Chicago).

of the glass. Gas is delivered to and extracted from the inner chamber in a way that ensures an even mixing of gas in the plasma-forming region. The ends of the cell are fitted with water-cooled electrodes and sealed with CaF_2 Brewster windows. The diameter of the inner chamber is 18 mm and the length of the cell is 1 m. These dimensions were empirically determined to be optimum for H_3^+ production and detection with diode lasers [113].

Liquid-N_2 cooling is necessary to maintain a significant fraction of the H_3^+ molecules in the lower rotational levels of the ground vibrational state. Experience indicates that the rotational temperature is roughly 500 K in the Black Widow. If a higher temperature was needed, a water-cooled cell ("the Tarantula") was employed.

A schematic of the electrical connections to the discharge cell are shown in Figure 6.6. An audio frequency generator outputs a 6 kHz sine wave with an amplitude of 10 V at a current of a few milliamperes and is connected to a power amplifier which increases the voltage by a factor of 4 and increases the current to about 8 A. A 40:1 step-up transformer is then used to increase the voltage to $\approx$1.6 kV and reduce the current to 200 mA. The current is passed through a bank of ballast capacitors and then through the discharge cell by water-cooled electrodes, which are

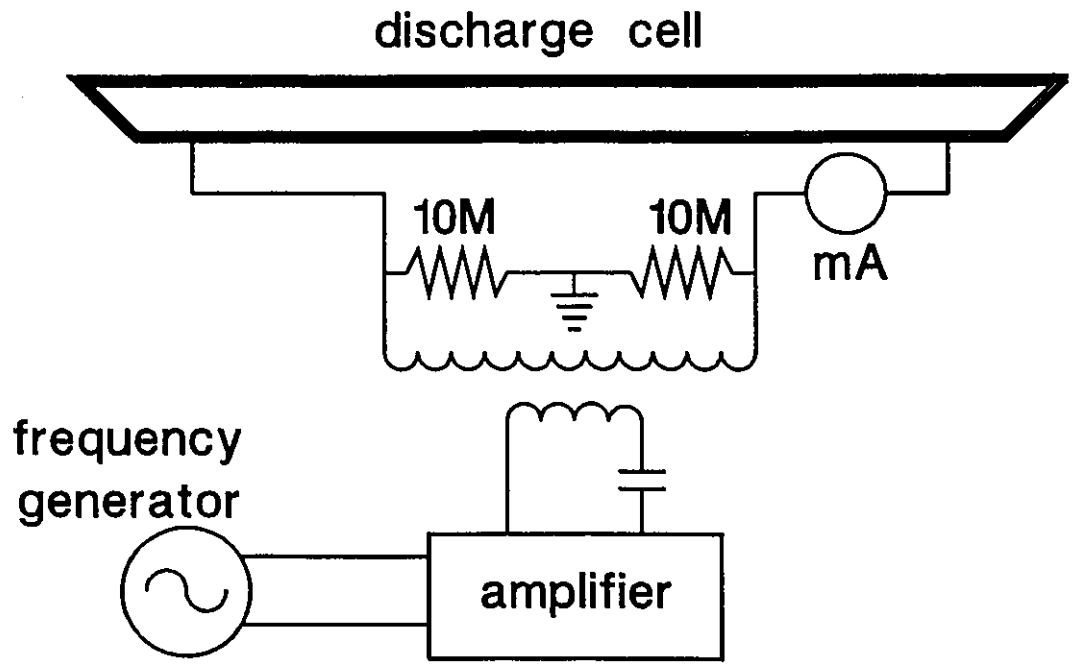

Figure 6.6

The electrical schematic for the gas discharge in which H_3^+ is produced.

isolated from ground by 10 MΩ resistors. The cell is designed so that the laser radiation passes only through the positive column of the discharge, which has a constant electric field as a function of position in the cell. The frequency, current and voltage of the a.c. discharge were determined empirically to give the optimum absorption signal for the $3\nu_2 \leftarrow 0$ H_3^+ transition.

During plasma production, hydrogen gas was continuously flowed into the discharge cell and the reactants were continuously pumped out with a mechanical vacuum pump. The gas flow rate was adjusted to maintain a pressure in the discharge of 1-1.5 Torr of H_2 gas and 0-6 Torr of He gas, depending on the desired chemistry. The addition of helium gas into the plasma increases the effective electron temperature, and has the effect of rendering the plasma more electrically stable. The most important chemical reaction in the plasma is equation (6.1); the H_2^+ is produced by electron bombardment in the discharge. The number density n of electrons in the discharge is obtained from

$$J=nev \qquad (6.8)$$

where J is the current density (A/cm^2), e is the electron charge and v is the drift velocity of the electrons. The charge neutrality condition of a plasma requires the number density of cations to be equivalent to that of the electrons. Since the electron velocity is typically $v \sim 10^7$ cm/s [114], and the current in the discharge cell (radius=9 mm) is 200 mA, the current density is 80 mA/cm^2. Assuming H_3^+ is the most abundant ion in the plasma,

its number density is therefore $\sim 10^{10}$ cm^{-3}. This makes the abundance of ions relative to neutrals about 10^{-5} to 10^{-6}.

6.4.3. Modulation Techniques for Ion Spectroscopy

The small abundance of ions relative to neutral species in the plasma discharge is a serious hindrance to the measurement of ion absorption spectra. Often the neutral species have absorption bands that overlap those of the ions, and the much larger abundance of neutrals in the discharge results in the weak ion absorptions being obscured and impossible to observe. If, for example, source modulation techniques such as harmonic detection are used, all molecular absorptions at the laser frequency will be observed. This problem is inherent in the observation of all molecular ion absorption spectra. Fortunately, an extremely clever method was devised by Gudeman et al. [115] that discriminates between absorption signals from neutrals and ions. This technique, called *velocity modulation*, exploits the Doppler shift that occurs when the ion is accelerated toward the electrode of opposite polarity. If the polarity of the electrodes is reversed periodically, the absorption frequency of the ion will be alternately red and blue-shifted relative to the laser frequency. This is equivalent to modulating the laser frequency at the rest frequency of the molecule, as in harmonic detection, but the effect is observed only for ionic absorptions. The detector that monitors the absorption signal

is demodulated by a lock-in amplifier, and a first-derivative-shaped signal is observed. The amount of frequency shift observed in the laboratory frame is comparable to the Doppler-broadened linewidth for most small ions in the positive column of a glow discharge [116] so the sensitivity is in principle comparable to harmonic detection. Another advantage of velocity modulation is that the etalon fringes that were detected when the laser frequency was modulated (Chapter 4,5) will not be present when velocity modulation is used. As a result, the sensitivity will then be limited only by the laser intensity noise, which is $\sim 10^{-6}$ in a 0.1 Hz bandwidth at the 6 kHz detection frequency.

Another technique useful for ion spectroscopy is *concentration modulation*. During a single cycle of the discharge, the concentration of all transient molecules (ions or neutrals) is varied twice, since the production of the transients does not depend on the polarity of the discharge. The detector signal is demodulated by the lock-in amplifier at the second harmonic of the discharge frequency. This method is analogous to using a light chopper, except that instead of chopping the laser beam, the concentration of the molecules themselves is "chopped" by the discharge at twice the modulation frequency. The absorption profile detected with concentration modulation depends on the phase of the lock-in amplifier and whether the molecule is a neutral or an ion. For an ion, the absorption profile has contributions from both the velocity-modulated lineshape and the absorption caused by the presence of ions after the extinction of the discharge. Each contribution has a different phase dependence, so the separate contributions to the lineshape can be observed by varying the phase of the lock-in [117].

Because the concentration of both ions and neutrals is modulated, concentration modulation does not allow the selectivity for ion spectroscopy that is provided by velocity modulation. When concentration modulation was used in this experiment, for example, the H_3^+ spectra were obscured by previously unobserved Rydberg transitions of molecular hydrogen. Although these transitions could be partially quenched by the addition of helium into the discharge, they still were much stronger than the H_3^+ lines. For this reason, velocity modulation was used exclusively to measure the ion spectra in this experiment.

6.4.4. Multi-pass Optical Arrangement and Noise Subtraction

To enhance sensitivity even further, a multi-pass optical configuration was used. Velocity modulation requires that the laser beam pass in only one direction through the cell, so a "bow-tie" configuration was devised to satisfy this restriction (Fig. 6.7). Up to 6 passes through the discharge cell were possible with this arrangement, resulting in a total absorption path length of 6 m. The number of passes was limited by the diameter of the multi-pass mirrors and the dimensions of the cell itself.

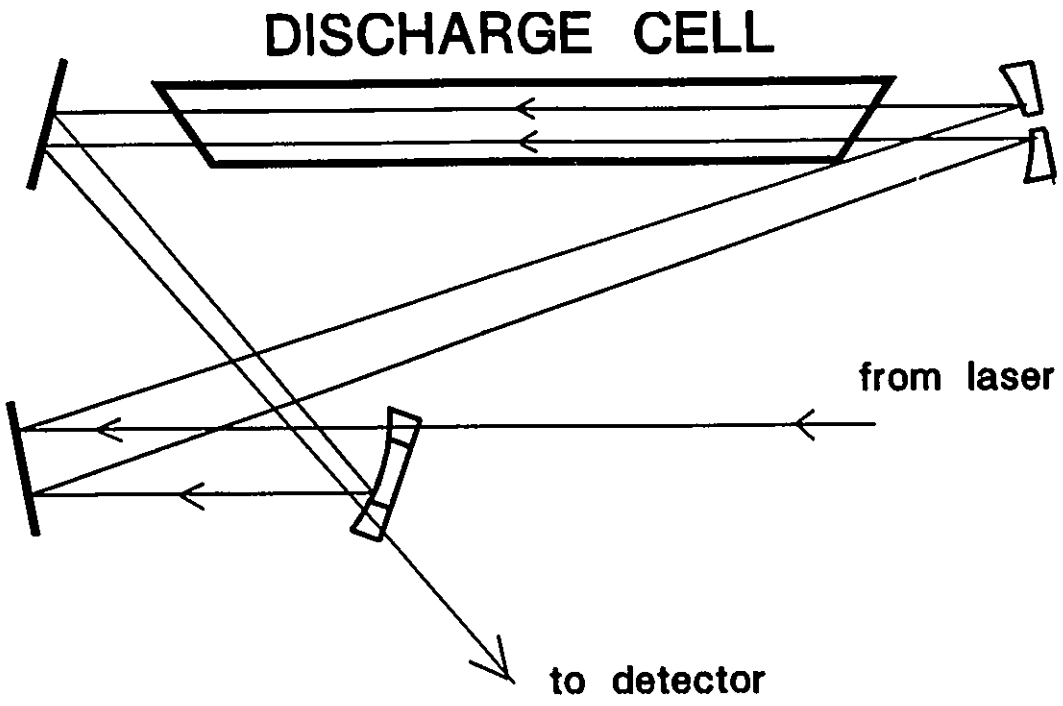

Figure 6.7

The single-direction, multi-pass "bow-tie" optical configuration to increase the absorption path through the discharge cell.

To detect very weak transitions, the single-direction multi-pass arrangement shown in Fig. 6.7 was modified to allow laser intensity noise subtraction [118]. The laser beam was split in two parts of equal intensity by a beam splitter and each beam was passed through the multi-pass arrangement in *opposite directions* (Figure 6.8). The beams were focused onto matched InGaAs detectors and the signals were subtracted and demodulated by the lock-in amplifier. Any random intensity flucuation on the laser will cause an identical fluctuation in each detector that will cancel out upon subtraction. The ion absorption signals at each detector will also be subtracted, but because they are of opposite phase, the net effect is to add the absorption signals from the two detectors. A significant increase in signal-to-noise ratio can be realized with this technique: in principle, the shot-noise limit can be reached. However, the alignment of the optics is difficult and even small mirror vibrations will destroy any advantage that this technique offers. Under ideal conditions, an increase in SNR of 3x to 5x is possible, resulting in sensitivity near 10^{-7}. This is the first time noise subraction has been used with a diode laser and the velocity modulation technique. Previous attempts with Pb-salt diode lasers were not successful, possibly because of the poor beam quality of these lasers.

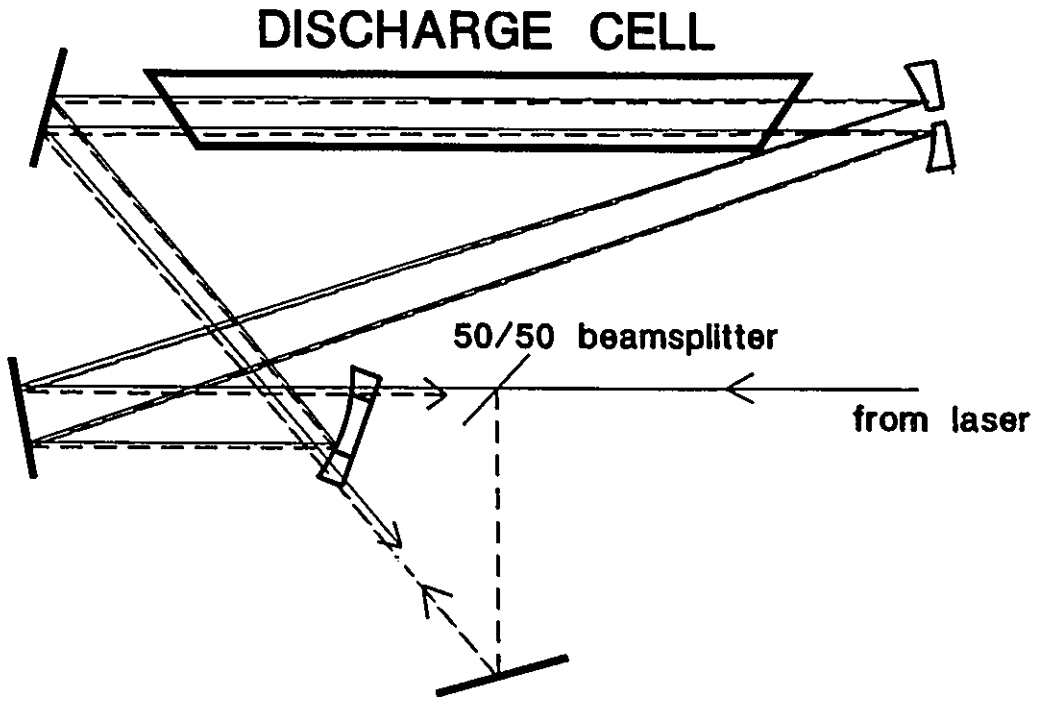

Figure 6.8

The bi-directional, multi-pass optical configuration used to implement laser intensity noise subtraction.

6.4.5. Electrical Noise

The high-voltage a.c. discharge is a source of pervasive electrical noise that can degrade the sensitivity with which H_3^+ absorptions can be detected. The electrical noise finds its way into the detection system through ground loops and electrical inductive pickup. One result of this noise is an offset on the lock-in amplifer's output. This noise is a common problem in plasma spectroscopy, and complete isolation from the problem is very difficult. The noise is especially difficult to filter because it is by nature at the detection frequency of the lock-in amplifier. A second concern was a.c. pickup on the laser current driver, which caused unwanted modulation of the laser current and resulted in 1f detection of absorption lines from ambient H_2O in the laboratory air. These absorption signals had the potential for obscuring the ion signals. A systematic study of the noise suggested some strategies that were found useful for the reduction of these problems.

Standard practices were used to reduce pickup through ground loops. The laser and detection electronics were grounded at the same point on the same lab circuit. The discharge electronics were grounded on a separate line.

The high voltage electronics for the plasma discharge were located as far as was

practical from the detection system. However, the reference signal for the lock-in had to be carried from the signal generator on a 3 m co-axial cable past the discharge cell to the lock-in amplifier. It was strongly suspected that there was pickup on this cable that found its way into the lock-in and into the laser electronics. The most effective solution was the insertion into the reference signal path of a circuit using an optical isolator chip (Optek 4N36). This circuit reduced the offset and the pick-up on the electronics by a factor of 4.

Pick-up on the InGaAs detectors also produced an offset of the output of the lock-in amplifiers, which increased the noise level. This offset was minimized by operating the detectors from batteries rather than the d.c. supply used to power the laser electronics. The aluminum casing of the detector had also to be grounded to the battery, and the detector had to be electrically isolated from the optical table. These precautions limited the offset of the lock-in output to less than 20 μV, which was comparable to the size of the absorption signals from H_3^+.

6.5 Results and Discussion

Fifteen H_3^+ ro-vibrational transitions of the $3\nu_2(1)\leftarrow 0$ band have been observed to date. The observed frequency, predicted frequency and assignments are found in Table 6.1. The accuracy of the measurements are estimated to be 0.01 cm^{-1}, limited by the accuracy of the wavelength meter. Figure 6.9 is an example of the absorption

Table 6.1

Observed transitions of the $3\nu_2(l=1)\leftarrow 0$ band of H_3^+.

Spectral Term	Transitions J',G',U←J",K"		Observed (cm^{-1})	Theoretical (cm^{-1})	(Obs.-Theo.) (cm^{-1})
$^{R}R(4,4)$	5,4,1	4,4	7265.852	7262.594	3.258
$^{R}R(1,0)$	2,0,1	1,0	7241.211	7238.493	2.718
$^{R}R(1,1)$	2,1,1	1,1	7237.243	7234.512	2.731
$^{R}R(3,3)$	4,3,1	3,3	7234.920	7231.753	3.167
$^{P}R(2,2)$	3,2,-1	2,2	7192.913	7189.700	3.213
$^{P}R(1,1)$	2,1,-1	1,1	7144.182	7141.177	3.005
$^{R}Q(4,3)$	4,3,1	4,3	6891.792	6888.499	3.293
$^{R}Q(5,3)$	5,3,1	5,3	6883.061	6979.669	3.392
$^{R}P(2,2)$	1,2,1	2,2	6877.512	6874.953	2.559
$^{R}Q(5,0)$	5,0,1	5,0	6866.338	6862.913	3.425
$^{R}P(2,1)$	1,1,1	2,1	6865.708	6863.040	2.668
$^{R}P(3,0)$	2,0,1	3,0	6811.374	6808.713	2.661
$^{R}P(3,2)$	2,2,1	3,2	6807.714	6805.114	2.600
$^{R}P(3,3)$	2,3,1	3,3	6807.275	6804.796	2.479
$^{R}P(3,1)$	2,1,1	3,1	6806.633	6804.010	2.623

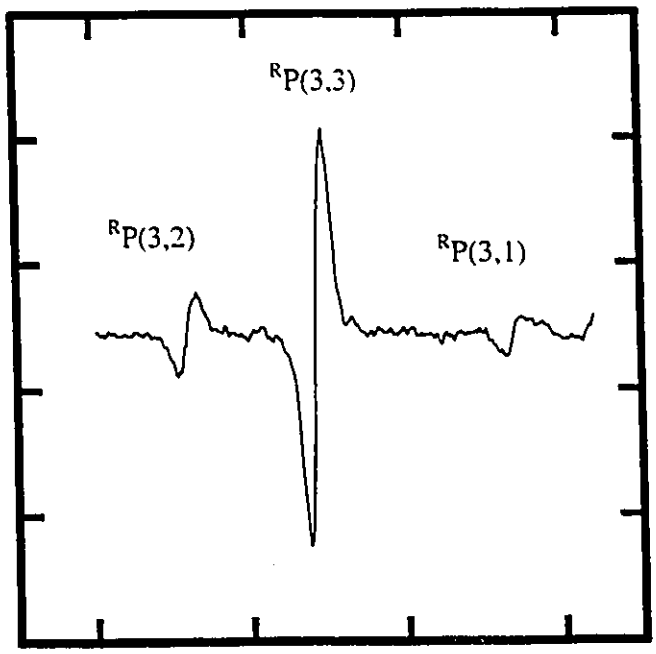

Figure 6.9

A frequency scan of three closely space H_3^+ absorption transitions in the P-branch of the $3\nu_2(1)\leftarrow 0$ band. The time constant was 3 s, and laser intensity noise subtraction was used.

spectrum measured using noise subtraction.

To confirm that each line was from an ion, the polarity of the discharge was reversed and the spectrum measured again. If the line shape reversed polarity, then it was caused by an ion or possibly a Rydberg state of H_2. The spectrum was also measured with and without the addition of about 5 Torr of helium into the discharge. If the strength of the absorption did not change appreciably, then the ion was surely H_3^+, rather than an ion with helium as a constituent. Helium also reduced the intensity of the H_2 Rydberg states appreciably so that they could be distinguished from H_3^+.

Figure 6.10 shows the effect of laser intensity noise subtraction. An increase in the signal-to-noise ratio of 3 to 5 was achieved with extremely careful alignment of the multi-pass optics. The light from the glow discharge is also removed by subtraction, so the need for a monochromator was eliminated, resulting in an increase of 5x in laser power incident on the detectors. The main difficulty in implementing this technique was separating the exit beams from the entrance beams. Optimum alignment of the optics requires the two beams to be exactly colinear, which makes such separation impossible. It was therefore necessary to slightly "dealign" the optics by diverting each input beam into the multi-pass optics at a small angle. The resulting output beams were displaced from the input beams and could tben separated with appropriate mirrors. Unfortunately, this strategy was hampered by the spherical mirrors at the heart of the multi-pass optical system, which were of limited aperture and left little room for the separation of the input

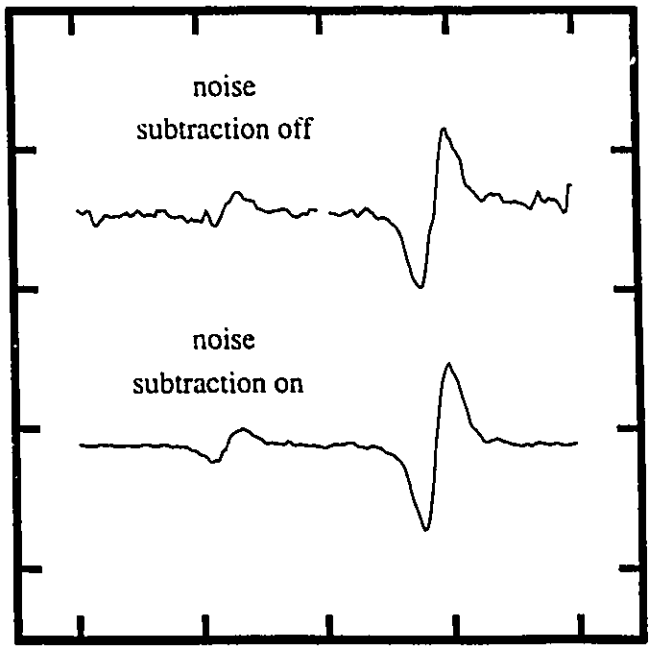

Figure 6.10

The effect of laser intensity noise subtraction on the H_3^+ spectra. For the upper scan, the signal from two matched detectors was subtracted and demodulated with a lock-in amplifier. For the lower scan, one detector was blocked. The detection time constant for both scans was 3 s.

and left little room for the separation of the input and output beams. It was difficult to keep all the reflection on the mirrors over a 4 m path. If one beam only partially hit the mirrors, then any small vibration destroyed the equality of the optical paths and the resulting noise would increase rather than decrease. Larger mirrors of identical focal length would solve this problem, and would also allow additional passes through the discharge cell resulting in a longer path length.

The upper state of H_3^+ in this band is highly vibrationally excited and because the molecule consists of light atoms, the vibrational amplitude of motion is large and the spectrum is expected to deviate significantly from that of an ideal oblate symmetric rotor. Even if the entire band could be observed, it would be very difficult to assign the lines on the basis of the spectral pattern. For these reasons, the assignment was accomplished using the *ab initio* calculations of Miller and Tennyson, which make no assumption of small vibrations about equilibrium geometry or coupling of vibrational and rotational motion. The *ab initio* calculations were assigned by Miller and Tennyson on the basis of symmetry, energy and line strengths. *Ab initio* calculations have been used in the past to assign the fundamental, first overtone, hot-band and forbidden bands of H_3^+ [108,110,111]. Figure 6.11 shows the predicted frequencies and intensities of some strong H_3^+ transitions in the 6600-7600 cm^{-1} region; the transitions that have been observed are indicated.

Two lines could not be assigned strictly on the basis of the *ab initio* calculations. The $^sQ(5,0)$ and the $^sP(2,1)$ transitions fall within 0.7 cm^{-1} of each

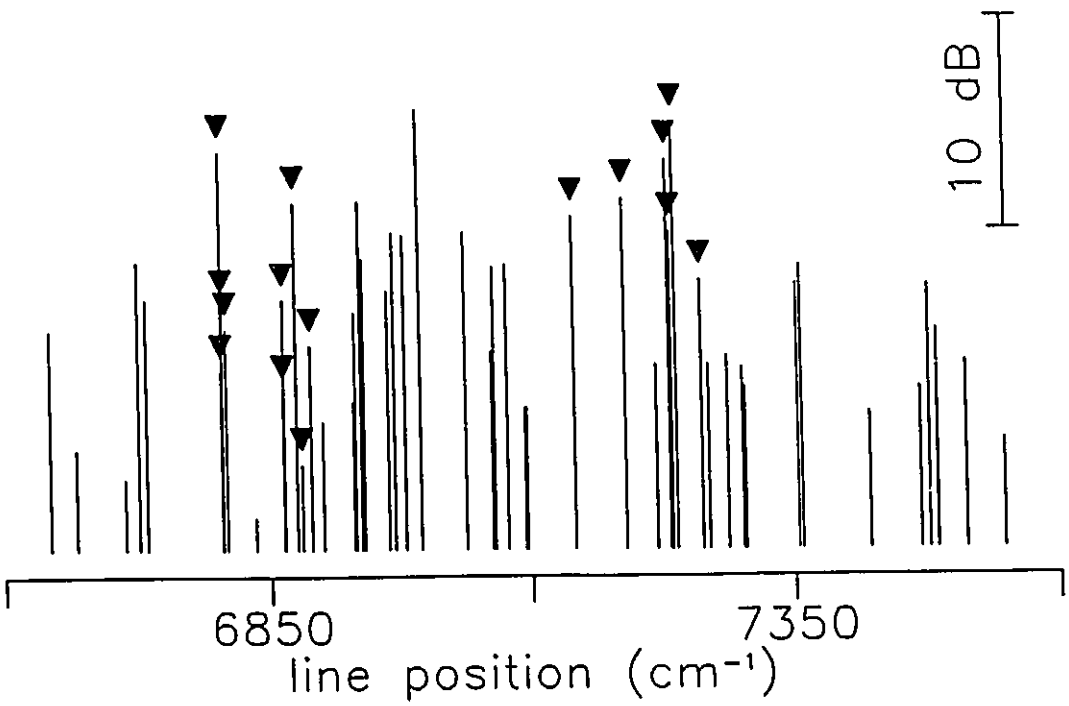

Figure 6.11

The predicted positions and intensities of the second vibrational overtone of H_2^+, from Miller and Tennyson's calculation assuming a temperature of 300 K. The strongest line is 1.18×10^{-19} cm/molecule. The lines marked with an inverted triangle have been observed in this thesis.

other, and they could not be distinguished. Assignment was made by studying the behaviour of the ratio of the intensities of the lines when the molecule was produced in both a liquid-N_2 cell ($T_{rot} \sim 500$ K) and a water-cooled cell ($T_{rot} \sim 700$ K). The $^RQ(5,0)$ line should be stronger in the water-cooled cell because of the higher rotational temperature, while the opposite holds for the $^RP(2,1)$ line.

The availability of accurate *ab initio* calculations is unusual in molecular spectroscopic studies, and it simplifies the analysis of the observed line frequencies. Traditionally, the observed line frequencies are fitted to a phenomenological Hamiltonian that describes the various contributions to the energy of the transition. The accuracy of the *ab initio* calculations limits the usefulness of such a Hamiltonian. Also, because only fifteen lines were observed, no such attempt could be made. Many more lines would be necessary for an accurate fit: for example, the Hamiltonian for the fundamental ν_2 band has 23 parameters that fit 44 transitions [119]. In the present case, the highly excited vibrational state of the molecule is expected to introduce many more interaction and perturbation terms.

The observed frequency of all transitions was higher than the predicted frequency by an average of 3.370 cm^{-1} for the Q-branch transitions and 2.598 cm^{-1} for the P-branch. These differences indicate that the potential surface used by Miller and Tennyson is somewhat "soft" for the higher vibrationally-excited states, although the accuracy of their calculations is still remarkable. Unfortunately, the absolute strengths of the transitions could not be evaluated because the number density of H_3^+ in the

discharge and the rotational temperature of the discharge were not accurately known. However, the observed relative intensity of the lines qualitatively followed the theoretical intensities that were expected for a rotational temperature of ~ 500 K. It is hoped that the observed frequecies will allow these researchers to adjust the potential surface to allow more accurate predictions of the third vibrational overtone of H_3^+; an experimental search for this overtone will be attempted in the near future [120].

6.6 Summary

Near-infrared InGaAsP SXC diode lasers have been successfully used to observe the $3\nu_2(\ell=1)\leftarrow 0$ band of the H_3^+ molecular ion. Observation is made possible by the unusually large dipole moment for this overtone band and by the high detection sensitivity that can be achieved with SXC diode lasers. The results presented in this chapter are the first observation of the second vibrational overtone of any molecular ion.

The observed frequencies fall within ≤ 3.5 cm^{-1} of predicted frequencies of the *ab initio* calculations of Miller and Tennyson. The Q-branch transitions were further off than the P-branch transitions. Absolute linestrengths could not be determined from the observations, but the relative intensities of the transitions agreed with the theoretical calculations. The observed frequencies can be used as a test of the calculations and allow

further refinements to be made to the molecular potential energy surface. Refined calculations can then be used to predict the frequencies of higher vibrational overtones and to obtain a better understanding of the highly-vibrationally excited states of this molecule. Finally, it is hoped that the results of this chapter will allow the observation of the second overtone band of H_3^+ in the auroral hot-spot of Jupiter's atmosphere, and that such observations will lead to improved understanding of this planetary system.

CHAPTER 7 - CONCLUSION

7.1 Summary of the Thesis

This thesis has described short-external-cavity semiconductor diode lasers for use in pure and applied research in molecular spectroscopy. The frequency of emission these lasers can be tuned over a wide range by altering their temperature, and the external cavity forces the laser to operate in a single longitudinal mode. The operation of SXC diode lasers was explained in Chapter 2, and an apparatus for extending the range of temperature operation of the lasers was presented. This apparatus allowed frequency tuning of 1.3-1.55 μm InGaAsP lasers over a range of $\sim$200 cm^{-1} (45 nm), and 0.76 μm AlGaAs lasers over $\sim$500 cm^{-1} (27 nm). A method for controlling the operation of the longitudinal modes of the laser was discussed in Chapter 3, and the technique was optimized using the principles of control theory. The SXC lasers and mode control techniques were used as radiation sources in an absorption spectrometer, which was discussed in Chapter 4. Using harmonic detection techniques, the spectrometer could measure absorptions as small as 3x10^{-4}% with an ENBW of 1.25 Hz, and a sensitivity

of 10^{-1} % was routinely attainable. The sensitivity was limited by etalon fringes caused by optical elements in the detection path, but is not a fundamental limitation of the system. A comparison was also made of the operation of the system with both SXC and distributed feedback InGaAsP laser diodes. The spectrometer was used in Chapter 5 to investigate the accuracy with which the abundances of HDO and H_2O and $^{13}CO_2$ and $^{12}CO_2$ could be measured. The results indicate that changes as small as 1 % could be detected in the concentration of the one isotopic species relative to another. Chapter 5 also described the investigation of the $W_{1\leftarrow0}(0)$ ro-vibrational transition in solid hydrogen. The crystal-field and ortho-hydrogen impurity splittings of this transition were measured. Finally, Chapter 6 described the measurement and assignment of the $3\nu_2(1)\leftarrow0$ ro-vibrational band of the H_3^+ molecular ion. It is hoped that this measurement will lead to better understanding of the highly excited states of this molecule, and perhaps facilitate the detection of this particular band in the highly ionized auroral regions of the atmosphere of Jupiter.

7.2 Suggestions For Further Research and Development

Several areas remain to be investigated. An improvement in the signal-to-noise ratio of the absorption spectrometer would allow more sensitive detection of molecular absorption transitions. Subtraction of laser intensity noise is a means of achieving shot-

noise-limited sensitivity with diode lasers, but the noise subtraction method presented in Chapter 6 did not achieve this limit. It was not clear what prevented the shot noise limit from being reached. A better matching of detectors or processing of the detector signal may help.

Ample opportunity exists for the development and commercialization of a diode laser-based trace-gas monitor for clinical or field use. The work presented in this thesis demonstrates the sensitivity that can be achieved in the laboratory with single-mode diode lasers, and careful and creative engineering can lead to the development of such monitoring systems. In addition, it is not understood what limits the accuracy to which the concentration of two molecules can be determined. It is possible that the answer lies with the frequency stability of the lasers.

The short-external-cavity system can be modified to narrow the linewidth of a single longitudinal mode of these lasers to the kilohertz level. The addition of a high finesse, long external cavity to the SXC lasers has already been attempted [121]. Such modifications reduce the linewidth at the expense of the continuous tuning range, however. A laser with such spectral purity would have applications in hole-burning spectroscopy of gases or in coherent communications systems. The mechanical stability of the SXC may also be improved by replacing the external mirror with an InP waveguide which has an optical length that can be controlled electrically.

An attempt should also be made to use the SXC configuration with other types of diode lasers based on III-V semiconductors, such as InSb lasers which operate in the

1.7-2.2 μm region. These lasers are attractive for use in trace-gas detection because the molecular transitions in this region are intrinsically much stronger than the 0.7-1.5 μm region, so that much smaller concentrations of trace gases can be observed.

The work presented in this thesis has demonstrated the utility of short-external-cavity near-IR diode lasers as versatile and economical radiation sources for molecular spectroscopy. The devices currently fill a niche in diode laser instrumentation by providing a low-noise, tunable, single-mode laser source that compares favourably with more expensive lasers structures. The techniques described in this thesis may continue to have application for some time to come.

REFERENCES

1. R.S. Eng, J.F. Butler and K.J. Linden, *Opt. Eng.* **19**, 945 (1980).

2. R.N. Hall, G.E. Fenner, J.D. Kingsley, T.J. Soltys, and R.O. Carlson, *Phys. Rev. Lett.* **9** 366 (1962).

3. M.I. Nathan, W.P. Dumke, G. Burns, F.H. Dills, and G. Lasher, *Appl. Phys. Lett.* **1**, 62 (1962).

4. N. Holonyak Jr. and S.F. Bevacqua, *Appl. Phys. Lett.* **1**, 82 (1962).

5. T.M. Quist, R.J. Keyes, W.E. Krag, B. Lax, A.L. McWhorter, R.H. Rediker, and H.J. Zeiger, *Appl. Phys. Lett.* **1**, 91 (1962).

6. B. Bölger and J.C. Diels, *Phys. Lett. A* **28**, 401 (1968).

7. S. Siahatgar and U.E. Hochuli, *IEEE J. Quantum Electron.* **QE-5**, 295 (1969).

8. U. Hochuli, P. Haldemann, and S. Siahatgar, *J. Appl. Phys.* **40**, 3374 (1969).

9. J.C. Camparo, *Contemp. Phys.* **26**, 443 (1985).

10. C.E. Wieman and L. Hollberg, *Rev. Sci. Instrum.* **62**, 1 (1991).

11. H. Sasada, *J. Chem. Phys.* **88**, 767 (1988).

12. H. Sasada and K. Yamada, *Appl. Opt.* **29**, 3535 (1990).

13. T. Ohshima and H. Sasada, *J. Mol. Spec.* **136**, 250 (1989).

14. S. Kinugawa and H. Sasada, *Jpn. J. Appl. Phys.* **29**, 611 (1990).

15. H. Sasada and T. Amano, *J. Chem. Phys.* **92**, 2248 (1990).

16. T. Yanagawa, S. Saito and Y. Yamamoto, *Appl. Phys. Lett.* **45**, 826 (1984).

17. T. Yanagawa, S. Saito, S. Machida, Y. Yamamoto and Y. Noguchi, *Appl. Phys. Lett.* **47**, 1036 (1985).

18. H. Sasada, T. Amano, C. Jarman, and P.F. Bernath, *J. Chem. Phys.* **94**, 2401 (1991).

19. M. Fujitake, R. Kiryu, and N. Ohashi, *J. Mol. Spec.* **154**, 169 (1992).

20. H. Kanamori, S. Takashima and K. Sakurai, *J. Chem. Phys.* **95**, 80 (1991).

21. W. Lenth and M. Gehrtz, *Appl. Phys. Lett.* **47**, 1263 (1985).

22. D.T. Cassidy, *Appl. Opt.* **27**, 610 (1988).

23. D.T. Cassidy and L.J. Bonnell, *Appl. Opt.* **27**, 268 (1988).

24. D.M. Bruce and D.T. Cassidy, *Appl. Opt.* **29**, 1327 (1990).

25. A.C. Stanton and J.A. Silver, *Appl. Opt.* **27**, 5009 (1988).

26. L.-G. Wang, D.A. Tate, H. Riris, and T.F. Gallagher, *J. Opt. Soc. Am. B* **6**, 871 (1989).

27. T.J. Johnson, F.G. Weinhold, J.P. Burrows, and G.W. Harris, *Appl. Opt.* **30**, 407 (1991).

28. K. Uehara and H. Tai, *Appl. Opt.* **31**, 809 (1992).

29. H.C. Casey and M.B. Panish, *Heterostructure Lasers*, Academic Press: Orlando (1978).

30. G.P. Agrawal and N.K. Dutta, *Long-Wavelength Semiconductor Lasers*, Van Nostrand Reinhold: New York (1986).

31. K. Petermann, *Laser Diode Modulation and Noise*, Kluwer Academic Publishers, Dordrecht (1988).

32. F.H. Peters, Ph.D. thesis, McMaster University (1991).

33. J.E. Hayward and D.T. Cassidy, *Appl. Phys. Lett.* **59**, 1150 (1991).

34. J.E. Hayward and D.T. Cassidy, *J. Opt. Soc. Am. B* **9**, 1151 (1992).

35. C.H. Henry, *IEEE J. Quantum Electron.* **QE-18**, 259 (1982).

36. R. Lang and K. Kobayashi, *IEEE J. Quantum. Electron.* **QE-16**, 347 (1980).

37. J. Buus, *Single Frequency Semiconductor Lasers*, SPIE Optical Engineering Press: Bellingham (1991).

38. D.T. Cassidy, D.M. Bruce, and B.F. Ventrudo, *Rev. Sci. Instrum.* **62**, 2385 (1991).

39. A.E. Siegman, *Lasers*, University Science Books: Mill Valley, CA (1986).

40. L.J. Bonnell and D.T. Cassidy, *Appl. Opt.* **28**, 4622 (1989).

41. K.R. Preston, K.C. Woollard and K.H. Cameron, *Electron. Lett.* **17**, 931 (1981).

42. P.A. Andrekson and A. Alping, *IEEE J. Quantum. Electron.* **QE-23**, 2078 (1987).

43. K.-Y. Liou, C.A. Burns, and F. Bosch, *J. Lightwave Tech.* **LT-3**, 985 (1985).

44. L.J. Bonnell, M.Eng. thesis, McMaster University (1989).

45. B.F. Ventrudo and D.T. Cassidy, submitted to *Applied Optics*, September 1992.

46. F.A. Jenkins and H.E. White, *Fundamentals of Physical Optics*, McGraw-Hill, New York, New York (1937).

47. G.F. Franklin, J.D. Powell, and A. Emani-Naeini, **Feedback Control of Dynamic Systems**, Addison-Wesley: Reading, Mass. (1986).

48. B.F. Ventrudo and D.T. Cassidy, *Appl. Opt.* **29**, 5007 (1990).

49. R.W. Tkach and A.R. Chraplyvy, *IEEE J. Lightwave Technol.* **LT-4**, 1655 (1986).

50. J. Reid and D. Labrie, *Appl. Phys. B* **26**, 203-210 (1981).

51. J. Reid, J. Shewchun, B.K. Garside and E.A. Ballik, *Appl. Opt.* **17**, 300 (1978).

52. G.R. Janik, C. Carlisle and T.F. Gallagher, *J. Opt. Soc. Am. B* **3**, 1070 (1986).

53. J.A. Silver, *Appl. Opt.* **31**, 707 (1992).

54. D.S. Bomse, A.C. Stanton and J.A. Silver, *Appl. Opt.* **31**, 718 (1992).

55. H. Sasada, Keio University, private communication (1990)..

56. K.E. Kerr, T.J. Byers, B.F. Ventrudo, D.T. Cassidy, T. Momose, and T. Oka, *47th Ohio State University International Symposium on Molecular Spectroscopy, June 15-19* (1992).

57. K.E. Kerr, T.J. Byers, B.F. Ventrudo, D.T. Cassidy, T. Momose, and T. Oka, submitted to *Journal of Chemical Physics*, September 1992.

58. L. Melander and W.H. Saunders, *Reaction Rates of Isotopic Molecules*, Wiley: New York (1980).

59. P.S. Lee and R.F. Majkowski, *Physics Today*, Nov. 1987, D22.

60. M. Schidlowski, J. M. Hayes, and I.R. Kaplan, in *Earth's Earliest Biosphere, Its Origins and Evolution*, J.W. Schopf, ed., Princeton U. Press: Princeton, N.J. (1983).

61. B.P. Tissot and D.H. Welte, *Petroleum Formation and Occurence*, Springer-Verlag: Berlin (1984).

62. D. Labrie and J. Reid, *Appl. Phys.* **24**, 381 (1981).

63. P.S. Lee and R.F. Majkowski, *Appl. Phys. Lett.* **48**, 619 (1986).

64. J.F. Becker, T.B. Sauke, and M. Loewenstein, *Appl. Opt.* **31**, 1921 (1992).

65. L.S. Rothman, R.R. Gamache, A. Goldman, L.R. Brown, R.A. Toth, H.M. Pickett, R.L. Poynter, J-M. Flaud, C. Camy-Peyret, A. Barbe, N. Husson, C.P. Rinsland, and M.A.H. Smith, *Appl. Opt.* **26**, 4058 (1987).

66. R. Toth, NASA Jet Propulsion Laboratory, Pasadena, CA; private communication.

67. K.R. Lang, *Astrophysical Formulae, 2nd. ed.*, Springer Verlag: Heidelberg (1980).

68. W.S. Benedict, R. Herman, G.E. Moore, and S. Silverman, *Can. J. Phys.* **34**, 830 (1956).

69. D.W. Poesner, *Austral. J. Phys.* **12**, 184 (1959).

70. J. van Kranendonk, *Physica* **25**, 1180 (1959).

71. J. van Kranendonk, *Can. J. Phys.* **38**, 240 (1960).

72. J. van Kranendonk, *Solid Hydrogen*, Plenum: New York (1983).

73. M. Okumura, M-C. Chan, and T. Oka, *Phys. Rev. Lett.* **62**, 32 (1989).

74. M-C. Chan, S.S. Lee, M. Okumura, and T. Oka, *J. Chem. Phys.* **95**, 88 (1991).

75. E.J. Allin, W.F.J. Hare, and R.E. MacDonald, *Phys Rev.* **98**, 554 (1955).

76. R.D.G. Prasad, M.J. Clouter, and S.P. Reddy, *Phys. Rev. A* **17**, 1690 (1978).

77. T.K. Balasubramanian, C.H. Lien, K.N. Rao, and J.R. Gaines, *Phys. Rev. Lett.* **47**, 1277 (1981).

78. H. Sasada, Keio University, private communication.

79. S.S. Lee, B.F. Ventrudo, D.T. Cassidy, T. Oka, S. Miller and J. Tennyson, *J. Mol. Spec.* **145**, 222 (1991).

80. J.J. Thomson, *Phil. Mag.* **24**, 209 (1912).

81. A.J. Demspter, *Phil. Mag.* **31**,428 (1916).

82. T.R. Hogness and E.G. Lunn, *Phys. Rev.* **25**, 452 (1925).

83. J.O. Hirschfelder, *J. Chem. Phys.*, **6**, 3627 (1938).

84. quote from G. Handler and J.R. Arnold, *J. Chem. Phys.* **27**, 144 (1957).

85. R.E. Christoffersen, S. Hagstrom, F. Prosser, *J. Chem. Phys.* **40**, 236 (1964).

86. G.D. Carney, *Mol. Phys.* **39**, 923 (1980).

87. G.D. Carney and R.N. Porter, *Phys. Rev. Lett.* **49**, 537 (1980).

88. S. Miller and J. Tennyson, *J. Mol. Spec.* **126**, 183 (1987).

89. S. Miller and J. Tennyson, *Ap. J.* **335**, 486 (1988).

90. S. Miller, J. Tennyson and B.T. Sutcliffe, *Mol. Phys.* **66**, 429 (1988).

91. S. Miller and J. Tennyson, *J. Mol. Spec.* **136**, 223 (1989).

92. S. Miller and J. Tennyson, *J. Mol. Spec.* **141**, 104 (1990).

93. B.M. Dinelli, S. Miller, and J. Tennyson, *J. Mol. Spec.* **153**, 718 (1992).

94. W. Meyer, P. Bostschwina and P.G. Burton, *J. Chem. Phys.* **84**, 891 (1986).

95. M. Saporoschenko, *Phys. Rev.* **139A**, 349 (1965).

96. E. Herbst and W. Klemperer, *Ap. J.* **185**, 505 (1973).

97. W.D. Watson, *Rev. Mod. Phys.* **48**, 513 (1976).

98. T.R. Geballe and T. Oka, *Ap.J.* **342**, 855 (1989).

99. J.P. Maillard and P. Drosart, *CFHT Bull.* **20**, 13 (1989).

100. P. Drossart, J.P. Maillard, J. Caldwell, S.J. Kim, J.K.G. Watson, W.A. Majewski, J. Tennyson, S. Miller, S.K. Atreya, J.T. Clarke, J.H. Waite, Jr., and R. Wegener, *Nature* **340**, 539 (1989).

101. T. Oka and T.R. Geballe, *Ap. J. Lett.* **351**, L53 (1990).

102. S. Miller, R.D. Joseph and J. Tennyson, *Ap. J.* **360**, L55 (1990).

103. T. Oka, private communication, July 1992.

104. J.K.G. Watson, S.C. Foster, A.R.W. McKellar, P. Bernath, T. Amano, F.S. Pan, M.W. Crofton, R.S. Altman, and T. Oka, *Can. J. Phys.* **62**, 1875 (1984).

105. J.K.G. Watson, *J. Mol. Spec.* **103**, 350 (1984).

106. G. Herzberg, *Molecular Spectra and Molecular Structure II: Infrared and Raman Spectra of Polyatomic Molecules* Van Nostrand Reinhold: New York (1945).

107. C.H. Townes and A.L. Schawlow, *Microwave Spectroscopy*, McGraw-Hill: New York (1955).

108. T. Oka, *Phys. Rev. Lett.* **45**, 531 (1980).

109. W.A. Majewski, P.A. Feldman, J.K.G. Watson, S. Miller, and J. Tennyson, *Ap. J. Lett.* **347**, L51-L54 (1989).

110. L-W. Xu, C. Gabrys, and T. Oka, *J. Chem Phys.* **93**, 6210 (1990).

111. M.G. Bawendi, B.D. Rehfuss, and T. Oka, *J. Chem. Phys.* **93**, 6200 (1990).

112. L.D. Landau and E.M. Lifshitz, *Quantum Mechanics (Non-Relativistic Theory)*, Pergamon Press: Oxford (1977).

113. S.S. Lee, private communication, July 1990.

114. T. Oka, in *Frontiers of Laser Spectroscopy of Gases*, p. 353, Kluwer Academic Publishers (1988).

115. C.S. Gudeman, M.H. Begemann, J. Pfaff and R.J. Saykally, *Phys. Rev. Lett.* **50**, 727 (1983).

116. N.H. Haese, F.S. Pan and T.Oka, *Phys. Rev. Lett.* **50**, 1575 (1983).

117. H. Solka, W. Zimmermann, D. Reinert, A. Stahn, A. Dax and W. Urban, *Appl. Phys. B.* **48**, 235 (1989).

118. D.J. Nesbitt, H. Petek, C.S. Gudeman, C.B. Moore and R.J. Saykally, *J. Chem. Phys.* **81**, 5281 (1984).

119. J.K.G. Watson, S.C. Foster, A.R.W. McKellar, P. Bernath, T. Amano, F.S. Pan, M.W. Crofton, R.S. Altman and T. Oka, *Can. J. Phys.* **62**, 1875 (1984).

120. T. Oka, private communication, Jan. 1992.

121. A. Hemmerich, D.H. McIntyre, D. Schropp, Jr., D. Meschede, and T.W. Hansch, *Opt. Comm.* **75**, 118 (1990).